DEUTSCHES ELEKTRONEN-SYNCHROTRON DESY

DESY 83-130
December 1983

JET PRODUCTION AND FRAGMENTATION IN e^+e^- ANNIHILATION AT 12 - 43 GeV

by

TASSO Collaboration

ISSN 0418-9833

NOTKESTRASSE 85 · 2 HAMBURG 52

DESY 83-130
December 1983
ISSN 0418-9833

Jet Production and Fragmentation in e^+e^- Annihilation at 12 - 43 GeV

TASSO Collaboration

M.Althoff, W.Braunschweig, F.J.Kirschfink, K.Lübelsmeyer, H.-U.Martyn, G.Peise,
J.Rimkus[*], P.Rosskamp, H.G.Sander, D.Schmitz, H.Siebke, W.Wallraff
I. Physikalisches Institut der RWTH Aachen, Germany[§]

H.M.Fischer, H.Hartmann, W.Hillen[**], A.Jocksch, G.Knop, L.Köpke, H.Kolanoski,
H.Kück, V.Mertens, R.Wedemeyer, N.Wermes[***], M.Wollstadt[****]
Physikalisches Institut der Universität Bonn, Germany[§]

Y.Eisenberg[*****], K.Gather, H.Hultschig, P.Joos, W.Koch, U.Kötz, H.Kowalski,
A.Ladage, B.Löhr, D.Lüke, P.Mättig, D.Notz, R.J.Nowak[+], J.Pyrlik, D.R.Quarrie[++],
M.Rushton, W.Schütte, D.Trines, G.Wolf, Ch.Xiao[+++]
Deutsches Elektronen-Synchrotron,DESY, Hamburg, Germany

R.Fohrmann, E.Hilger, T.Kracht, H.L.Krasemann, P.Leu, E.Lohrmann, D.Pandoulas,
G.Poelz, K.U.Pösnecker, B.H.Wiik
II. Institut für Experimentalphysik der Universität Hamburg, Germany[§]

R.Beuselinck, D.M.Binnie, A.J.Campbell[******], P.J.Dornan, B.Foster, D.A.Garbutt,
C.Jenkins, T.D.Jones, W.G.Jones, J.McCardle, J.K.Sedgbeer, J.Thomas,
W.A.T. Wan Abdullah[*******]
Department of Physics, Imperial College London, England[§§]

K.W.Bell, M.G.Bowler, P.Bull, R.J.Cashmore, P.E.L.Clarke, R.Devenish,
P.Grossmann, C.M.Hawkes, S.L.Lloyd, G.L.Salmon, T.R.Wyatt, C.Youngman
Department of Nuclear Physics, Oxford University, England[§§]

G.E.Forden, J.C.Hart, J.Harvey, D.K.Hasell, J.Proudfoot[++++],D.H.Saxon,
P.L.Woodworth[+++++]
Rutherford Appleton Laboratory, Chilton, England[§§]

F.Barreiro, M.Dittmar, M.Holder, B.Neumann
Fachbereich Physik der Universität-Gesamthochschule Siegen, Germany[§]

E.Duchovni, U.Karshon, G.Mikenberg, R.Mir, D.Revel, E.Ronat, A.Shapira,
G.Yekutieli
Weizmann Institute, Rehovot, Israel[§§§]

G.Baranko, T.Barklow[***], A.Caldwell, M.Cherney, J.M.Izen, M.Mermikides, G.Rudolph,
D.Strom, H.Venkataramania, E.Wicklund, Sau Lan Wu, G.Zobernig
Department of Physics, University of Wisconsin, Madison, Wisconsin, USA[§§§§]

December 1983

To be submitted to Z. Physic C

---

[*] Now at Siemens, München, Germany
[**] Now at Philips, Aachen, Germany
[***] Now at SLAC, Stanford, CA, USA
[****] Now at Lufthansa, Frankfurt, Germany
[*****] On leave from Weizmann Institute, Rehovot, Israel
[******] Now at Glasgow University, Glasgow, UK
[*******] On leave from Universiti Malaya, Kuala Lumpur
[+] On leave from Warsaw University, Warsaw, Poland
[++] Now at FNAL, Batavia, IL, USA
[+++] On leave from the University of Science and Technology of China, Hefei, Supported by the Konrad - Adenauer-Stiftung
[++++] Now at Argonne National Laboratory, Argonne, IL, USA
[+++++] Now at Institute of Oceanographic Sciences, Bidston, Merseyside, UK

[§] Supported by the Deutsches Bundesministerium für Forschung und Technologie
[§§] Supported by the UK Science and Engineering Research Council
[§§§] Supported by the Minerva Gesellschaft für Forschung mbH
[§§§§] Supported by the US Department of Energy contract DE-AC02-76ER00881

Abstract

We present the general properties of jets produced by e^+e^- annihilation. Their production and fragmentation characteristics have been studied with charged particles for c.m. energies between 12 and 43 GeV. In this energy range e^+e^- annihilation into hadrons is dominated by pair production of the five quarks u,d,s,c and b. In addition, hard gluon bremsstrahlung effects which are invisible at low energies become prominent at the high energies. The observed multiplicity distributions deviate from a Poisson distribution. The multiplicity distributions for the overall event as well as for each event hemisphere satisfy KNO scaling to within ~20 %. The distributions of $x_p = 2p/W$ are presented; scale breaking is observed at the level of 25 %. The quantity $x_p\, d\sigma/dx_p$ is compared with multigluon emission calculations which predict a Gaussian distribution in terms of $\ell n(1/x)$. The observed energy dependence of the maximum of the distributions is in qualitative agreement with the calculations. Particle production is analysed with respect to the jet axis and longitudinal and transverse momentum spectra are presented. The angular distribution of the jet axis strongly supports the idea of predominant spin 1/2 quark pair production. The particle distributions with respect to the event plane show clearly the growing importance of planar events with increasing c.m. energies. They also exclude the presence of heavy quark production, $e^+e^- \rightarrow Q\overline{Q}$, for quark masses up to $5 < m_Q < 20.3$ GeV ($|e_Q| = 2/3$) and $7 < m_Q < 19$ GeV ($|e_Q| = 1/3$). The comparison of $1/\sigma_{tot}\, d\sigma/dp_T$ measured at 14, 22 and 34 GeV suggests that hard gluon bremsstrahlung contributes mainly to transverse momenta larger than 0.5 GeV/c. The rapidity distribution for $W \geq 22$ GeV shows an enhancement away from $y = 0$ which corresponds to an increase in yield of 10 - 15 % compared to the centre region ($y = 0$). The enhancement probably results from heavy quark production and gluon bremsstrahlung. The particle flux around the jet axis shows with increasing c.m. energy a rapidly growing number of particles collimated around the jet axis, while at large angles to the jet axis almost no W dependence is observed. For fixed longitudinal momentum $p_{||}$ approximate "fan invariance" is seen: The shape of the angular distribution around the jet axis is almost independent of W. The collimation depends strongly on $p_{||}$. For small $p_{||}$, $p_{||} < 0.2$ GeV/c, isotropy is observed. With increasing $p_{||}$ the particles tend to be emitted closer and closer to the jet axis.

1. Introduction

All available data support the hypothesis that high energy e^+e^- annihilation into hadrons proceeds predominantly through the production of a pair of quarks, $e^+e^- \rightarrow q\bar{q}$, followed by their fragmentation into hadrons. This and the fact that, unlike hadron-hadron collisions, no spectators are around which might disturb the hadronization process, makes e^+e^- annihilation an ideal place to study quark fragmentation into hadrons. Apart from the two-jet events produced by $q\bar{q}$ fragmentation, a small fraction of the events at high c.m. energies has a three-jet structure1,2). They can be understood as the result of hard gluon bremsstrahlung, $e^+e^- \rightarrow q\bar{q}g$. The data to be discussed below include the contributions from these events.

In this paper we present the general properties of hadronic final states produced by e^+e^- annihilation at c.m. energies W between 12 and 43 GeV. The results are based on the information from charged particles summed over all particle species. Particle separated cross sections from this experiment have been given elsewhere3,4). No attempt has been made to separate the contributions from different quark flavours. The results, therefore, represent sums over all possible quark flavours, which contribute to the total cross section approximately in the ratio of the quark charges squared, $u\bar{u} : d\bar{d} : s\bar{s} : c\bar{c} : b\bar{b} = 4 : 1 : 1 : 4 : 1$.

As a reference, some of the data are compared with the predictions from QCD using for the fragmentation into hadrons an independent jet fragmentation model5,6) and a string model7).

2. Particle and event selection

The data were obtained at the PETRA storage ring with the TASSO detector for the c.m. energies shown in Table 1. Details of the detector can be found elsewhere[8)]. The data taking and analysis procedure was identical to that used for the determination of the total hadronic annihilation cross section[9)]. The multihadron events were detected in the central detector using the information on charged particles. For the events used in this analysis the trigger required a minimum number of charged particles with polar angles θ measured with respect to the beam direction (z direction) satisfying $|\cos\theta| < 0.82$ and with a minimum momentum p_{xy} perpendicular to the beam. The minimum number of tracks demanded was between 2 and 5; it was 2 for most of the data. The nominal minimum p_{xy} was set to 0.22 GeV/c at W = 14 and 22 GeV and for a large part of the data at 35 GeV, and 0.32 GeV/c for all other energies. After event reconstruction charged tracks were accepted if they satisfied the following requirements:

(a) $d_0 < 5$ cm where d_0 is the distance of closest approach to the nominal beam position in the (x,y) plane,

(b) $p_{xy} > 0.1$ GeV/c,

(c) $|\cos\theta| < 0.87$,

(d) $|z - z_v| < 20$ cm, where z is the track coordinate at the point of closest approach to the beam and z_v is the z coordinate of the event vertex averaged over the tracks.

The r.m.s. momentum resolution including multiple scattering was $\sigma_p/p = 0.016\,(1 + p^2)^{1/2}$, p in GeV/c. The angular resolution was typically $\sigma_\varphi = 4$ mrad in azimuth and $\sigma_\Theta = 6$ mrad in the polar angle.

The events were required to obey the following criteria:

1. at least 4 (5) accepted tracks for W = 12 - 25 GeV ($W \geq 27$ GeV),
2. to suppress the contribution from τ pair production at W < 15 GeV (W > 15 GeV) events with 3 charged tracks in one hemisphere with respect to the sphericity axis and 3 (1 or 3) in the other hemisphere were discarded if the effective mass of both particle systems was less than the τ mass (assuming pion masses for the observed particles),

3. for $W \leq 14$ GeV, tracks were required in both hemispheres defined with respect to the beam axis, and the sum of the charges of the accepted tracks was not to exceed 3,
4. the z coordinate of the event vertex had to be $|z_v| < 6$ cm,
5. the momentum sum $\Sigma p \equiv \Sigma |p_i|$ of the particle momenta had to be $\Sigma p > 0.265$ W.

These cuts discriminated against beam gas scattering (3-5), τ pair production (1,2), Bhabha scattering and μ pair production (1) and γγ scattering (1,5). All events surviving these cuts were inspected visually. Approximately 3% were rejected, most of them being Bhabha scattering events producing electromagnetic showers in the material before the tracking chambers.

A total of 28 721 events from an integrated luminosity of 90 pb^{-1} passed the selection criteria. The contamination of the accepted events by other processes was found to be small (Ref. 9): from beam gas scattering $0.5 \pm 0.5\%$ at $W \leq 15$ GeV and a negligible amount at higher energies; from τ pair production $1.5 \pm 1.5\%$ ($1.2 \pm 1.2\%$) at $W \leq 15$ GeV ($W > 15$ GeV); from γγ scattering $1.6 \pm 0.8\%$. The systematic uncertainty in the corrected number of events is 1.8% at W = 14 GeV, 1.5% at W = 34 GeV and 1.3% at W = 41.5 GeV.

3. Corrections

The distributions presented below were corrected for acceptance and other detector effects and radiative effects. The corrected cross sections $d\sigma(x)$ as a function of a variable x were obtained from the measured distribution $dn_{meas}(x)$ with the help of a correction function $C(x)$,

$$d\sigma(x) = C(x)\, dn_{meas}(x) \tag{1}$$

which was determined by a Monte Carlo technique$^{5)}$, generating $q\bar{q}$ and $q\bar{q}g$ events in first order QCD and using Field-Feynman type fragmentation functions$^{10)}$.

Firstly, N_{gen} Monte Carlo events were generated at a fixed c.m. energy W without QED radiative effects. These events yielded the distribution $n_{gen}(x)$ of charged particles. For $n_{gen}(x)$ all primary produced particles or those produced in the decay of particles with lifetimes less than $3 \cdot 10^{-10}$ sec were considered. For example the charged particles from K^o_S and Λ decays were included, irrespective of how far away from the interaction point the decay occurred, while the charged particles from K^o_L decay were not included. Secondly, events were generated including QED radiative effects[11)]. The generated events were followed through the detector generating hits in the track chambers. Energy loss, multiple scattering, photon conversion and nuclear interactions in the material of the detector as well as decays were taken into account. The events were then passed through the track reconstruction and acceptance programs used for the real data, yielding N_{det} accepted events and producing the particle distribution $n_{det}(x)$.

Using the total cross section values, σ_{tot}, measured in this experiment, and the number of accepted events in the real data, N_{meas}, the correction factor C(x) was calculated as

$$C(x) \;=\; \frac{\sigma_{tot}}{N_{meas}} \left(\frac{n_{gen}(x)}{N_{gen}}\right) \Bigg/ \left(\frac{n_{det}(x)}{N_{det}}\right)$$

The systematic error on the correction factor was estimated by comparing the C(x) values obtained with the independent jet and the string model, by varying the fragmentation parameters and by studying uncertainties for instance in the correction for secondary interactions and for the finite momentum resolution. As an example of the size of the systematic uncertainty we consider the scaled cross section $1/\sigma_{tot}\, d\sigma/dx_p$, $x_p = 2p/W$. At $W = 34$ GeV the systematic error was typically 5 % for $x_p < 0.05$, 4 % for $0.05 < x_p < 0.5$ and 11 % for $0.5 < x_p < 0.8$. If not stated otherwise, the error bars given in the distributions below show only the statistical error; the systematic error in general are of the order of the statistical errors.

4. QCD Models

This section describes briefly the QCD models used for the correction of the data and for comparison with the data. The QCD prediction for $e^+e^- \to q\bar{q}$, $q\bar{q}g$ at the parton level was calculated in first order of α_s according to Refs. 5 - 7.

For the fragmentation of quarks and gluons into hadrons two different models, an independent jet model and a string model, were considered. In the independent jet model based on the work of Hoyer et al.$^{5)}$ and Ali et al.$^{6)}$ quarks and gluons are assumed to fragment independently into hadrons. In the model of the Lund group$^{7)}$ hadronization occurs along the colour field lines (strings) between quarks and gluons. In both models the fragmentation functions $^{7,10)}$ depend on a set of parameters whose values have to be found by comparison with experiment. We have fitted these parameters together with α_s in the course of a QCD analysis$^{12)}$ by adjusting the model predictions to our high energy data. Different α_s values have been found in this analysis, $\alpha_s = 0.19 \pm 0.02$ for independent jet fragmentation and $\alpha_s = 0.27 \pm 0.03$ for string fragmentation. These α_s values were used for the present comparison. The QCD predictions were computed with both models. In general, both gave similar results. For this reason in most cases only the predictions of the independent jet model are shown.

5. The total cross section

Table 1 lists the number of accepted events. The bulk of the data were obtained at W = 14, 22, 30 -36.7 and 38.7-43.1 GeV. The latter energy intervals will be referred to as $\overline{W}$ = 34 GeV and $\overline{W}$ = 41.5 GeV. Fig. 1 (see also Table 1) shows the total cross section for e^+e^- annihilation into hadrons, σ_{tot}, in terms of the ratio

$$R \equiv \sigma_{tot} / \sigma_{\mu\mu} \tag{3}$$

where $\sigma_{\mu\mu} = \frac{4\pi\alpha^2}{3s} = \frac{86.9}{s}$ nb, $s = W^2$ in GeV^2. The cross section data up to 33.5 GeV have already been presented in Ref. 9. The data measured in this experiment are shown together with those from other experiments$^{13)}$. Our data between 14 and 43.1 GeV are consistent with a constant value of R, the average being R = 4.04 ± 0.02 (stat.) ± 0.19 (syst.).

6. Charged particle multiplicities

The corrected multiplicity distribution was determined by unfolding the observed multiplicity distribution. Let $N_m(i)$ be the number of accepted events with i accepted charged tracks and N(j) be the corrected number of events with j(j = even) produced charged particles. The two distributions were related by a matrix M:

$$N(j) = M_{ji}\, N_m(i) \tag{4}$$

The coefficients M_{ji} were determined from events generated by the Monte Carlo programs mentioned above. In this case N(j) gives the multiplicity distribution of events generated at a fixed c.m. energy (i.e. without the emission of radiative photons). $N_m(i)$ is the multiplicity distribution of the Monte Carlo events obtained by including radiative and detector effects and imposing acceptance criteria. Eq.(4) was used to determine the multiplicity distribution for $j \geq n_{min}$ where $n_{min} = 4$ (5) is the minimum number of accepted tracks at $W \leq 15$ (> 15) GeV. For the multiplicities j = 0, 2 (j =0, 2, 4) at $W \leq 15$ (> 15) GeV the corrected numbers of events were taken from the Monte Carlo calculation. The uncertainty of these numbers were estimated by comparing the predictions of the independent jet and the string models and was found to be of the order of a factor of two. Due to the fact that the fraction of events with $j < n_{min}$ is only a few percent the N(j) value for $j < n_{min}$ has little effect on the average charge multiplicity $\langle n_{CH} \rangle$ and on the dispersion D, defined as

$$D = (\langle n_{CH}^2 \rangle - \langle n_{CH} \rangle^2)^{1/2} \tag{5}$$

For completeness we mention that the correction for radiative effects alone raised $\langle n_{CH} \rangle$ typically by 5% and reduced D by 4%.

Fig. 2 and Table 2 show the charged particle multiplicity distribution at W = 14, 22 and 34 GeV. The nonaccepted multiplicities $n_{CH} \leq 4(5)$ at $W \leq 15$ (>15) GeV were taken from Monte Carlo predictions (see above). The error bars shown are statistical except for the nonaccepted multiplicities where they are of purely systematic origin. As mentioned before, the $\pi^\pm$ from the decay $K_S^0 \rightarrow \pi^+\pi^-$ are included: they contribute 0.75, 0.85, 1.0, ~1.05 units to the multiplicity at 14, 22, 34, 41.5 GeV, respectively. The average multiplicity is shown in Fig. 3 as a function of W and listed in Table 3. It is corrected for the nonaccepted multipicities. The error bars shown in Fig. 3 are purely statistical. The systematic uncertainty for $\langle n_{CH} \rangle$ is ±0.25 at W = 14 GeV increasing to ±0.45 at W = 41.5 GeV.

Fig. 3 shows also measurements for $<n_{CH}>$ from other experiments and from lower energies[14,15]. As noted earlier[16-18], the average multiplicity rises faster than ℓn W. Most of this rise can be understood as a result of the increase in phase space and the corresponding reduced dependence on particle masses[19]. In Fig. 4 $<n_{CH}>$ is compared with the QCD model prediction and with the prediction for $q\bar{q}$ production alone. Gluon emission is seen to increase $<n_{CH}>$ by only a small amount: 0.6 units for W = 14 GeV and 1.4 units for W = 41.5 GeV. The QCD prediction agrees well with the data. Fig. 5 compares the $<n_{CH}>$ measurements in e^+e^- annihilation with those for pp and $p\bar{p}$ interactions[20-24]. The latter two processes produce 20 - 30 % less charged particles than e^+e^- annihilation at the same c.m. energy. If, on the other hand, for pp → ppX the two leading protons are removed from the multiplicity sum and the remaining multiplicity is measured as a function of the c.m. energy of the system X, closer agreement with the e^+e^- multiplicity is observed[25].

We analysed the e^+e^- multiplicity results shown in Fig. 2 in terms of several models. We discuss first fits to the W dependence of $<n_{CH}>$. The $<n_{CH}>$ values were fitted to various functional forms. In performing the fits a systematic error of 5 % was assumed for each measurement.

(a) $<n_{CH}> = a + b\, \ell ns + c\, \ell n^2 s$ as suggested by the analysis of pp data[21]. The fit yielded

$$a = 3.33 \pm 0.11 \qquad b = -0.40 \pm 0.08 \qquad c = 0.26 \pm 0.01$$

with $\chi^2 = 85$ for 79 d.o.f. The solid curve in Fig. 5 shows the result of this fit.

(b) Phase space like production predicts[26]

$$<n_{CH}> = a\, s^{1/4}$$

The fit yielded $a = 2.18 \pm 0.01$ with $\chi^2 = 146$ for 81 d.o.f.

(c) $n_{CH} = a + b \exp\{c(\ell n\, s/Q_0^2)^{1/2}\}$

This form has been advocated by QCD calculations for the evolution of partons in the leading log approximation[27-30]. Using the data over the full W range and assuming $Q_0 = 1$ GeV, the fit gave

$$a = 2.71 \pm 0.08 \qquad b = 0.058 \pm 0.010 \qquad c = 1.97 \pm 0.06$$

with $\chi^2 = 81$ for 79 d.o.f. The fit result is shown by the dashed-dotted curve in Fig. 5.

In Ref. 29 a prediction has been given for the coefficient c, $c = \sqrt{72/(33 - 2N_f)}$, where N_f is the number of flavours. Using $N_f = 3$ for $1.8 < W < 3.7$ GeV, $N_f = 4$ for $3.7 < W < 10.5$ GeV and $N_f = 5$ for $W > 10.5$ GeV and treating Q_0 as a free parameter the fit gave the following result:

$$a = 2.56 \pm 0.02 \qquad b = 0.089 \pm 0.024 \qquad Q_0 = 0.85 \pm 0.34 \text{ GeV}$$

with $\chi^2 = 72$ for 79 d.o.f.

We turn now to a discussion of the shape of the multiplicity distributions. The dispersion D is shown in Fig. 6 as a function of W. The error bars do not include the systematic uncertainties which are close to ±7 % of the D values. Also shown are measurements by the LENA group$^{14)}$ at lower energy and by the PLUTO group$^{14)}$. The energy dependence of the dispersion can be described by the form $D = c_1 + c_2 \ln s + c_3 \ln^2 s$. As shown in Fig. 7 rather similar values are measured for D in e^+e^- annihilation and in pp, $p\bar{p}$ interactions.

The multiplicity distributions shown in Fig. 2 were compared with two types of Poisson distributions. The first type (dashed curves in Fig. 2) ignores the fact that the number of positive and negative charged particles have to be equal. To a good approximation,

$$N(i) = 2 \frac{\lambda^i}{i!} e^{-\lambda} \quad . \tag{6}$$

Here N(i) is the number of events with i charged particles (i = even) and $\lambda = \langle n_{CH} \rangle$. The second type (solid curves in Fig. 2) acknowledges the fact that there are equal numbers of positive and negative particles:

$$N(i) = \frac{(\lambda/2)^{i/2} e^{-\lambda/2}}{(i/2)!} \tag{7}$$

The two types of distributions are seen to bracket the data, the first one predicting a narrower distribution, the second one predicting a wider distribution than observed.

In Fig. 8a we present the multiplicity distributions at 14, 22 and 34 GeV together with data measured by other experiments between 5 and 30.6 GeV in a way suitable to test for KNO scaling$^{31)}$, namely $P(n_{CH}) \langle n_{CH} \rangle$ versus $n_{CH}/\langle n_{CH} \rangle$ where $P(n_{CH})$ is the measured probability for events with multiplicity n_{CH}. Only the statistical errors are shown. The data of the JADE group$^{15)}$ (not shown) agree with our data shown in Fig. 8a. KNO scaling holds to within ~20 %. The shape of the distributions for e^+e^- is close to that observed in $p\bar{p}$ annihilation[22,23] but differs markedly from that for pp, $p\bar{p}$ collisions[20,21,24] (Fig. 8b). The ratio $<n_{CH}>/D$, shown in Fig. 9, is almost independent of the c.m. energy for both e^+e^- annihilation and pp,$p\bar{p}$ interactions. The latter have a ~30 % smaller $<n_{CH}>/D$ ratio.

Most of the e^+e^- events result from the production of two back-to-back jets (see below). In order to see whether the multiplicity distribution in each jet separately obeys KNO scaling, we analysed all events as two-jet events and assigned the accepted particles to one of the two jets using the sphericity axis. Fig. 10 shows the multiplicity distributions for a single jet for W = 14, 22 and 34 GeV. KNO scaling is also found to hold to within ~20 %. The ratio $<n_{CH}>/D$ per jet is approximately energy independent: 2.23 ± 0.04 ± 0.10 (W = 14 GeV), 2.27 ± 0.05 ± 0.15 (W = 22 GeV) and 2.34 ± 0.02 ± 0.20 (W = 34 GeV). These values are lower by $\sim\sqrt{2}$ than those obtained for the complete event: 2.80 ± 0.10 ± 0.15, 2.95 ± 0.10 ± 0.25 and 3.02 ± 0.03 ± 0.35, respectively. This means that the spread of the single jet multiplicity distribution is narrower by a factor of $\sim\sqrt{2}$ than for the whole event. This is to be expected for two-jet events if the two jets are uncorrelated.

7. Particle Momentum Spectra

The differential cross sections $1/\sigma_{tot}\ d\sigma/dp$ for inclusive charged particle production are given in Fig. 11 and Table 4 for p > 0.2 GeV/c. The cross sections decrease steeply with momentum. The distribution becomes broader as the c.m. energy increases. The energy dependence of the average momentum p (corrected for momenta below p = 0.2 GeV/c), is shown in Fig. 12 and listed in Table 3. It rises linearly with W in our energy range. The momentum spectra were used to determine the fraction of the c.m. energy carried by charged particles (neglecting particle masses), $f_{CH} = \sum_{CH} P_i/W$.
Extrapolation to zero momentum yielded the f_{CH} values given in Table 3. Within errors $f_{CH} = 0.58$ independent of the c.m. energy.

For completeness, Fig. 13 and Table 4 give the normalized cross section $1/\sigma_{tot}\ d\sigma/dx_p$, ($x_p$ fractional particle momentum, $x_p = 2p/W$) for W = 14, 22 and 34 GeV which have already been presented in Ref. 34. For $x_p > 0.2$ the cross sections fall steeply with x_p. At small x_p, $x_p \lesssim 0.1$, a rapid rise with

W is seen which corresponds to the observed growth of the multiplicity. For $x_p > 0.2$ the data show a slow but significant decrease with W. This is more clearly seen in Fig. 14 where $1/\sigma_{tot}\ d\sigma/dx_p$ is plotted versus $s = W^2$. Going from W = 14 to 41.5 GeV $1/\sigma_{tot}\ d\sigma/dx_p$ on the average is reduced by ~25 %. This scale breaking was discussed in detail in Ref. 32. The amount of scale breaking was quantified by fitting the data to the following form suggested by QCD:

$$1/\sigma_{tot}\ d\sigma/dx_p = c_1\ (1 + c_2\ \ell n(s/s_o)) \qquad (8)$$

where $s_o = 1\ \text{GeV}^2$. The fit results for c_1 and c_2 are given in Table 5. The scale breaking effects seen in this experiment are in agreement with the data from the MARKII[33)] and JADE[15)] experiments.

The observed x dependence of inclusive particle production was compared with several theoretical conjectures. The behaviour for $e^+e^- \rightarrow h$ + anything near $x_p = 1$ has been related to the s dependence of the $\gamma h\bar{h}$ formfactor $F_h(s)$ in the reaction $e^+e^- \rightarrow h\bar{h}$ (see Ref. 35). If $F_h(s) \propto s^{-m}$ for $s \rightarrow \infty$ a Drell-Yan-West relation predicts $d\sigma/dx_p \propto (1-x_p)^n$ with $n = 2m - 1$. For instance, for h = pion or kaon m = 1 is expected which leads to n = 1 while for protons m = 2 and hence n = 3 should be observed.

In order to determine the large x_p behaviour we multiplied $1/\sigma_{tot}\ d\sigma/dx_p$ by a factor of $f = x_p(1-x_p)^{-n}$ for n = 1, 2 and 3 (the factor x_p ensures a reasonable description of the data near $x_p = 0$). The result is shown in Fig. 15. In the high x_p region ($0.4 \leq x < 0.8$) the data suggest $f \cdot 1/\sigma_{tot}\ d\sigma/dx_p$ to be constant for a value of the power n between 1 and 2. Taking into account the fact that in the high x_p region roughly 20 - 30 % of all charged particles are protons (antiprotons)[3] the Drell-Yan-West relation seems to be in reasonable agreement with the data.

Studies of multigluon emission[30,35,36)] have led to qualitative predictions for the behaviour at small and medium x values. They suggest that the energy weighted gluon spectrum

$$x d\sigma/dx = -d\sigma/d(\ell n(1/x))$$

(x is the fractional gluon energy) follows a Gaussian distribution with respect to $\ell n(1/x)$. The distribution should be centered around $\ell n(1/x) = 1/4\ \ell n(s/\mu^2)$ where μ is the virtual gluon mass. The assumption that the gluon x distribution represents the x_p distribution of the final state particles and ignoring the fact that the observed particles result mostly from the decay of heavier particles, lead to the prediction

$$x_p\, d\sigma/dx_p \sim \exp\left[-\left\{\frac{c[\ell n(1/x_p) - 1/4\ \ell n(s/\mu^2)]^2}{\ell n^{3/2}(s/\Lambda^2) - \ell n^{3/2}(\mu^2/\Lambda^2)}\right\}\right] \qquad (9a)$$

where Λ is the QCD scale parameter and c is a constant. Eq.(9a) predicts for the energy dependence of the maximum,

$$(\ell n(1/x_p))_{max} = 1/4\ \ell n\ (s/\mu^2) \qquad (9b)$$

Fig. 16a shows the data for all charged particles in terms of $Fx_p\ d\sigma/dx_p$ as a function of $\ell n(1/x_p)$. F is a normalization constant such that $F\int(x_p\ d\sigma/dx_p)\ dx_p = 1$. The data exhibit a maximum whose position shifts to higher $\ell n\ (1/x_p)$ values as W increases. As mentioned before, eq.(9a) does not take into account the fact that most of the detected particles result from the decays of heavier particles. The influence of decays was studied (see Fig. 16b) using the QCD model to compute the spectrum of the prompt (i.e. before decay) charged particles (dashed curve) and of the particles after decay (solid curve). The position of the maximum is considerably lower for the prompt particles. The high $\ell n(1/x_p)$ (= low x_p) region is dominated by decays.

It has been suggested that the effect of decays is less important for heavier particles$^{36)}$. We show in Fig. 17a the quantity $x_p\ 1/\sigma_{tot}\ d\sigma/dx_p$ for $\pi^+ + \pi^-$, $K^+ + K^-$ and $p + \bar{p}$ production as measured in this experiment$^{3)}$. The curves are drawn to guide the eye. Qualitatively, a behaviour similar to that found for all charged particles is observed. We used the data shown in Figs. 16a, 17a to determine the position of the maximum. The resulting values are shown in Fig. 17b. The data are compared with lines whose logarithmic slope is given by eq.(9b). These lines are seen to agree well with the $\pi^\pm$, $K^\pm$ and $p,\bar{p}$ data. The slope observed for <u>all</u> charged particles is somewhat steeper than predicted by eq.(9b). The value of μ deduced from Fig. 17b is different for $\pi^\pm$, $K^\pm$ and $p,\bar{p}$: $\mu = 0.05 \pm 0.02$ GeV ($\pi^\pm$), $0.19\ ^{+\ 0.10}_{-\ 0.07}$ GeV ($K^\pm$) and $0.35\ ^{+\ 0.23}_{-\ 0.12}$ GeV ($p,\bar{p}$). We note that the QCD model predictions for $e^+e^- \rightarrow q\bar{q}$, $q\bar{q}g$ (not shown) agree with the data given in Fig. 17b.

8. Jet properties

8.1 Jet variables

In the following analysis all events were treated as two-jet events. The event shape was characterized in terms of the sphericity tensor[37)] and of thrust[38)]. The sphericity tensor is defined as

$$M_{\alpha\beta} = \sum_{j=1}^{N} P_{j\alpha} P_{j\beta} \qquad \alpha,\beta = x,y,z; \quad j = 1,\ldots, N \text{ particles} \tag{10}$$

with eigenvectors $\hat{n}_1$, $\hat{n}_2$, $\hat{n}_3$ and corresponding normalized eigenvalues

$$Q_K = \frac{\Sigma(\vec{p}_j \cdot \hat{n}_k)^2}{\Sigma\, p_j^2} \tag{11}$$

which satisfy $Q_1 + Q_2 + Q_3 = 1$ and which are ordered such that $0 \leq Q_1 \leq Q_2 \leq Q_3$. In terms of these Q_K, the sphericity S, the aplanarity A and the variable Y are given by

$$\begin{aligned} S &= \tfrac{3}{2}(Q_1 + Q_2) \\ A &= \tfrac{3}{2} Q_1 \\ Y &= \tfrac{\sqrt{3}}{2}(Q_2 - Q_1) \end{aligned} \tag{12}$$

The plane defined by $\hat{n}_2$ and $\hat{n}_3$ is called the event plane; $\hat{n}_3$ gives the sphericity axis (= jet axis determined by sphericity). Sphericity

$$S = \frac{3}{2}(Q_1 + Q_2) = \frac{3}{2}\,\frac{\Sigma p_T^2}{\Sigma p^2}, \qquad 0 \leq S \leq 1 \tag{13}$$

is a measure of how well particles are collimated into two jets. Here p_T is the particle transverse momentum with respect to the jet axis. Extreme two-jet events have $S = 0$ while for spherical events $S \rightarrow 1$. Aplanarity A, $0 \leq A \leq 0.5$, measures the flatness of events; extreme flat events have $A = 0$.

The average squared transverse momenta in and out of the event plane are defined as

$$<p^2_{Tin}> = Q_2 \frac{\Sigma p_j^2}{N} \tag{14}$$

$$<p^2_{Tout}> = Q_1 \frac{\Sigma p_j^2}{N} \tag{15}$$

Another measure of the jet structure is thrust T defined as[38)]

$$T = \text{Max} \frac{\Sigma|p_{||j}|}{\Sigma|p_j|} \qquad \frac{1}{2} \leq T \leq 1 \tag{16}$$

where $p_{||j}$ is the longitudinal particle momentum relative to the jet axis, which is chosen such as to maximize $\Sigma|p_{||j}|$. Extreme two-jet events have T = 1.

8.2 Choice of the jet axis

The appropriate choice for the overall jet axis of an event is a theoretical as well as an experimental question. The theoretical choice depends on the underlying parton final state. For events produced by a two-parton state (e.g. $e^+e^- \rightarrow q\bar{q}$) the thrust axis, representing the direction of the vector sum of all particles in a hemisphere defined by a plane perpendicular to the parton direction, should be close to the original parton direction. For events produced by a three-parton state (e.g. $e^+e^- \rightarrow q\bar{q}g$) the direction of the most energetic parton in general is the preferred axis. Again, the thrust axis should be the best choice. For four or more parton states it is not clear which is the preferred direction. The axis determined by the sphericity method which minimizes the sum of the squares of the transverse momenta should be close to the thrust axis for events produced by two partons but may differ considerably for three-parton configurations.

To study how well the jet axis reproduces the primary parton direction we generated events of the types $e^+e^- \rightarrow q\bar{q}$ and $e^+e^- \rightarrow q\bar{q}g$ in the two QCD models without radiative and detector effects. We determined the average angle $<\delta>$ between the thrust and sphericity axes (reconstructed from the final state charged and neutral particles) and the original parton-parton direction ($q\bar{q}$) or the direction of the most energetic parton ($q\bar{q}g$). The result is shown in

Table 6a for different c.m. energies. Table 6a shows that for the thrust and sphericity axes $<\delta>$ is $\approx 6^0$ at W = 14 GeV and $\approx 1^0 - 2^0$ at W = 41.5 GeV for $q\bar{q}$ states. If gluon emission is included, $<\delta>$ is larger. At 41.5 GeV the average value is $<\delta> = 4 - 5^0$. Averaged over all events the thrust and sphericity methods reproduce the parton direction with similar accuracy. Sizeable differences are found for hard wide angle gluon emission. For instance, for events at W = 34 GeV with a charged particle of $p_T > 2.6$ GeV/c : $<\delta> = 7^0$ for the thrust axis but $<\delta> = 11^0$ for the sphericity axis. This has a noticeable effect on the transverse momentum (p_T) spectra at high transverse momenta. Fig. 18 compares the measured $1/\sigma_{tot}\ d\sigma/dp_T^2$ determined with the thrust axis (✱) and with the sphericity axis (♦). The sphericity axis leads to significantly smaller (~10 - 20 %) p_T^2 values once $p_T^2 \gtrsim 5$ GeV^2. Qualitatively, this is to be expected since the sphericity method will pull the axis towards the particle with the highest transverse momentum.

We turn now to the experimental side of the question. Hard photon radiation in the initial state can render genuine $q\bar{q}$ events highly acollinear and produce large fluctuations in the transverse momentum distribution. In the determination of jet axis related quantities such as the p_T and p_T^2 distributions, these events were suppressed by requiring $|\cos\Theta_n| > 0.2$ where Θ_n is the angle between the normal to the event plane and the beam direction. The fraction of events which survived the Θ_n cut were 88, 87, 81 and 80 % at 14, 22, 34 and 41.5 GeV, respectively. To ensure a large acceptance for the particles in the jets, all quantities which depend on the jet axis were determined by using only events with $|\cos\Theta_{jet}| < 0.7$ where Θ_{jet} is the angle between the sphericity or thrust axis and the beam direction. Approximately, 80 % of the accepted events satisfied this condition.

The jet axis was determined with the charged particles. Table 6b lists the average angle $<\delta>$ between the measured jet axis and the primary parton direction as found from Monte Carlo generated events; $<\delta> \sim 15^0$ at W = 14 GeV and decreases to $\sim 7^0$ at W = 41.5 GeV.

The correction factors needed to determine the distributions corrected for acceptance, detector and radiative effects were calculated according to sect. 3. The "true" sphericity and thrust axes as well as the S, T and A distributions were calculated using all (charged and neutral) particles which were either prompt or produced by the decay of particles with lifetimes less than $3 \cdot 10^{-10}$ sec.

8.3 Sphericity and thrust distribution

The sphericity S and thrust T distributions which were derived from the charged particles were corrected so as to represent the S and T distributions for charged and neutral particles. The inclusion of neutrals in the corrected distributions does not significantly affect the T distributions but changes the S distributions: e.g. the average value of S at 34 GeV is reduced by ~15 %. The normalized S and T distributions at 14, 22 and 34 GeV are presented in Figs. 19, 20 and Table 7. The S (T) distributions vary rapidly at $S \lesssim 0.1$ ($T \gtrsim 0.95$), a region where the accuracy of the jet axis determination is particularly important. In this region of S (T) a ±10 % systematical uncertainty has to be added to the statistical errors shown in Figs. 19, 20. For the bulk of the data the trend to ever stronger collimation as the c.m. energy increases is clearly visible. The energy dependence of the average sphericity and thrust values, <S> and <T>, are shown in Figs. 21, 22 and Table 3. The rapid decrease of <S> with increasing W slows down or even comes to a halt above W ~ 25 GeV with <S> ~ 0.11. This behaviour is not completely reproduced by the QCD models (solid curves in Figs. 21, 22). Preliminary calculations show, however, that the inclusion of the second order ($O(\alpha_s^2)$) terms provides a good description of the data[12)]. Pure $q\bar{q}$ production (dashed curves) would predict a decreasing <S>, reaching <S> ~ 0.05 at W = 30 GeV and <S> ~ 0.03 at W = 41.5 GeV. Similar conclusions can be drawn for <1 - T> (Fig. 22).

In Fig. 23a, the angular distributions of the sphericity axis with respect to the beam axis is displayed for W = 14, 22 and 34 GeV. The distributions are well described by the form

$$\frac{1}{N}\, dN/d\cos\Theta_S \propto 1 + \cos^2\Theta_S \tag{17}$$

This result gives strong support for the hypothesis that the dominant process is $e^+e^- \to q\bar{q}$ with massless quarks and quark spin 1/2. Within errors, the angular distribution of the thrust axis (see Fig. 23b) is the same as of the sphericity axis. Fits of the form

$$\frac{1}{N}\, dN/d\cos\Theta_{S,T} \sim (1 + a_{S,T} \cos^2\Theta_{S,T})$$

shown by the curves in Fig. 23 yielded:

W = 14 GeV	$a_S = 1.09 \pm 0.16$	$a_T = 1.22 \pm 0.10$
22 GeV	$= 1.42 \pm 0.22$	$= 1.22 \pm 0.12$
34 GeV	$= 1.03 \pm 0.07$	$= 1.01 \pm 0.06.$

8.4 Event topology

Fig. 24 shows plots of the observed sphericity versus aplanarity. As illustrated in Fig. 24a collinear two-jet events lie in the left-hand corner (A, S small), uniform disk shaped events in the upper corner (A small, S large), spherical events in the lower right-hand corner while coplanar events will populate a band with A being small. The data from W = 14, 34 and 41.5 GeV (Figs. 24d-f) show that collinear events dominate at all energies. The occurrence of planar events can be seen from Fig. 25 which displays the distributions of the average squared transverse momenta in and out of the event plane, $<p_{T\ in}^2>$ and $<p_{T\ out}^2>$. As W increases the $<p_{T\ in}^2>$ distribution develops a long tail to high values of $<p_{T\ in}^2>$. Such a tail is not seen for $<p_{T\ out}^2>$.

The averages over all events, $<<p_{T\ in}^2>>$ and $<<p_{T\ out}^2>>$ are given in Fig. 26 and Table 3 as a function of W; both quantities rise with W. The rise is however, much more pronounced in $<<p_{T\ in}^2>>$ which is again related to the production of planar events. The data are well described by the QCD string model (solid curves); for the QCD independent jet model the agreement is not as good. The $p_{T\ out}$ distribution to a first approximation reflects the p_T distribution of hadrons produced in quark fragmentation. It may therefore be surprising to find that $<<p_{T\ out}^2>>$ increases with W. A study of Monte Carlo events produced according to a) $e^+e^- \rightarrow q\bar{q}$ alone (dashed curve), b) including gluon bremsstrahlung in first order (solid curve) showed that the growth of $<<p_{T\ out}^2>>$ results mainly from the larger spread of the jet axis in gluon bremsstrahlung events.

8.5 Search for heavy quarks

The aplanarity distributions (Fig. 27) can be used to set limits on the production of heavy quarks Q which near threshold would decay isotropically and therefore would give rise to events with large aplanarity A and sphericity S (see Fig. 24c). To demonstrate that A is sensitive to heavy quarks we determine the b-quark threshold using the data at W = 14 GeV. In Fig. 28 the fraction of events observed at A > 0.18 (±1 s.d. given by the shaded band) with the predictions for u,d,s,c + gluon production (dashed-dotted curve), and for u,d,s,c + gluon plus b quark production (solid curves a,b). The

$b\bar{b}$ contribution was assumed to be given a) by the asymptotic value $R_{b\bar{b}} = 1/3$ (case a); b) by the value modified for quark mass effects $R_{b\bar{b}} = 1/3\ \beta(3-\beta^2)/2$, where β is the b quark velocity (case b). It is not clear which of these is the appropriate description. The predictions are given in Fig. 28 as a function of the threshold c.m. energy, W_{thresh}, for open bottom production. We define the b quark mass* as $m_b = W_{thresh}/2$. The observed fraction of events with $A > 0.18$ is 3.5 ± 0.7 % which is significantly larger than the 1.3 % predicted for the case without b quarks. Agreement with the data is found if $b\bar{b}$ production with asymptotic strength is assumed to be present and $9.2 < W_{thresh} < 14$ GeV. The latter is in accord with the threshold for open bottom production near W = 10.5 GeV. The same method was applied in Fig. 29 to search at W = 34 GeV and 41.5 GeV for heavier quarks with charge $|e_Q| = 2/3$ (top quark) and $|e_Q| = 1/3$. The data agree well with the predictions for u,d,s,c,b + gluon alone. The additional fraction of highly aplanar events predicted for either quark charge is much too large as long as W_{thresh} is 1-2 GeV below the c.m. energy at which the data were taken. Using data at all W we can exclude the presence of additional heavy quark pair production for $5 < M_Q < 20.3$ GeV ($|e_q| = 2/3$) and $7 < M_Q < 19$ GeV ($|e_Q| = 1/3$) at 95% C.L.** A summary of results on heavy quark production from this and other experiments has been given in Ref. 39.

---

* Note that the mass found for the b quark from potential model analyses of the Υ system is somewhat lower than $\Upsilon_{thresh}/2$.

** In deriving the upper values the contribution from the five known quarks was ignored. Hence, they represent conservative limits.

9. Charged particle production with respect to the jet axis

9.1 Longitudinal and transverse momentum spectra

We studied the longitudinal and transverse momentum distributions of charged particles with respect to the jet axis. If not specified otherwise the sphericity axis was used. In Figs. 30-32 and Table 4 the longitudinal and transverse momentum distributions $1/\sigma_{tot}\ d\sigma/dp_{||}$, $1/\sigma_{tot}\ d\sigma/dp_T$ and $1/\sigma_{tot}\ d\sigma/dp_T^2$ are shown for 14, 22 and 34 GeV. The $p_{||}$ distribution resembles closely the p distribution shown in Fig. 11. As expected from phase space, the p_T distribution approaches zero as $p_T \to 0$. The p_T^2 distribution near $p_T^2 = 0$ is of the form $d\sigma/dp_T^2 \sim \exp(-a\ p_T^2)$. The p_T and p_T^2 distributions broaden with increasing c.m. energy.
For small p_T, $p_T \lesssim 0.4$ GeV/c (see insert of Fig. 31) no energy dependence of the shape of the p_T distribution is observed. In order to study this in more detail, Fig. 33 shows the ratio of the p_T distribution at 34 GeV with respect to those observed at 14 and 22 GeV, e.g.

$$F(34\ \text{GeV},\ 14\ \text{GeV}) = \frac{1/\sigma_{tot}\ d\sigma/dp_T(W = 34\ \text{GeV})}{1/\sigma_{tot}\ d\sigma/dp_T(W = 14\ \text{GeV})}$$

The ratio F is above unity which reflects the growth in multiplicity as W increases. F is almost constant for p_T up to 0.4 GeV/c and then starts to rise. The growth of the number of particles at $p_T \gtrsim 0.5$ GeV/c with increasing W can be understood as a result of hard gluon bremsstrahlung (solid curves). The dashed and dashed-dotted curves show the predictions for the case where gluon bremsstrahlung is turned off and only the process $e^+e^- \to q\bar{q}$ is considered. In this case the value of F at $p_T < 0.4$ GeV/c is well accounted for and only a small rise is predicted for $0.5 < p_T < 2$ GeV/c. The comparison suggests that hard gluon bremsstrahlung affects mostly the particle flux at $p_T \gtrsim 0.5$ GeV/c.

In Fig. 12 we compare the energy dependence of the average values $\langle p \rangle$, $\langle p_{||} \rangle$, $\langle p_T \rangle$ and $\langle p_T^2 \rangle$ (see also Table 3). The sphericity axis was used as the jet axis; $\langle p \rangle$ and $\langle p_{||} \rangle$ rise rapidly with W, while $\langle p_T \rangle$ shows only a weak increase; $\langle p_T^2 \rangle$ is also seen to rise rapidly with W. The data were fitted to following form:

$$\langle p_T^2 \rangle = a + bW \tag{18}$$

with the result $a = 0.072 \pm 0.008\ \text{GeV}^{-2}$, $b = 0.0070 \pm 0.0003$ GeV.*
The $\langle p_T \rangle$ and $\langle p_T^2 \rangle$ data agree with those by the PLUTO group[40].

---

* The errors include systematic uncertainties.

The dependence of $\langle p_T \rangle$ and $\langle p_T^2 \rangle$ on $x_{||} \equiv 2p_{||}/W$ is given in Figs. 34, 35. Since using the thrust and sphericity axes lead to noticeable differences, the data are shown for both axes. Note that at $W = 34$ GeV a difference of 0.3 GeV/c in $\langle p_T \rangle$ at $x_{||} = 0.8$ corresponds to an angle of 1.3^0 between the two axes. Due to the kinematical constraint the transverse momentum has to go to zero as $x_{||}$ approaches unity. There is, however, no kinematical constraint which would limit $\langle p_T \rangle$ at $x_{||} = 0$. $\langle p_T \rangle$ exhibits a distinct minimum near $x_{||} = 0$, a broad maximum around $x_{||} \approx 0.2$ followed by a slow decrease towards high x values.

Figs. 34, 35 demonstrate that for fixed $x_{||}$ the average values of p_T and p_T^2 change rapidly with W. Less W dependence is observed when $\langle p_T \rangle$ and $\langle p_T^2 \rangle$ are analysed for fixed $p_{||}$ (see Fig. 36). In particular for $p_{||} < 1$ GeV/c little variation with W is found.

Guided by QCD which for small values of α_s predicts p_T broadening by gluon bremsstrahlung predominantly for <u>one</u> of the two jets, we divided each event into two halves by a plane perpendicular to the jet axis and determined p_T^2 separately for the narrow and the wide jets defined by $(\Sigma p_T^2)_{\text{narrow jet}} > (\Sigma p_T^2)_{\text{wide jet}}$.

Figs. 37, 38 show $\langle p_T \rangle$ and $\langle p_T^2 \rangle$ as a function of $x_{||}$ for the narrow and the wide jet. The typical "sea-gull" shape is observed, namely small average transverse momenta for $x_{||} = 0$ and $x_{||} = 1$. The wide jet exhibits a rapid increase of $\langle p_T^2 \rangle$ with W (see also Fig. 39) which is reproduced by the QCD-models (see curves). The narrow jet also shows some increase of $\langle p_T^2 \rangle$, which is reproduced by the QCD models; the increase of $\langle p_T^2 \rangle$ for the narrow jet results mainly from a deterioration of the accuracy of the jet axis determination for events with hard gluon bremsstrahlung.

In Figs. 40-42 and Table 3 we display the normalized cross sections $1/\sigma_{tot}\, d\sigma/dx_{||}$ and $1/\sigma_{tot}\, d\sigma/dx_T$ where $x_T = 2p_T/W$. The same remarks given for $1/\sigma_{tot}\, d\sigma/dx_p$ apply also to $1/\sigma_{tot}\, d\sigma/dx_{||}$. The cross section falls steeply with $x_{||}$. At small $x_{||}$, $x_{||} < 0.1$, a strong increase with W is observed. For $x_{||} > 0.2$ the data show a slow but significant decrease with W. This is seen more clearly in Fig. 41 where $1/\sigma_{tot}\, d\sigma/dx_{||}$ is plotted for fixed $x_{||}$ intervals as a function of s. Fits of the form

$$1/\sigma_{tot}\, d\sigma/dx_{||} = c_1(1 + c_2\, \ell n(s/s_0))$$

with $s_0 = 1$ GeV^2 yielded the c_1 and c_2 values given in Table 5. The normalized cross section $1/\sigma_{tot}\, d\sigma/dx_T$ does not scale (Fig. 42): the 14 GeV data are above those from 22 and 34 GeV for $x_T \gtrsim 0.1$; however, the difference between 14 and 22 GeV is larger than between 22 and 34 GeV and it is conceivable that for $x_T \geq 0.1$ scaling in x_T is approached at large W values. Single noncollinear gluon emission, $e^+e^- \rightarrow q\bar{q}g$, at the parton level predicts scaling in x_T up to logarithmic terms.

For completeness, we present in the Appendix $x_{||}$ spectra and the dependence of $<p_T>$ on $x_{||}$ obtained by using a high momentum particle as a jet trigger as done by some ISR experiments. These distributions were compared with the unbiased ones shown in Figs. 34 and 40.

9.2 Particle spectra in terms of rapidity

The charged particle production along the jet axis was also analysed in terms of the rapidity y,

$$y = \frac{1}{2} \ln \frac{E + p_{||}}{E - p_{||}} .$$

To compute the particle energies E all particles were assumed to be pions.* The y distributions were determined using the thrust axis as the jet axis. The region of very small y values, $y \leq 0.1$, is particularly sensitive to the corrections and to the choice of the jet axis. The difference in yield obtained at larger y values $(0.1 \leq y \leq 2)$ with the thrust and sphericity axes is less than 10 %.** The intrinsic resolution at large y is approximately $\Delta y = 0.3$ due to the accuracy in determining the jet direction.

Fig. 43 and Table 8 show the rapidity distribution normalized to the total cross section $1/\sigma_{tot}\, d\sigma/dy$ at 14, 22 and 34 GeV. Note that the data were folded around y = 0. The y yield changes comparatively little over the y region starting at y = 0, called the plateau region, and then drops off rapidly at higher y values. In the plateau region, starting from y = 0, the y yield goes through a maximum which is 20 % higher than the yield at y = 0. This maximum will be discussed in more detail below. The plateau is found to broaden with increasing energy. The height of the plateau is shown in Fig. 44 for small y values $(0.1 \leq y \leq 0.2)$ and for $0.2 \leq y \leq 1$. It is found to rise with the c.m. energy in a manner similar to the pp, $p\bar{p}$ data[41-43].

---

* The rapidity distributions like all other distributions were corrected by Monte Carlo. For the "true" y distribution, y was calculated from the momenta of the final state particles assuming pion masses.

** Monte Carlo studies show,however, that the y distribution determined with the thrust axis is closer to the original distribution measured with respect to the parton direction, than if the sphericity axis was used.

In the leading particle region (y close to $y_{max} \approx \ell n(W/m)$, m particle mass) the particle yield is a steeply decreasing function of y. In order to see whether the shape of the y distribution in the leading particle region changes with energy, Fig. 45 shows the rapidity distributions plotted as a function of $y - y_{max}$. The high energy data in the leading particle again lie systematically below the low energy data. This is qualitatively to be expected from QCD effects. Note, however, that this y region is particularly affected by the jet axis determination and by the fact that all particles were assumed to be pions which will move true kaons and protons to apparent y values which are larger compared to the true ones. The importance of both effects may change with W.

9.2.1 The maximum in the rapidity distribution outside y = 0

We turn now to the maximum in the plateau region outside y = 0. The presence of this maximum is clearly seen in Fig. 46 where $1/\sigma_{tot}\, d\sigma/dy$ divided by its value at $0.1 < y \leq 0.2$* is shown as a function of y for W = 14, 22 and 34 GeV. As the c.m. energy increases the position of the maximum moves to higher y values. At W = 34 GeV the maximum is near y = 1 and the yield in the maximum is 16 ± 2 % higher than at $0.1 < y \leq 0.2$.*

We investigated whether the maximum is a result of the manner in which y is determined, namely by assigning the pion mass to all charged particles. Monte Carlo events were generated according to $e^+e^- \rightarrow q\bar{q}$ (i.e. no gluon emission) folded by fragmentation. Using the proper mass to compute y, the $\pi^\pm$, $K^\pm$ and $p,\bar{p}$ distributions are flat near y = 0 and do not exhibit a maximum outside y = 0. Assigning all particles the pion mass, the resulting y yield summed over all charged particles was again found to be flat. It appears therefore unlikely that if all particles are assigned the pion mass a y spectrum which was originally flat would have a dip near y = 0. In order to see whether heavy quark production is responsible for the effect, $c\bar{c}$ and $b\bar{b}$ events were generated. Some enhancement was found near y = 1.5 - 2 although smaller than shown by the data (dashed curve in Fig. 46b). Using the

---

* The value of the points at y > 0.2 is affected by the statistical uncertainty of $1/\sigma_{tot}\, d\sigma/dy$ at $0.1 < y < 0.2$ which is 5% at 14 and 22 GeV, and 1 % at 34 GeV. Systematic uncertainties in the corrections for $1/\sigma_{tot}\, d\sigma/dy$ at $0.1 < y < 0.2$ are of the order of 5 % and significantly smaller for larger y values. If instead of the thrust axis the sphericity axis were used, the yield in the maximum would be only ~10 % larger than at y = 0.

string model good agreement with the data is obtained when gluon emission is added to the pair production of the five quarks (solid curve in Fig. 46b and curves in Fig. 46a). This suggests that gluon emission and, to a lesser extent, heavy quark production build up the enhancement. We note, however, that the QCD independent jet model does not reproduce the enhancement.

9.3 The transverse momentum as a function of rapidity

The average values of p_T and p_T^2 are shown in Fig. 47 as a function of y for W = 14, 22 and 34 GeV. The average p_T and p_T^2 were calculated with respect to the thrust axis. The sphericity axis led to similar results. Compared to the corresponding distributions as a function of $x_{||}$ the significance of any dip near zero is greatly reduced. The average p_T and p_T^2 values near $y = 0$ increase with W. They are found to decrease steadily with increasing y.

9.4 Particle flow around the jet axis and fan invariance

Little information has been published from e^+e^- annihilation on the angular distribution of particles with respect to the jet axis. From the behaviour of the average transverse momentum as a function of the longitudinal momentum shown above it is clear that high momentum charged particles are strongly collimated around the jet axis. It is an interesting question whether collimation persists down to the lowest momenta. Another point of interest is the W dependence of the shape of the angular distribution. We present in this section the angular distribution of charged particles with respect to the thrust axis.

Fig. 48 shows the distribution of the angle α between the jet axis and the particle direction for W = 14, 22 and 34 GeV. With increasing c.m. energy there is a rapidly growing number of particles at small angles to the jet axis while the number of particles at angles $\alpha > 40^o$ is almost independent of W, the increase in yield from 14 to 34 GeV being ~20 %. For completeness Fig. 49 shows the same data as a function of $\cos\alpha$.

Fig. 50 shows the distribution of α for fixed intervals of the longitudinal momentum $p_{||}$ at W = 14, 22 and 34 GeV. The same distributions are shown in Fig. 51 with respect to $\cos\alpha$. The distributions are normalized separately to unity for each $p_{||}$ interval. Below $p_{||} = 0.2$ GeV/c the angular distribution is basically isotropic (see Fig. 51). Above $p_{||} = 0.2$ GeV/c collimation sets in; it becomes rapidly stronger as $p_{||}$ increases. The shape of the angular distribution is approximately independent of the c.m. energy. We call this phenomenon fan invariance: for fixed $p_{||}$ the particles fan out in a manner independent of W. Fan invariance in our data holds only approximately as can be seen from the following argument: The angle α is related to the transverse momentum by $p_T = p_{||}tg\alpha$. As shown in Fig. 36, the average transverse momentum $<p_T>$ for fixed $p_{||}$ changes as a function of W, in particular for $p_{||} \gtrsim 1$ GeV/c, although the change is comparatively small. The curves in Fig. 50 show the predictions of the QCD model. They agree well with the data.

In Fig. 51, 53 we show the α and $\cos\alpha$ distributions for fixed $x_{||}$ intervals. In this case the α (and $\cos\alpha$) distributions are found to change with the c.m. energy; i.e. no scaling is observed with respect to $x_{||}$. The higher the c.m. energy, the stronger is the collimation around the jet axis for the same $x_{||}$ interval.

Finally, Fig. 54 gives the momentum flow $d\Phi_p/d\alpha$ of charged particles around the jet axis. The particle momenta are normalized to the total momentum carried by charged particles in an event, Σp_i:

$$\frac{d\Phi_p}{d\alpha} = \frac{1}{N}\int dp \, \frac{p}{\Sigma p_i} \, \frac{d^2N}{dp\,d\alpha} \qquad \text{with} \quad \int d\alpha \, \frac{d\Phi_p}{d\alpha} = 1 \tag{19}$$

As the c.m. energy increases the fraction of momentum emitted at small angles to the jet axis increases rapidly, while the momentum fraction at large angles is reduced. The latter is in contrast to the particle density at large angles which actually grows slowly with W (Fig. 48).

10. Summary

We have studied charged particle production and the properties of the underlying jet structure for e^+e^- annihilation into hadrons at c.m. energies W between 12 and 43 GeV. In this energy range pair production of the five quarks u,d,s,c and b is the dominant process. Hard gluon bremsstrahlung effects change from being almost invisible at W = 12 GeV to being prominent at the high energy end.

The ratio R of the total cross section to the μ pair cross section over the full W range is consistent with a constant value of $R = 4.04 \pm 0.02 \pm 0.19$. The behaviour of R and of the transverse momentum spectra with respect to the event plane exclude the presence of heavy quarks with masses $5 < m_Q < 20.3$ GeV for a quark charge $|e_Q| = 2/3$ and $7 < m_Q < 19$ GeV for $|e_Q| = 1/3$.

The average charged particle multiplicity $<n_{CH}>$ is found to rise with energy faster than $\ell n\ s$ ($s = W^2$) if the data from lower energies are included. Good fits are obtained with the form $<n_{CH}> \sim a + b\ \ell n\ s + c\ \ell n\ s^2$ but also with a form suggested by QCD. The multiplicity distributions are found to lie between the two Poisson distributions obtained when the fact that equal numbers of positive and negative particles are produced is or is not taken into account. The multiplicity distributions obey KNO scaling to within ~20 %. The multiplicity distributions for each event hemisphere also satisfy KNO scaling to within that accuracy.

The average charged particle momentum rises almost linearly with W. The scaled momentum distribution exhibits scale breaking, $1/\sigma_{tot}\ d\sigma/dx_p$ for $x_p > 0.2$ being 25 % smaller at W = 41.5 GeV compared to W = 14 GeV. The large x behaviour of the scaled momentum distribution can be approximated by $d\sigma/dx_p \sim x_p(1-x_p)^n$ (with n = 1 to 2). Multigluon emission calculations predict $x\ d\sigma/dx$ to be distributed as a Gaussian with respect to $\ell n(1/x)$ and the position of the maximum of the Gaussian to change like $1/4\ \ell n\ s$. The measured inclusive spectra for $\pi^\pm$, $K^\pm$ and $p,\bar{p}$ are consistent with these expectations but also with the QCD model predictions for single hard gluon bremsstrahlung.

All events have been analysed with respect to a common jet axis and longitudinal and transverse momentum spectra as well as various jet measures have been studied. The angular distribution of the jet axis measured with respect to the incoming beams is of the form $1 + \cos^2\Theta$. The result gives strong support for the assumption that the underlying process is predominantly spin 1/2 quark pair production. The average sphericity decreases rapidly with c.m. energy up to W = 25 GeV and is almost constant above. At the same time the transverse momentum distributions show an excess of high p_T^2 particles, the average p_T^2 rising rapidly with W. The distribution of the average squared transverse momentum $<p_{T\ in}^2>$ in the event plane develops a long tail to large $<p_{T\ in}^2>$ values with increasing c.m. energy. This is due to the production of planar events. The observed jet broadening as well as the transverse momentum distributions are well described by gluon bremsstrahlung. A comparison of the p_T distributions at different energies suggests that hard noncollinear gluon emission contributes mainly to particles with $p_T > 0.5$ GeV/c. The rapidity distributions show a "plateau" whose width increases with W. The plateau is considerably higher than measured for pp or $p\bar{p}$ collisions. In the plateau region an enhancement is observed away from $y = 0$ which moves to larger y values as W increases. The enhancement is reproduced by the QCD string model.

The particle flux around the jet axis shows with increasing c.m. energy a rapidly growing number of particles collimated around the jet axis, while at large angles to the jet axis ($>40^0$) the particle yield is almost independent of W. Particles with $p_{||} < 0.2$ GeV/c are isotropically distributed while for $p_{||} > 0.2$ GeV/c collimation around the jet axis is observed which becomes stronger as $p_{||}$ increases. For fixed longitudinal momentum the shape of the angular distribution changes only little with W. This phenomenon we call fan invariance. A study of the charged particle momentum flow around the jet axis shows that the momentum fraction produced at small angles increases rapidly with the c.m. energy; the momentum fraction emitted at large angles decreases with W.

Acknowledgements

We gratefully acknowledge the strong support of the DESY directorate for this experiment. The data presented here have been collected over four years of running at PETRA. During that period, the indefatigable efforts of the PETRA machine group headed by D. Degele have continuously improved the performance of the storage ring and pushed its maximum energy upwards. The help of the Hallendienst and in particular of F. Schwickert and F. Czempik has been invaluable in allowing continuous upgrading of the TASSO detector. In keeping the detector operational the technical work by K.Rehlich, H.H.Sabath and K.Westphal has been indispensable. The analysis of the data has been made possible by the efficient operation of the DESY Rechenzentrum headed by P.E.Kuhlmann. We thank Mrs. E.Hell for her untiring assistance and patience with this manuscript. Those of us from outside DESY wish to thank the DESY directorate for the hospitality extended to them while working at DESY. One of us (P.M.) would like to thank A.H. Mueller (Columbia University, New York) for illuminating discussions.

Appendix

Jet studies using high momentum particles as the trigger

ISR experiments sometimes selected jet events produced in hard pp scattering by demanding that a high momentum particle is emitted at large angles[44]. The particle flow on the trigger side and on the away side are then studied (Fig. 44) with the hope that the bias introduced by the trigger for the away side is small.

In order to facilitate the comparison with e^+e^- annihilation we applied similar selection criteria to our data. Using the sphericity axis each event was subdivided into two hemispheres. If the track with the largest momentum in a hemisphere had $p_{trig} > 4$ GeV/c it was called the trigger particle and the particle properties were studied in the hemisphere of this particle (= trigger side) and in the opposite hemisphere (= away side). Similarly, the other hemisphere was searched for a trigger particle and the analysis was repeated. In the distributions presented in the following the trigger particle was not included. The distributions were compared with the unbiased distributions presented in Figs. 34, 40 above. The unbiased distributions are indicated in Figs. 56-61 by the shaded bands which represent hand drawn averages of the data of Figs. 34, 40.

Firstly, the sphericity axis determined from the particles on the away side was used as the jet axis. Fig. 55 shows $<p_T>$ as a function of $x_{||} = 2p_{||}/W$ for the trigger and away sides. In Fig. 56 the $x_{||}$ distributions are displayed for the two sides. The away side shows good agreement with the unbiased distributions. The analysis was repeated taking the momentum vector of the trigger particle as the jet axis. In this case, the trigger side distributions might be compared to the unbiased ones[44]. The results are shown in Figs. 58, 59. Large differences with respect to the unbiased results are observed. This is also true when the trigger direction is used as the jet axis and the particle distributions are determined as a function of $x_{||}^t = p_{||}/p_{trig}$ (Figs. 60, 61). In conclusion, the $<p_T>$ and $x_{||}$ distributions on the away side are in good agreement with the unbiased results while the trigger side distributions analysed as described differ markedly from their unbiased counter parts.

List of References

1. TASSO Collaboration, R.Brandelik et al., Phys.Lett. 86B (1979) 243.
2. MARK-J Collaboration, D.P.Barber et al., Phys.Rev.Lett. 43 (1979) 830;
   PLUTO Collaboration, Ch.Berger et al., Phys.Lett. 86B (1979) 418.
   JADE Collaboration, W.Bartel et al., Phys.Lett. 91B (1980) 142.
3. TASSO Collaboration, R.Brandelik et al., Phys.Lett. 94B (1980) 444; 113B (1982) 98;
   TASSO Collaboration, M.Althoff et al., Z.Phys. C17 (1983) 5;
4. TASSO Collaboration, R.Brandelik et al., Phys.Lett. 105B (1981) 75; 108B (1982) 71;
   M.Althoff et al., Phys.Lett. 126B (1983) 493; 130B (1983) 449; and DESY Report 83-121 (1983).
5. P.Hoyer et al., Nucl.Phys. B161 (1979) 34.
6. A.Ali et al., Z.Phys. C2 (1979) 33.
7. B.Andersson, G.Gustafson, T.Sjöstrand, Phys.Lett. 94B (1980) 211.
8. TASSO Collaboration, R.Brandelik et al., Phys.Lett. 83B (1979) 261; Z.Phys. C4 (1980) 87.
9. TASSO Collaboration, R.Brandelik et al., Phys.Lett. 113B (1982) 499.
10. R.D.Field, R.P.Feynman, Nucl.Phys. B136 (1978) 1.
    C.Peterson et al., Phys.Rev. D27 (1983) 105.
11. F.A.Berends and R.Kleiss, Nucl.Phys. B177 (1981) 237; B178 (1981) 141.
12. TASSO Collaboration, M.Althoff et al., publication in preparation.
13. experiments cited in P. Söding and G. Wolf, Ann.Rev.Nucl.Part.Sci. 41 (1981) 231, and recent data from
    J.L.Siegrist et al., Phys.Rev. D26 (1982) 969;
    LENA Collaboration, B.Niczyporuk et al., Z.Phys. C15 (1982) 299;
    H.Albrecht et al., Phys.Lett. 116B (1982) 383;
    JADE Collaboration, W.Bartel et al., DESY Report 83-050 (1983);
    MARK-J Collaboration, B.Adeva et al., Phys.Rev.Lett. 50 (1983) 799.
14. C.Bacci et al., Phys.Lett. 86B (1979) 234;
    LENA Collaboration, B.Niczyporuk et al., Z.Phys. C9 (1981) 1;
    M.S.Alam et al., Phys.Rev.Lett. 49 (1982) 357;
    PLUTO Collaboration, Ch.Berger et al., paper in preparation.
15. JADE Collaboration, W.Bartel et al., DESY Report 83-042 (1983).

16. G.Wolf, Proc. EPS Int. Conf. on High Energy Physics (Geneva, Switzerland, (1979), p.220.

17. JADE Collaboration, W.Bartel et al., Phys.Lett. 88B (1979) 171.

18. TASSO Collaboration, R.Brandelik et al., Phys.Lett. 89B (1980) 418.

19. G.Wolf, Proc. XI Int. Symp. Multiparticle Dynamics (Bruges, 1980), ed.by E. de Wolf, F.Verbeure, p. 283 and DESY Report 80-85 (1980).

20. E.Albini et al., Nuovo Cim. 32A (1976) 101.

21. W.Thomé et al., Nucl.Phys. B129 (1977) 365.

22. J.Slava, V.Simak, Nucl.Phys. 69B (1974) 15.

23. R.Stenbacka et al., Nuovo Cim. 51A (1979) 63.
V.V.Ammosov et al., Phys. Lett. 42B (1972) 519;
G.A.Akopdjanov et al., Nucl. Phys. B75 (1974) 401;
J.Erwin et al., Phys. Rev. Lett. 32 (1974) 254.

24. UA5 Collaboration, K.Alpgård et al., Phys.Lett. 107B (1981) 315.

25. M.Basile et al., Phys.Lett 92B (1980) 367; 95B (1980) 311.

26. J.D.Bjorken and S.J.Brodsky, Phys.Rev. D1 (1970) 1416. For a recent analysis see W.Ochs, MPI Munich preprint, MPI-PAE 118 (1983).

27. A.Bassetto, M.Ciafaloni, G.Marchesini, Phys.Lett. 83B (1978) 207.

28. K.Konishi, Rutherford Report RL 79-035 (1979).

29. W.Furmanski, S.Pokorski, Nucl.Phys. 155B (1979) 253.

30. A.H.Müller, Phys.Lett. 104B (1981) 161; Nucl.Phys. B213 (1983) 85; Columbia University Reports CU-TP-247 (1982) and CU-TP-249 (1982).

31. Z.Koba, H.B.Nielsen, P.Olesen Nucl.Phys. B40 (1972) 317.

32. TASSO Kollaboration, R.Brandelik et al., Phys.Lett. 114B (1982) 65.

33. J.F.Patrick et al., Phys.Rev.Lett. 49 (1982) 1232.

34. J.D.Bjorken, J.Kogut, Phys.Rev. D8 (1973) 1341.

35. A.Bassetto, M.Ciafaloni, G.Marchesini, A.H.Müeller, Nucl.Phys. B207 (1982) 189.

36. Y.L.Dokhshitzer, V.S.Fadin, V.A.Khoze, Phys.Lett. 115B (1982) 242; see also B.R.Webber, CERN Report TH 3713 (1983).

37. J.D.Bjorken, S.J.Brodsky, Phys.Rev. D1 (1970) 1416.

38. S.Brandt et al., Phys.Lett. 12 (1964) 57;
E.Fahri, Phys.Rev.Lett. 39 (1977) 1587.

39. S.Yamada, rapporteur talk, Int. Symp. Lepton and Photon Interactions at High Energies, Cornell, USA, 1983.

40. PLUTO Collaboration, Ch.Berger et al., DESY Report 83-054 (1983).

41. C.Bromberg et al., Phys.Rev.Lett. 31 (1973) 1563;
C.Bromberg et al., Phys.Rev. D9 (1974) 1864;
J.Whitmore et al., Phys.Rev. D10 (1974) 273;
A.Firestone et al., Phys.Rev. D10 (1974) 2080;
W.M.Morse et al., Phys.Rev. D15 (1977) 66;
C.P.Ward et al., Nucl.Phys. B153 (1979) 299.

42. UA5 Collaboration, K.Alpgård et al., Phys.Lett. 107B (1981) 310.

43. UA1 Collaboration, G.Arnison et al., Phys.Lett. 123B (1983) 108.

44. This study was triggered by H.Bøggild.

Table 1: Number of events and values for R = $\sigma_{tot}/\sigma_{\mu\mu}$ as a function of the c.m. energy. The errors quoted include the statistical as well as the point to point systematic error. An overall systematic error of ±4.5 % has to be added.

W-range	W(GeV)	L (nb^{-1})	no of evts	R
12	12	96	186	3.80±0.28
14	14	1631	2704	4.14±0.30
22	22	2785	1889	3.89±0.17
25	25	454	231	3.72±0.38
27.4-27.7	27.5	337	141	3.91±0.32
29.9-30.5	30.1	1309	460	3.94±0.18
30.5-31.5	31.1	1317	407	3.66±0.18
32.5-33.5	33.2	1581	484	4.09±0.19
33.5-34.5	34.0	12650	3706	4.12±0.11
34.5-35.5	34.7	59581	16746	4.08±0.09
35.5-36.7	36.1	2213	548	3.93±0.19
38.7-43.1	41.4	6485	1219	4.06±0.29

Table 2: Charged particle multiplicity distributions, 1/N dN/dn_{CH}

Multiplicity	W=14 GeV	W=22 GeV	W=34 GeV
0	0.001±0.001	0.000±0.000	0.000±0.000
2	0.017±0.008	0.005±0.003	0.003±0.002
4	0.076±0.010	0.028±0.007	0.015±0.008
6	0.172±0.011	0.085±0.010	0.043±0.002
8	0.248±0.013	0.173±0.013	0.088±0.003
10	0.226±0.015	0.208±0.014	0.146±0.003
12	0.148±0.015	0.204±0.017	0.185±0.004
14	0.072±0.012	0.140±0.017	0.180±0.005
16	0.027±0.009	0.086±0.015	0.142±0.005
18	0.009±0.005	0.041±0.015	0.092±0.004
20	0.003±0.002	0.018±0.010	0.052±0.004
22	0.001±0.001	0.007±0.004	0.028±0.003
24		0.002±0.001	0.015±0.003
26		0.001±0.001	0.006±0.002
28			0.002±0.001

Table 3: Average values for track and event parameters. The sphericity axis was used as the jet axis; only statistical errors are given.

	W=12 GeV	W=14 GeV	W=22 GeV	W=25 GeV	W=30.5GeV	W=34.5GeV	W=41.5GeV
$<n_{CH}>$	8.48±0.21	9.08±0.05	11.22±0.07	11.69±0.24	12.79±0.13	13.48±0.030	14.41±0.24
$<f_{CH}>$	0.59±0.02	0.58±0.01	0.58±0.01	0.58±0.02	0.60±0.01	0.59±0.002	0.58±0.015
D		3.24±0.08	3.81±0.25			4.46±0.05	
$<S>$	0.255±0.017	0.213±0.004	0.145±0.004	0.127±0.009	0.112±0.006	0.108±0.001	0.108±0.005
$<T>$	0.840±0.008	0.855±0.002	0.884±0.002	0.898±0.005	0.900±0.003	0.902±0.001	0.905±0.003
$<p>$ (GeV/c)	0.841±0.021	0.895±0.006	1.163±0.010	1.233±0.032	1.424±0.019	1.512±0.004	1.671±0.019
$<p_{\|\|}>$ (GeV/c)	0.683±0.023	0.756±0.007	1.019±0.011	1.075±0.031	1.281±0.022	1.350±0.005	1.523±0.022
$<p_T>$ (GeV/c)	0.340±0.007	0.334±0.002	0.377±0.003	0.368±0.007	0.404±0.004	0.422±0.001	0.448±0.004
$<p_T^2>$ (GeV/c^2	0.171±0.008	0.168±0.002	0.232±0.004	0.213±0.009	0.281±0.008	0.311±0.002	0.350±0.009
$<p^2_{Tin}>$ (GeV/c)^2	0.128±0.009	0.131±0.002	0.184±0.009	0.161±0.011	0.223±0.012	0.251±0.003	0.280±0.012
$<p^2_{Tout}>$ (GeV/c)^2	0.044±0.002	0.044±0.001	0.059±0.002	0.055±0.002	0.061±0.002	0.068±0.001	0.075±0.002

Table 4a: Normalized momentum distributions, $1/\sigma_{tot}\ d\sigma/dp$ $(\mathrm{GeV/c})^{-1}$

p (GeV/c)	**W=14 GeV**	**W=22 GeV**	**W=34 GeV**
0.10-0.20	6.224±0.184	6.248±0.214	6.298±0.076
0.20-0.30	10.340±0.230	10.270±0.275	10.670±0.099
0.30-0.40	9.898±0.225	10.110±0.272	10.510±0.098
0.40-0.50	8.592±0.205	9.045±0.258	9.628±0.094
0.50-0.60	7.251±0.188	7.885±0.241	8.546±0.088
0.60-0.70	5.840±0.167	7.236±0.231	7.737±0.084
0.70-0.80	4.957±0.154	6.207±0.214	6.638±0.078
0.80-1.00	3.934±0.096	5.028±0.136	5.495±0.050
1.00-1.20	2.893±0.083	3.836±0.119	4.294±0.044
1.20-1.40	2.204±0.073	2.883±0.103	3.534±0.040
1.40-1.60	1.778±0.066	2.264±0.091	2.778±0.036
1.60-1.80	1.315±0.057	1.951±0.085	2.465±0.034
1.80-2.00	1.077±0.052	1.422±0.073	2.088±0.031
2.00-2.20	0.835±0.046	1.352±0.071	1.710±0.028
2.20-2.40	0.751±0.044	1.097±0.064	1.510±0.026
2.40-2.60	0.523±0.037	0.816±0.055	1.238±0.024
2.60-2.80	0.384±0.032	0.811±0.055	1.124±0.023
2.80-3.00	0.342±0.030	0.631±0.049	0.960±0.021
3.00-3.50	0.209±0.015	0.484±0.027	0.802±0.012
3.50-4.00	0.134±0.012	0.307±0.021	0.586±0.011
4.00-6.00	0.036±0.003	0.144±0.008	0.295±0.004
6.00-8.00		0.038±0.004	0.117±0.003
8.00-10.00			0.046±0.002
10.00-12.00			0.008± 0.001

Table 4b: Normalized scaled momentum distributions, $1/\sigma_{tot}\ d\sigma/dx_p$, where $x_p = 2p/W$.

x_p	W=14 GeV	W=22 GeV	W=34 GeV
0.02-0.03	54.98± 3.46	116.80±7.700	162.60±21.50
0.03-0.04	66.40± 4.12	110.50±6.600	135.80±15.50
0.04-0.05	68.14± 4.20	93.30±5.200	106.80± 9.50
0.05-0.06	61.42± 3.84	85.80±4.500	85.80± 5.70
0.06-0.08	56.72± 3.40	64.90±3.200	62.70± 3.50
0.08-0.10	42.79± 2.60	49.50±2.400	45.10± 1.60
0.10-0.12	34.70± 2.16	34.20±1.600	34.00± 0.90
0.12-0.14	28.11± 1.77	27.00±1.400	25.72± 0.68
0.14-0.16	21.56± 1.41	21.20±1.100	19.50± 0.53
0.16-0.18	19.10± 1.24	16.72±0.960	16.38± 0.48
0.18-0.20	15.04± 1.02	14.23±0.870	13.34± 0.39
0.20-0.25	11.58± 0.72	10.13±0.520	9.23± 0.25
0.25-0.30	7.41± 0.50	6.71± 0.40	5.69± 0.17
0.30-0.35	5.25± 0.36	4.22± 0.29	3.66± 0.11
0.35-0.40	3.32± 0.25	2.95± 0.23	2.56± 0.10
0.40-0.50	1.83± 0.14	1.55± 0.11	1.41± 0.10
0.50-0.60	0.93± 0.09	0.78± 0.08	0.66± 0.04
0.60-0.70	0.40± 0.05	0.38± 0.05	0.36± 0.03
0.70-0.80	0.21± 0.04	0.21± 0.04	0.19± 0.04

Table 4c: Normalized longitudinal momentum distributions, $1/\sigma_{tot}\ d\sigma/dp_{||}$ $(\mathrm{GeV}/c)^{-1}$

$P_{\|\|}$ (GeV/c)	W=14 GeV	W=22 GeV	W=34 GeV
0.00-0.05	8.732±0.292	7.881±0.328	8.454±0.120
0.05-0.10	9.431±0.304	9.595±0.364	9.394±0.127
0.10-0.15	11.710±0.339	11.060±0.392	12.450±0.147
0.15-0.20	11.050±0.329	11.970±0.410	12.450±0.147
0.20-0.25	10.820±0.326	10.545±0.387	11.630±0.143
0.25-0.30	8.866±0.296	9.804±0.375	10.520±0.137
0.30-0.35	8.621±0.292	9.139±0.364	9.640±0.131
0.35-0.40	7.690±0.276	8.342±0.349	8.849±0.126
0.40-0.45	6.574±0.256	7.526±0.333	8.423±0.124
0.45-0.50	6.161±0.248	7.346±0.330	7.639±0.118
0.50-0.60	5.250±0.162	6.703±0.224	7.037±0.080
0.60-0.70	4.448±0.150	5.393±0.202	6.153±0.076
0.70-0.80	3.875±0.140	4.909±0.194	5.454±0.072
0.80-0.90	3.348±0.130	4.630±0.189	4.882±0.068
0.90-1.00	2.850±0.120	3.833±0.173	4.392±0.065
1.00-1.20	2.517±0.080	3.269±0.113	3.675±0.042
1.20-1.40	1.950±0.071	2.591±0.101	3.068±0.039
1.40-1.60	1.538±0.063	2.111±0.091	2.558±0.035
1.60-1.80	1.199±0.055	1.661±0.081	2.222±0.033
1.80-2.00	0.958±0.050	1.358±0.073	1.847±0.030
2.00-3.00	0.483±0.015	0.822±0.025	1.181±0.011
3.00-4.00	0.145±0.008	0.356±0.025	0.642±0.008
4.00-5.00	0.046±0.005	0.174±0.011	0.337±0.006
5.00-6.00		0.080±0.008	0.206± 0.004
6.00-8.00		0.032±0.003	0.107± 0.002
8.00-10.00			0.041± 0.002
10.00-12.00			0.019± 0.001
12.00-14.00			0.007± 0.001

Table 4d: Normalized transverse momentum distributions $1/\sigma_{tot}\ d\sigma/dp_T$ $(GeV/c)^{-1}$

p_T(GeV/c)	W=14 GeV	W=22 GeV	W=34 GeV
0.00-0.05	5.609±0.250	6.432±0.328	8.030±0.112
0.05-0.10	12.960±0.380	15.710±0.513	17.192±0.164
0.10-0.15	18.990±0.460	20.350±0.584	23.270±0.191
0.15-0.20	20.750±0.481	23.300±0.625	25.420±0.199
0.20-0.25	19.890±0.471	22.280±0.611	24.630±0.196
0.25-0.30	18.790±0.458	21.860±0.605	22.820±0.189
0.30-0.35	16.150±0.424	18.460±0.556	20.670±0.180
0.35-0.40	13.510±0.388	16.160±0.520	17.900±0.167
0.40-0.45	10.780±0.347	13.160±0.470	15.430±0.155
0.45-0.50	8.586±0.309	11.200±0.433	13.020±0.143
0.50-0.60	5.926±0.182	8.022±0.259	10.230±0.089
0.60-0.70	3.841±0.146	5.619±0.217	7.326±0.075
0.70-0.80	2.052±0.107	3.718±0.177	5.222±0.064
0.80-0.90	1.399±0.088	2.387±0.141	3.712±0.054
0.90-1.00	0.675±0.061	1.692±0.119	2.667±0.045
1.00-1.20	0.565±0.045	0.961±0.065	1.712±0.026
1.20-1.40	0.176±0.026	0.448±0.045	0.976±0.019
1.40-1.60	0.088±0.019	0.242±0.033	0.572± 0.015
1.60-1.80	0.031±0.012	0.177±0.029	0.368± 0.012
1.80-2.00	0.027±0.011	0.105±0.022	0.232± 0.009
2.00-2.50	0.005±0.003	0.047±0.010	0.114± 0.004
2.50-3.00		0.015±0.007	0.043± 0.003
3.00-4.00			0.012± 0.001
4.00-6.00			0.0014± 0.000
6.00-8.00			0.0004± 0.000

Table 4e: Normalized distributions of the transverse momentum squared $1/\sigma_{tot}\ d\sigma/dp_T^2$ $(\mathrm{GeV}/c)^{-2}$

p_T^2 $(\mathrm{GeV}/c)^2$	W=14 GeV	W=22 GeV	W=34 GeV
0.00–0.01	92.820±2.275	110.702±3.050	125.600±0.991
0.01–0.02	75.870±2.057	82.320±2.620	94.650±0.861
0.02–0.04	61.390±1.308	67.950±1.690	73.780±0.538
0.04–0.06	45.260±1.123	49.950±1.449	55.280±0.465
0.06–0.08	36.370±1.007	41.160±1.313	44.160±0.416
0.08–0.10	29.040±0.900	35.720±1.223	36.420±0.377
0.10–0.12	23.530±0.810	26.550±1.054	30.820±0.347
0.12–0.14	19.600±0.739	22.530±0.971	25.880±0.318
0.14–0.16	17.030±0.689	20.980±0.937	22.510±0.297
0.16–0.18	13.630±0.617	16.880±0.841	20.340±0.282
0.18–0.20	12.160±0.582	14.530±0.780	16.430±0.253
0.20–0.25	9.055±0.318	11.810±0.445	13.810±0.147
0.25–0.30	6.468±0.269	8.224±0.371	10.860±0.130
0.30–0.35	4.661±0.228	6.466±0.329	8.262±0.114
0.35–0.40	3.546±0.199	5.578±0.306	6.826±0.103
0.40–0.60	2.024±0.075	3.204±0.116	4.402±0.041
0.60–0.80	0.884±0.050	1.541±0.080	2.320±0.030
0.80–1.20	0.314±0.021	0.714±0.039	1.184±0.015
1.20–1.60	0.123±0.013	0.287±0.025	0.576±0.011
1.60–2.00	0.038±0.007	0.130±0.016	0.322±0.008
2.00–3.00	0.019±0.004	0.069±0.008	0.157±0.004
3.00–4.00	0.0077±0.0027	0.030±0.005	0.066±0.002
4.00–6.00	0.0018±0.0010	0.012±0.003	0.026±0.001
6.00–8.00		0.003±0.002	0.0098±0.0006
8.00–10.00			0.0049±0.0004
10.00–12.00			0.0023±0.0003
12.00–14.00			0.0013±0.0003
14.00–16.00			0.0011±0.0002
16.00–18.00			0.00065±0.00018
18.00–20.00			0.00029±0.00013
20.00–30.00			0.00020±0.00009
30.00–40.00			0.00003±0.00002

Table 4f: Distributions of the scaled parallel momentum, $1/\sigma_{tot}\ d\sigma/dx_{||}$, where $x_{||} = 2P_{||}/W$.

$x_{\|\|}$	W=14 GeV	W=22 GeV	W=34 GeV
0.02-0.03	77.40± 3.46	114.50±7.940	143.90±21.50
0.03-0.04	70.50± 4.12	91.60±6.500	112.30±14.50
0.04-0.05	60.64± 3.20	79.50±4.500	89.40± 9.00
0.05-0.06	51.00± 3.14	62.84±4.000	72.90± 5.10
0.06-0.08	41.30± 2.90	49.50±1.340	54.90± 2.70
0.08-0.10	31.40± 2.00	37.30±1.900	39.80± 1.40
0.10-0.12	25.20± 1.60	29.10±1.300	30.90± 0.80
0.12-0.14	21.70± 1.53	21.10±1.000	23.42± 0.60
0.14-0.16	17.90± 1.21	18.60±0.900	18.30± 0.53
0.16-0.18	15.50± 1.12	13.40±0.840	14.70± 0.40
0.18-0.20	12.50± 0.95	12.20±0.800	12.40± 0.35
0.20-0.25	9.40± 0.72	8.72±0.510	8.63± 0.25
0.25-0.30	6.35± 0.45	5.80± 0.39	5.26± 0.17
0.30-0.35	4.35± 0.36	3.76± 0.28	3.49± 0.11
0.35-0.40	2.75± 0.25	2.80± 0.23	2.37± 0.10
0.40-0.50	1.58± 0.09	1.48± 0.11	1.27± 0.08
0.50-0.60	0.88± 0.07	0.70± 0.07	0.63± 0.02
0.60-0.80	0.26± 0.04	0.28± 0.05	0.24± 0.02

Table 4g: Distributions of the scaled transverse momentum, $1/\sigma_{tot}\ d\sigma/dx_T$, where $x_T = 2p_T/W$.

x_T	W=14 GeV	W=22 GeV	W=34 GeV
0.00-0.01	52.52±1.74	126.10±3.22	301.00±1.55
0.01-0.02	115.70±2.54	241.70±4.47	400.60±1.78
0.02-0.03	143.80±2.80	232.70±4.40	261.00±1.43
0.03-0.04	132.80±2.67	169.40±3.76	148.30±1.07
0.04-0.05	112.20±2.45	113.30±3.09	82.40±0.80
0.05-0.06	86.41±2.16	74.85±2.51	46.61±0.60
0.06-0.07	65.99±1.90	46.91±2.00	27.82±0.46
0.07-0.08	46.15±1.61	29.78±1.59	17.13±0.37
0.08-0.09	33.84±1.39	20.81±1.34	10.72±0.29
0.09-0.10	26.78±1.26	12.34±1.03	7.35±0.24
0.10-0.12	15.26±0.69	6.67±0.54	4.25±0.13
0.12-0.14	7.49±0.50	3.56±0.40	1.98±0.09
0.14-0.16	4.89±0.42	1.91±0.29	1.05±0.07
0.16-0.18	2.65±0.32	1.31±0.25	0.54±0.05
0.18-0.20	1.02±0.21	1.06±0.21	0.27±0.03
0.20-0.25	0.48±0.09	0.18±0.06	0.12±0.02
0.25-0.30	0.20±0.06	0.08±0.05	0.03±0.01
0.30-0.40	0.01±0.01		0.008±0.002

Table 5a: Fit results to the s-dependence of the scaled cross section $1/\sigma_{tot}\ d\sigma/dx_p = c_1 \cdot (1+c_2 \cdot \ell n(s/s_o))$ where $s_o = 1\ \mathrm{GeV}^2$

x_p	c_1	c_2
0.02-0.05	0.50±0.05	25.30 ±2.49
0.05-0.10	1.97±0.87	0.318 ±0.08
0.10-0.20	26.80±1.40	-0.022±0.008
0.20-0.30	14.99±0.81	-0.071±0.005
0.40-0.50	7.27±0.54	-0.081±0.006
0.40-0.50	3.29±0.37	-0.084±0.008
0.50-0.70	1.09±0.16	-0.075±0.012

Table 5b: Fit results to the s-dependence of the scaled cross section $1/\sigma_{tot}\ d\sigma/dx_{||} = c_1 \cdot (1+c_2 \cdot \ell n(s/s_o))$ where $s_o = 1\ \mathrm{GeV}^2$

$x_{\|\|}$	c_1	c_2
0.02-0.05	0.54±0.01	27.7 ±0.33
0.05-0.10	2.95±0.01	2.36 ±0.03
0.10-0.20	15.86±1.00	0.032±0.012
0.20-0.30	11.55±0.72	-0.059±0.006
0.30-0.40	5.72±0.49	-0.069±0.007
0.40-0.50	2.56±0.49	-0.071±0.007
0.50-0.70	0.94±0.30	-0.069±0.025

Table 6: Monte Carlo calculation of the angle between the jet axis determined by thrust or sphericity and the direction of the most energetic parton. QED radiative effects were turned off.

a) for an ideal detector and using charged and neutrals.

	sphericity		thrust	
W (GeV)	$q\bar{q}$	$q\bar{q}+q\bar{q}g$	$q\bar{q}$	$q\bar{q}+q\bar{q}g$
14	5.5°	8.2°	6.8°	9.2°
22	2.8°	5.7°	3.7°	5.9°
34	1.6°	5.4°	2.3°	4.6°
41.5	1.3°	5.2°	1.8°	4.4°

b) for the TASSO detector and using only charged particles.

	sphericity		thrust	
W (GeV)	$q\bar{q}$	$q\bar{q}+q\bar{q}g$	$q\bar{q}$	$q\bar{q}+q\bar{q}g$
14	12.2°	14.0°	13.1°	14.7°
22	6.2°	10.3°	7.4°	10.5°
34	3.5°	8.2°	4.1°	8.1°
41.5	3.0°	7.4°	3.6°	6.8°

Table 7a: Normalized sphericity distributions, 1/N dN/dS

Sphericity	W=14 GeV	W=22 GeV	W=34 GeV
0.000–0.025	1.14±0.15	2.22±0.23	6.29±0.16
0.025–0.050	2.72±0.24	6.23±0.46	8.87±0.20
0.050–0.075	3.87±0.29	6.55±0.48	5.77±0.15
0.075–0.100	4.21±0.30	5.06±0.41	4.12±0.12
0.100–0.150	3.68±0.20	3.01±0.21	2.70±0.07
0.150–0.200	2.63±0.16	2.26±0.17	1.58±0.05
0.200–0.250	1.67±0.13	1.32±0.13	1.14±0.04
0.250–0.300	1.44±0.11	0.92±0.10	0.68±0.03
0.300–0.350	1.03±0.09	0.72±0.09	0.45±0.02
0.350–0.400	0.99±0.09	0.58±0.08	0.29±0.02
0.400–0.450	0.55±0.07	0.30±0.05	0.19±0.01
0.450–0.500	0.51±0.06	0.34±0.06	0.13±0.01
0.500–0.550	0.37±0.05	0.17±0.04	0.11±0.01
0.550–0.600	0.39±0.06	0.10±0.03	0.10±0.01
0.600–0.650	0.33±0.05	0.13±0.03	0.07±0.01
0.650–0.700	0.26±0.05	0.11±0.03	0.04±0.01

Table 7b: Normalized thrust distributions, 1/N dN/dT

Thrust	W=14 GeV	W=22 GeV	W=34 GeV
0.60–0.64	0.34±0.07	0.05±0.03	0.02±0.01
0.64–0.68	0.44±0.07	0.24±0.06	0.11±0.01
0.68–0.72	1.17±0.11	0.50±0.08	0.26±0.02
0.72–0.76	1.56±0.12	0.90±0.11	0.48±0.02
0.76–0.80	2.17±0.16	1.38±0.14	0.92±0.04
0.80–0.84	3.32±0.20	2.53±0.20	1.97±0.06
0.84–0.88	4.08±0.22	3.84±0.25	3.02±0.08
0.88–0.90	5.36±0.36	5.46±0.43	4.40±0.13
0.90–0.92	5.67±0.37	6.25±0.46	5.76±0.15
0.92–0.94	5.63±0.35	7.74±0.54	8.11±0.19
0.94–0.96	4.04±0.29	6.80±0.46	9.70±0.21
0.96–0.98	2.55±0.23	3.82±0.33	6.64±0.16
0.98–1.00	0.59±0.11	0.93±0.15	1.86±0.08

Table 8: Normalized rapidity distributions, $1/\sigma_{tot}\ d\sigma/dy$
(folded around $y = 0$)

Rapidity	W=14 GeV	W=22 GeV	W=34 GeV
0.-0.2	3.74±0.13	3.77±0.15	4.10±0.05
0.2-0.4	4.05±0.11	4.00±0.13	4.50±0.05
0.4-0.6	3.98±0.10	4.31±0.15	4.69±0.05
0.6-0.8	4.22±0.10	4.57±0.12	4.88±0.05
0.8-1.0	3.97±0.09	4.50±0.13	4.99±0.05
1.0-1.2	3.89±0.09	4.54±0.13	4.99±0.05
1.2-1.4	3.71±0.09	4.54±0.13	4.94±0.05
1.4-1.6	3.30±0.08	4.31±0.13	4.80±0.05
1.6-1.8	3.10±0.08	4.02±0.12	4.68±0.05
1.8-2.0	2.60±0.07	3.61±0.13	4.43±0.04
2.0-2.2	2.11±0.07	3.03±0.11	3.94±0.04
2.2-2.4	1.68±0.06	2.67±0.10	3.53±0.04
2.4-2.6	1.31±0.06	2.26±0.09	2.93±0.04
2.6-2.8	0.99±0.05	1.65±0.08	2.49±0.04
2.8-3.0	0.62±0.04	1.09±0.07	1.85±0.03
3.0-3.2	0.43±0.03	0.67±0.05	1.42±0.03
3.2-3.4	0.19±0.02	0.55±0.05	1.05±0.03
3.4-3.6	0.12±0.02	0.34±0.04	0.71±0.02
3.6-3.8	0.05±0.01	0.20±0.03	0.50±0.02
3.8-4.0	0.03±0.01	0.08±0.02	0.30±0.01
4.0-4.2		0.05±0.02	0.18±0.01
4.2-4.4		0.04±0.02	0.09±0.01
4.4-4.6			0.06±0.01
4.6-4.8			0.03±0.01

Figure Captions

1) The ratio $R = \sigma(e^+e^- \rightarrow \text{hadrons})/\sigma_{\mu\mu}$ where $\sigma_{\mu\mu} = 4\pi\alpha^2/3s$. The data from other experiments were taken from Ref. 18.

2) The unfolded distribution of the charged multiplicity n_{CH} at W = 14, 22 and 34 GeV. The curves show two kinds of Poisson distributions (see text) computed for the measured average charge multiplicity.

3) Average charged particle multiplicity as a function of the c.m. energy W from this experiment (ϕ) and from other e^+e^- experiments(19,20).

4) Average charged particle multiplicity in e^+e^- annihilation as a function of the c.m. energy. Also shown are the QCD model prediction for $e^+e^- \rightarrow q\bar{q}$, $q\bar{q}g$ (solid curve) and the prediction for $e^+e^- \rightarrow q\bar{q}$ (dashed curve) summed over all possible quark flavours.

5) Average charged particle multiplicity as a function of the c.m. energy W from this and other e^+e^- experiments(19,20). Also shown are the data for pp and $p\bar{p}$ collisions(25,26). The curves show fits to the e^+e^- and pp,$p\bar{p}$ data (see text).

6) The dispersion $D = (\langle n_{CH}^2\rangle - \langle n_{CH}\rangle^2)^{1/2}$ of the charged particle multiplicity distribution as a function of the c.m. energy W as measured by this (ϕ) and other e^+e^- experiments(19,20).

7) The dispersion $D = (\langle n_{CH}^2\rangle - \langle n_{CH}\rangle^2)^{1/2}$ of the charged particle multiplicity distribution as a function of the c.m. energy W as measured in e^+e^-, pp and $p\bar{p}$ experiments(19,25,26).

8a) The charged particle multiplicity distribution $P(n_{CH})$ multiplied by the average charged particle multiplicity $\langle n_{CH}\rangle$ as a function of the ratio $n_{CH}/\langle n_{CH}\rangle$ from this experiment at 14, 22 and 34 GeV and other e^+e^- experiments(19).

b) Same as a) as measured in this experiment at W = 34 GeV and data from $p\bar{p}$ annihilation (curve)(25) and $p\bar{p}$ scattering at a c.m. energy of 540 GeV(26).

9a) The ratio $\langle n_{CH}\rangle/D$ as a function of the c.m. energy as measured in this and other e^+e^- experiments(19,20).

b) Same as in a) for e^+e^- (19,20), pp(25) and $p\bar{p}$(26) data. The straight lines are drawn to guide the eye.

10) $e^+e^- \to$ hadrons. Each event is separated into two hemispheres by means of the sphericity axis. Shown is for each hemisphere the charged multiplicity distribution $P(n_{CH})$ multiplied by the average charged particle multiplicity $\langle n_{CH}\rangle$ as a function of $n_{CH}/\langle n_{CH}\rangle$ for W = 14, 22 and 34 GeV.

11) The charged particle momentum spectrum $1/\sigma_{tot}\, d\sigma/dp$ at W = 14, 22 and 34 GeV.

12) The average values of the total, transverse and longitudinal momentum and of the transverse momentum squared, $\langle p\rangle$, $\langle p_{||}\rangle$, $\langle p_T\rangle$ and $\langle p_T^2\rangle$, as a function of the c.m. energy W. The solid curves show the predictions of the QCD independent jet model for $e^+e^- \to q\bar{q}, q\bar{q}g$; the dashed curves show the prediction for $e^+e^- \to q\bar{q}$.

13) The normalized scaled cross section $1/\sigma_{tot}\, d\sigma/dx_p$ as a function of $x_p = 2p/W$ for W = 14, 22 and 34 GeV.

14) $1/\sigma_{tot}\, d\sigma/dx_p$ for fixed x_p intervals as a function of $s = W^2$.

15) The normalized scaled cross section $1/\sigma_{tot}\, d\sigma/dx_p$ multiplied by the function $f = x_p/(1 - x_p)^n$ for n = 1, 2 and 3 as a function of x_p for W = 34 GeV.

16a) The normalized quantity $x_p \cdot 1/\sigma_{tot}\, d\sigma/dx_p$ as a function of $\ell n\,(1/x_p)$ for W = 14, 22 and 34 GeV.

b) The normalized quantity $x_p\, 1/\sigma_{tot}\, d\sigma/dx_p$ for the prompt charged particles (dashed curve) and for the final particles (solid curve) as calculated with the QCD model.

17a) The quantity $x_p\, 1/\sigma_{tot}\, d\sigma/dx_p$ versus $\ell n\,(1/x_p)$ for $\pi^+ + \pi^-$, $K^+ + K^-$, $p + \bar{p}$ at W = 14, 22 and 34 GeV. The curves are drawn to guide the eye.

b) The position of the maximum, $(\ell n\,(1/x_p))_{max}$, of $x_p\, d\sigma/dx_p$ as a function of s for all charged particles, and for $\pi^\pm$, $K^\pm$ and $p,\bar{p}$. The straight lines are proportional to $1/4\ \ell ns$.

18) $1/\sigma_{tot}\, d\sigma/dp_T^2$ at W = 34 GeV evaluated with respect to the sphericity axis (⧫) and the thrust axis (✱).

19) The normalized sphericity distributions at W = 14, 22 and 34 GeV.

20) The normalized thrust distributions at W = 14, 22 and 34 GeV.

21) The average sphericity as a function of the c.m. energy W. The solid curve shows the prediction of the QCD independent jet model for $e^+e^- \to q\bar{q}, q\bar{q}g$. The dashed curve shows the prediction for $e^+e^- \to q\bar{q}$.

22) The average value of 1-thrust, <1 - T>, as a function of the c.m. energy W. The curve shows the prediction of the QCD independent jet model for $e^+e^- \to q\bar{q}, q\bar{q}g$. The dashed curve shows the prediction for $e^+e^- \to q\bar{q}$.

23a) The angular distribution of the jet axis determined by sphericity at W = 14, 22 and 34 GeV. The curves are proportional to $1 + \cos^2\Theta_S$.

b) The angular distribution of the jet axis determined by thrust at W = 14, 22 and 34 GeV. The curves are proportional to $1 + \cos^2\Theta_T$.

24) The distribution of sphericity versus aplanarity.

a) schematic diagram

b) distribution predicted for W = 34 GeV by the QCD string model for 1100 accepted events

c) distribution predicted for pair production of top quarks with a mass of 16 GeV at W = 34 GeV for 650 accepted events.

d)-f) measured distributions at W = 14 (2704 accepted events), 34 (20452) and 41.5 GeV (1219).

25) Distribution of the transverse momentum squared out of the event plane $<p_{T\,out}^2>$ and in the event plane, $<p_{T\,in}^2>$, averaged over the event, at W = 14, 22, 34 and 41.5 GeV.

26) The average momentum squared in and out of the event plane, $<<p_{T\,in}^2>>$ and $<<p_{T\,out}^2>>$, averaged over all events, as a function of the c.m. energy W. The curves show the prediction of the QCD string model; for $e^+e^- \to q\bar{q}, q\bar{q}g$ (solid) and $e^+e^- \to q\bar{q}$ (dashed).

27) The normalized aplanarity distributions at W = 14, 22 and 34 GeV.

28) The fraction of events with A > 0.18 at W = 14 GeV. The dashed band shows the ±1 s.d. band for the observed event fraction. The dashed-dotted line shows the QCD model prediction for u,d,s,c + gluon. The solid curves show the QCD prediction including an asymptotic b-quark contribution ($R_{b\bar{b}} = 1/3$) and a b-quark contribution with the threshold factor ($R_{b\bar{b}} = 1/3\ \beta(3-\beta^2)/2$). W_{thresh} is the assumed threshold for open b production, $W_{thresh} = 2m_b$ where m_b is the b-quark mass.

29) The fraction of events with A > 0.18 GeV at W = 34 (a) and 41.5 GeV (b). The dashed bands show the ±1 s.d. band for the observed fraction. The dashed-dotted lines show the QCD prediction for five quarks. The solid curves show the QCD prediction including a sixth quark of charge 2/3 or 1/3 with either an asymptotic contribution or including the threshold factor. W_{thresh} is the assumed $Q\bar{Q}$ threshold, $W_{thresh} = 2m_Q$, where m_Q is the quark mass.

30) Normalized differential cross section for the momentum component parallel to the jet axis (= sphericity axis), $p_{||}$, for W = 14, 22 and 34 GeV.

31) Normalized differential cross section for the momentum component transverse to the jet axis (= sphericity axis), p_T, for W = 14, 22, 34 and 41.5 GeV.

32) Normalized differential cross section for the square of the momentum component transverse to the jet axis (= sphericity axis), p_T^2, for W = 14, 22, 34 and 41.5 GeV.

33) Ratio F of the normalized differential cross sections

(a) $F = \frac{1/\sigma_{tot}\ d\sigma/dp_T\ (W = 34\ \text{GeV})}{1/\sigma_{tot}\ d\sigma/dp_T\ (W = 22\ \text{GeV})}$

(b) $F = \frac{1/\sigma_{tot}\ d\sigma/dp_T\ (W = 34\ \text{GeV})}{1/\sigma_{tot}\ d\sigma/dp_T\ (W = 14\ \text{GeV})}$

as a function of p_T. The solid and dotted curves show the prediction of the QCD independent jet model for $e^+e^- \to q\bar{q}, q\bar{q}g$. The dashed and dashed-dotted curves show the predictions for $e^+e^- \to q\bar{q}$.

34) The average transverse momentum $<p_T>$ as a function of the fractional longitudinal momentum $x_{||} = 2p_{||}/W$ with respect to the jet axis at W = 14, 22 and 34 GeV.

a) using the sphericity axis

b) using the thrust axis.

The curves show the predictions of the QCD independent jet model.

35) Same as Fig. 34 for the square of the transverse momentum, p_T^2.

36a) The average transverse momentum p_T as a function of the longitudinal momentum $p_{||}$ at W = 14, 22 and 34 GeV. The thrust axis was used.

b) Same as a) for the square of the transverse momentum.

37) The average transverse momentum $<p_T>$ as a function of $x_{||} = 2p_{||}/W$ separately for the narrow and the wide jet at W = 14, 22 and 34 GeV.

a) using the sphericity axis

b) using the thrust axis.

The curves show the predictions of the QCD independent jet model.

38) Same as Fig. 37 for the square of the transverse momentum, p_T^2.

39) The average transverse momentum squared for the narrow and the wide jet as a function of the c.m. energy W. The solid curves show the predictions of the QCD string model. The dashed curves show the predictions for $e^+e^- \rightarrow q\bar{q}$.

40) The normalized differential cross section $1/\sigma_{tot}\ d\sigma/dx_{||}$ as a function of $x_{||} = 2p\ /W$ at W = 14, 22 and 34 GeV. The sphericity axis was used as the jet axis.

41) The normalized differential cross section $1/\sigma_{tot}\ d\sigma/dx_{||}$ for different $x_{||}$ intervals as a function of the square of the c.m. energy, $s = W^2$. The sphericity axis was used as the jet axis.

42) The normalized differential cross section $1/\sigma_{tot}\ d\sigma/dx_T$, where x_T is the fractional transverse momentum $x_T = 2p_T/W$ at W = 14, 22, 34 and 41.5 GeV. The sphericity axis was used as the jet axis.

43) The normalized differential cross section for the rapidity $y = 1/2\ \ell n\ (E + P_{||})/(E - P_{||})$ folded around y = 0 for W = 14, 22 and 34 GeV. The thrust axis was used as the jet axis.

44) The height of the rapidity yield near y = 0 ($0.1 < y \leq 0.2$ ▲, $0.2 < y < 1$ ●) as a function of the c.m. energy W. Also shown are results from pp and $p\bar{p}$ interactions[41-43].

45) Same as data in Fig. 43 plotted as a function of $y - y_{max}$ at W = 14, 22 and 34 GeV.

46) The rapidity yield 1/NdN/dy normalized to the yield at $0.1 < y \leq 0.2$ for
a) W = 14, 22 and 34 GeV. The curves show the QCD string model predictions
b) W = 34 GeV. The dashed curve shows the prediction for $e^+e^- - q\bar{q}$. The solid curve shows the prediction of the QCD string model.

47 a) The average transverse momentum as a function of the rapidity at W = 14, 22 and 34 GeV using the thrust axis
b) Same as a) for the square of the transverse momentum.

48) The distribution of the angle α between the charged particle direction and the jet axis (= thrust axis) at W = 14, 22 and 34 GeV.

49) Same as Fig. 48 for $\cos\alpha$.

50) The distribution of α for different $p_{||}$ intervals at W = 14, 22 and 34 GeV. The curves show the prediction of the QCD independent jet model.

51) Same data as in Fig. 50 for cosα.

52) The distribution of α (in degrees) for different $x_{||}$ intervals at W = 14, 22 and 34 GeV.

53) Same as Fig. 52 for cosα.

54) The charged momentum flow around the jet axis

$$\frac{d\Phi_p}{d\alpha} = \frac{1}{N} \int \frac{p}{\Sigma p} \frac{d^2N}{dpd\alpha} dp$$

where Σp is the total charged momentum in an event, at W = 14, 22 and 34 GeV.

55) Selection of hard pp scattering events.

56) The average transverse momentum as a function of $x_{||} = 2p_{||}/W$ for the trigger side and the away side at W = 34 GeV. A particle with momentum greater than 4 GeV/c was required as the trigger (see text). The sphericity axis was determined separately for each side and was used as the jet axis.

57) The normalized differential cross section $1/\sigma_{tot}\ d\sigma/dx_{||}$ as a function of $x_{||}$ ar W = 34 GeV for the trigger and away side. The procedure was the same as for Fig. 56.

58) Same as Fig. 56 but with the direction of the trigger particle as the jet axis.

59) Same as Fig. 57 but with the direction of the trigger particle as the jet axis.

60) Same as Fig. 56 but with the direction of the trigger particle as the jet axis and defining $x_{||}$ as $x_{||}^t = p_{||}/p_{trigger}$.

61) Same as Fig. 57 but with the direction of the trigger particle as the jet axis and defining $x_{||}$ as $x_{||}^t = p_{||}/p_{trigger}$.

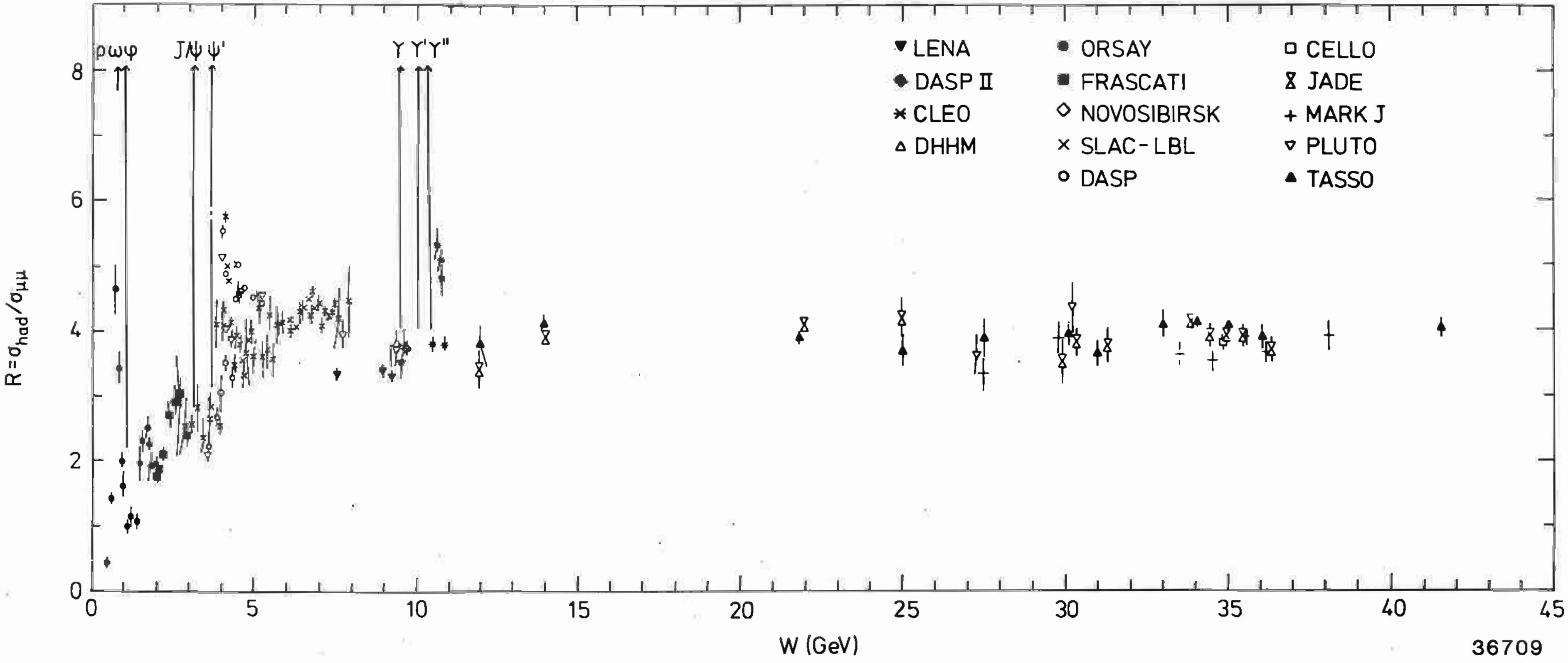
ρ ω φ
J/ψ ψ'
ϒ ϒ' ϒ''
▼ LENA
◆ DASP II
✱ CLEO
△ DHHM
● ORSAY
■ FRASCATI
◇ NOVOSIBIRSK
× SLAC-LBL
○ DASP
□ CELLO
⧗ JADE
+ MARK J
▽ PLUTO
▲ TASSO
R = σ_had/σ_μμ
0
2
4
6
8
0
5
10
15
20
25
30
35
40
45
W (GeV)
36709

Fig. 1

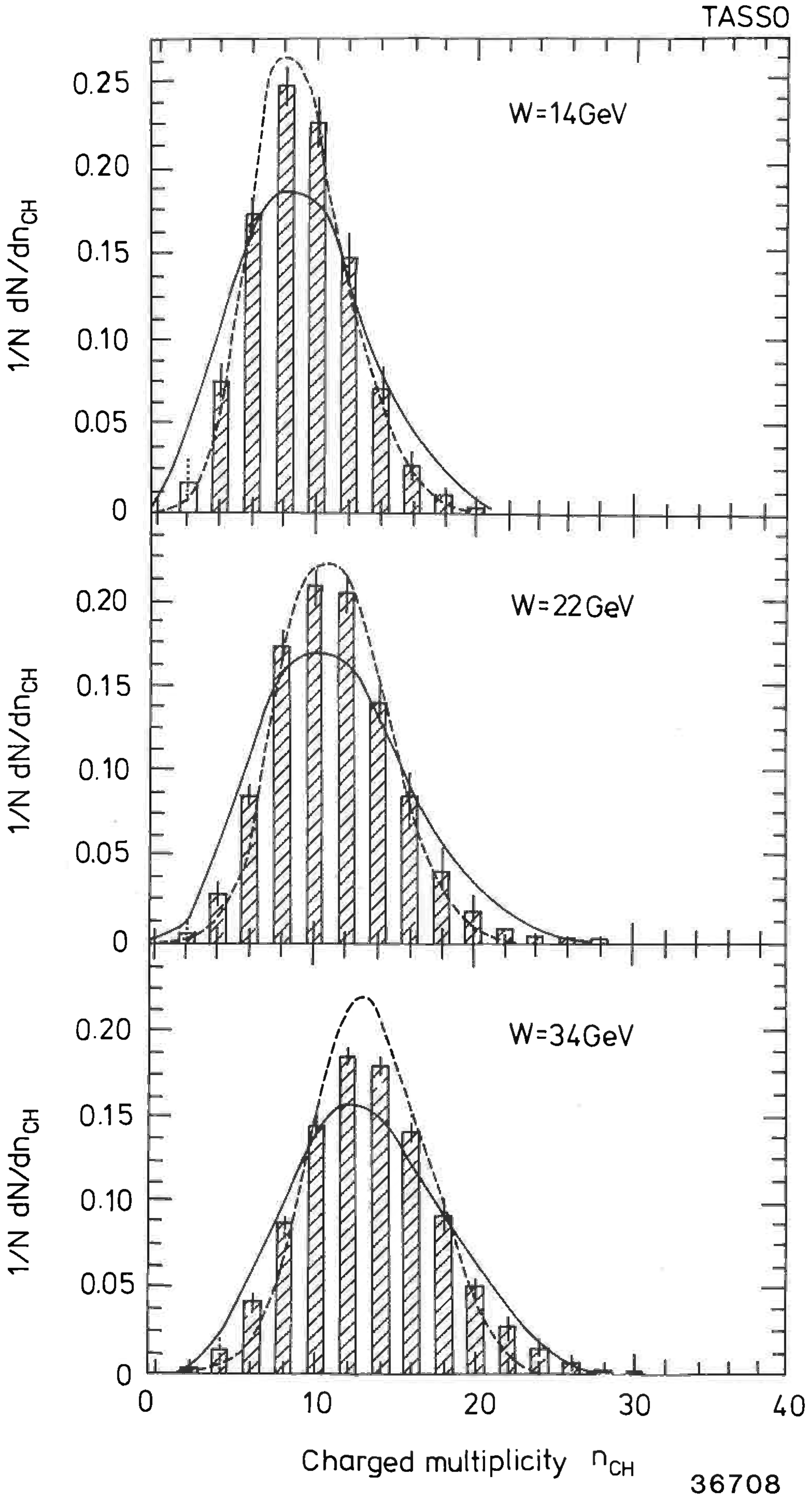
TASSO
W=14GeV
W=22GeV
W=34GeV
1/N dN/dn$_{CH}$
0.25
0.20
0.15
0.10
0.05
0
0
10
20
30
40
Charged multiplicity n$_{CH}$
36708

Fig. 2

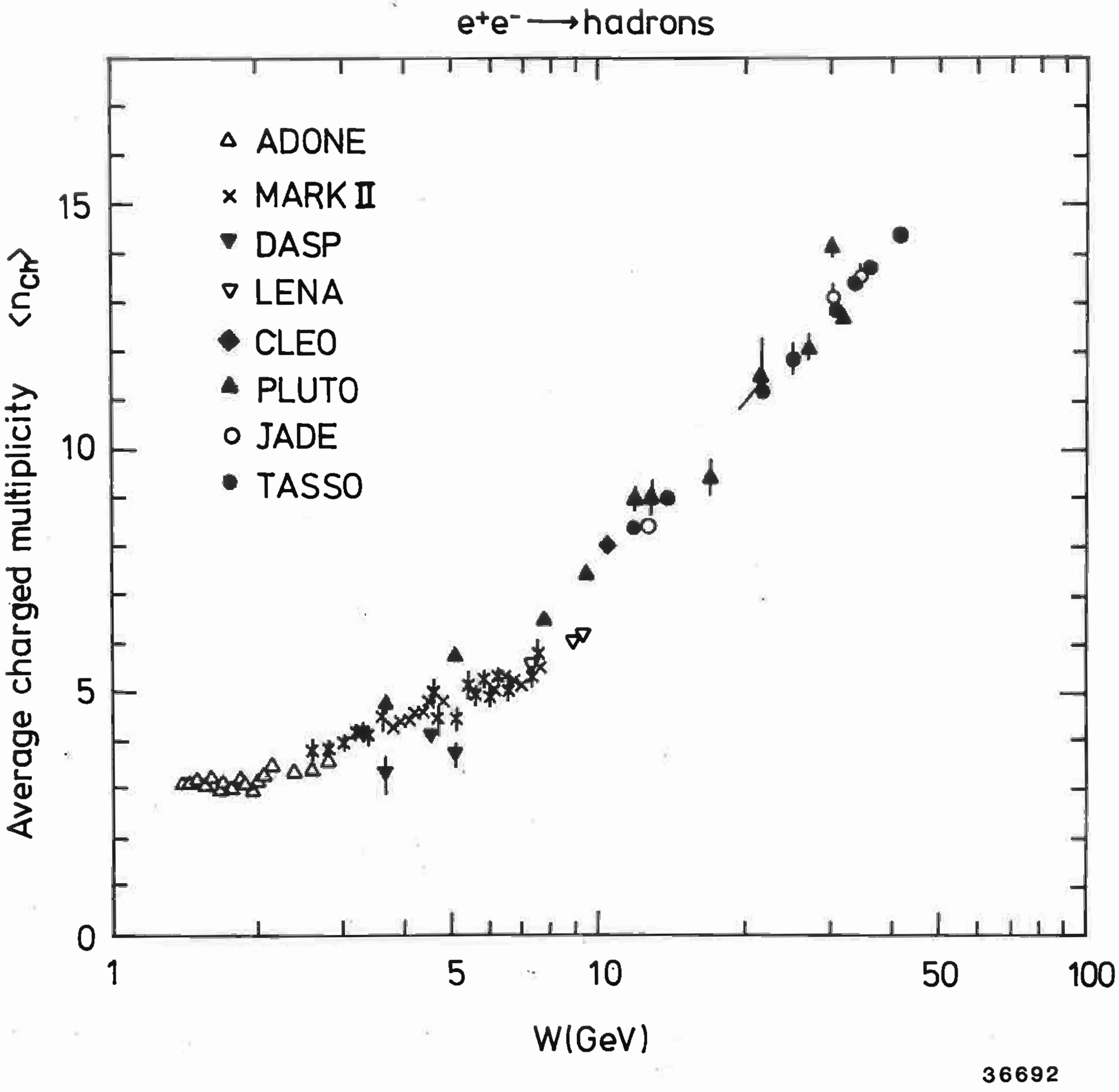
e⁺e⁻ ⟶ hadrons
△ ADONE
× MARK II
▼ DASP
▽ LENA
◆ CLEO
▲ PLUTO
○ JADE
● TASSO
Average charged multiplicity ⟨n_ch⟩
0
5
10
15
1
5
10
50
100
W(GeV)
36692

Fig. 3

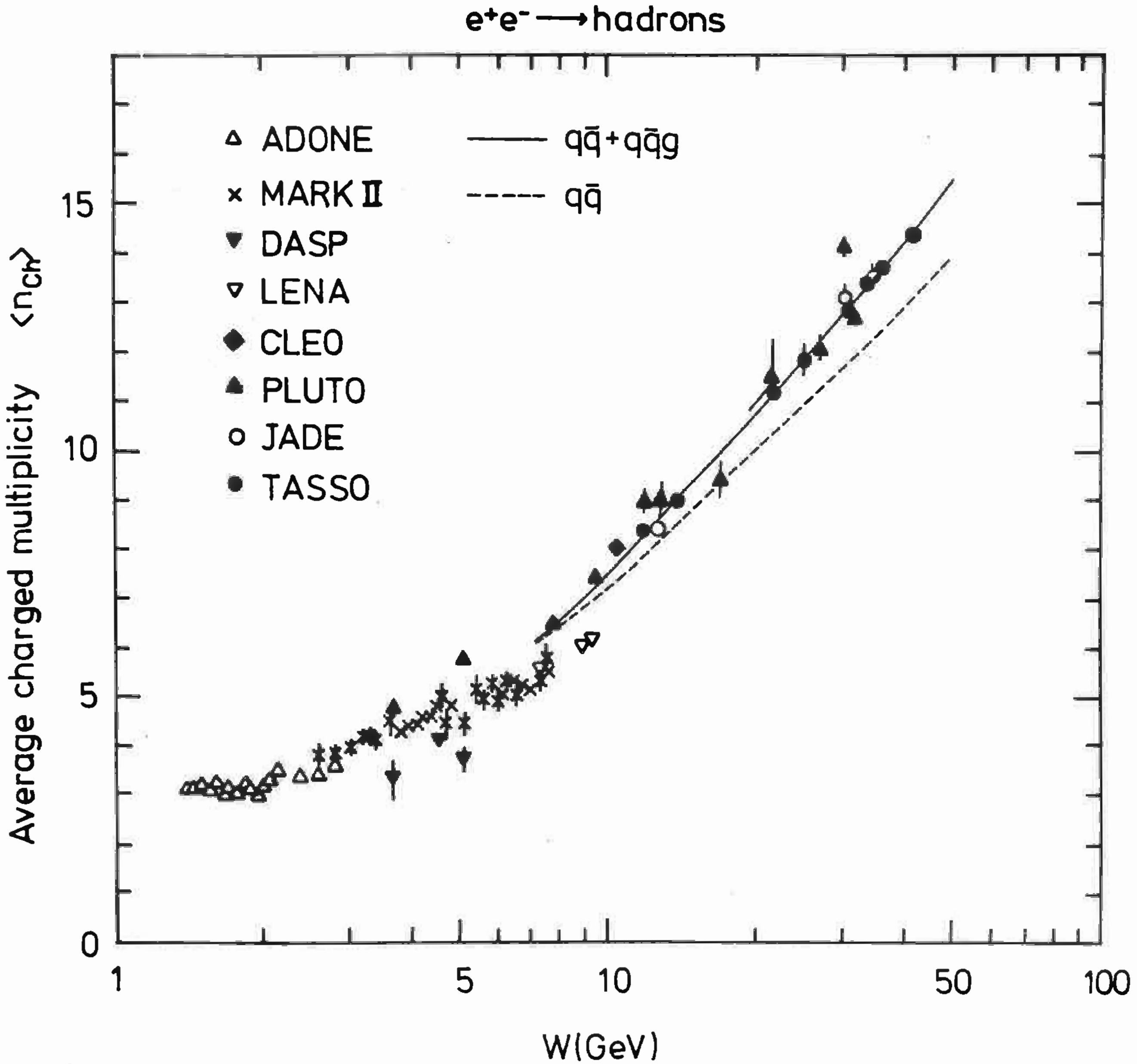

e⁺e⁻ ⟶ hadrons
Average charged multiplicity ⟨n_ch⟩
W(GeV)
0
5
10
15
1
5
10
50
100
ADONE
MARK II
DASP
LENA
CLEO
PLUTO
JADE
TASSO
qq̄ + qq̄g
qq̄

Fig. 4

36722

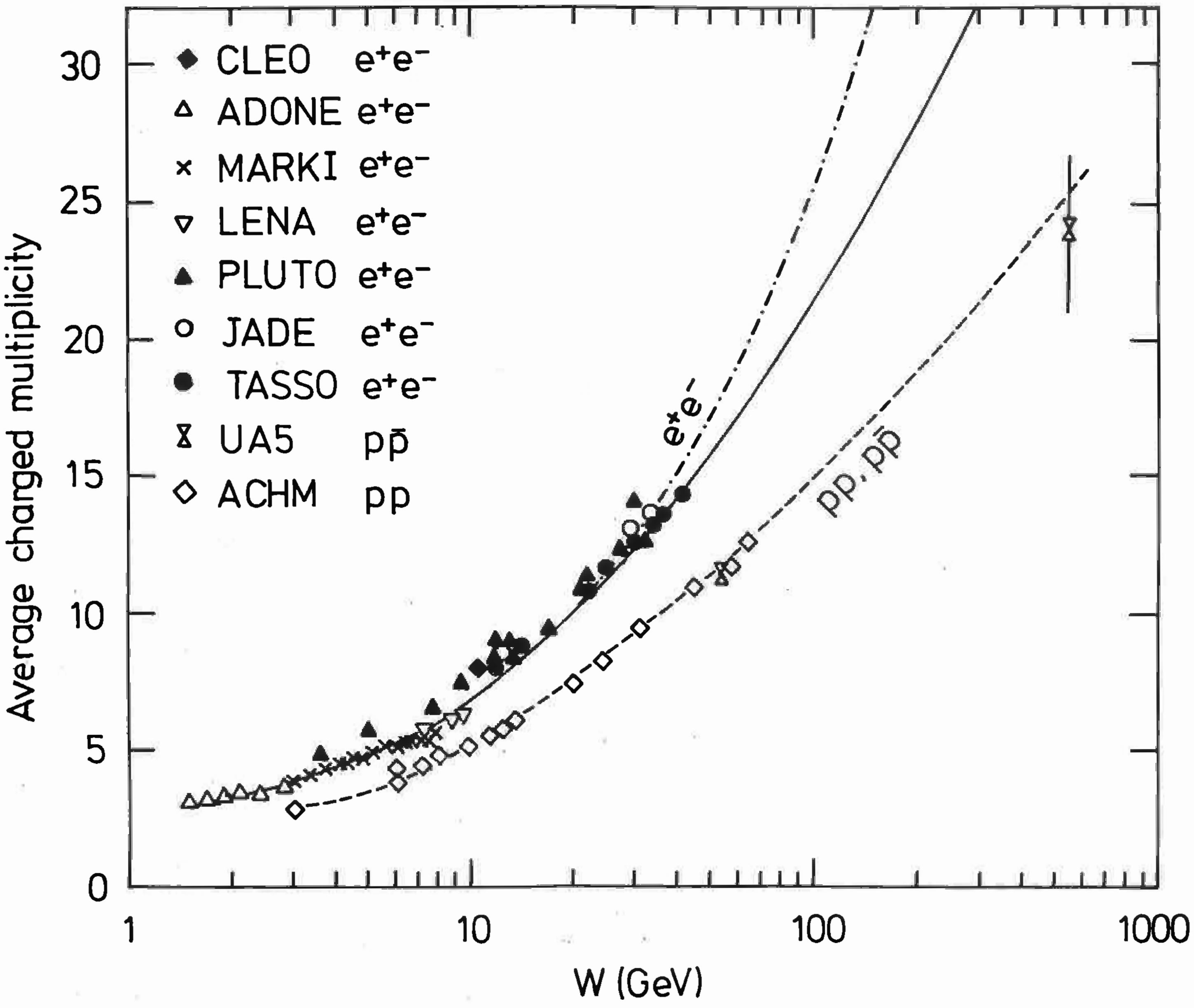
Average charged multiplicity
W (GeV)
0
5
10
15
20
25
30
1
10
100
1000
◆ CLEO e⁺e⁻
△ ADONE e⁺e⁻
× MARKI e⁺e⁻
▽ LENA e⁺e⁻
▲ PLUTO e⁺e⁻
○ JADE e⁺e⁻
● TASSO e⁺e⁻
UA5 pp̄
◇ ACHM pp
e⁺e⁻
pp, pp̄

36678

Fig. 5

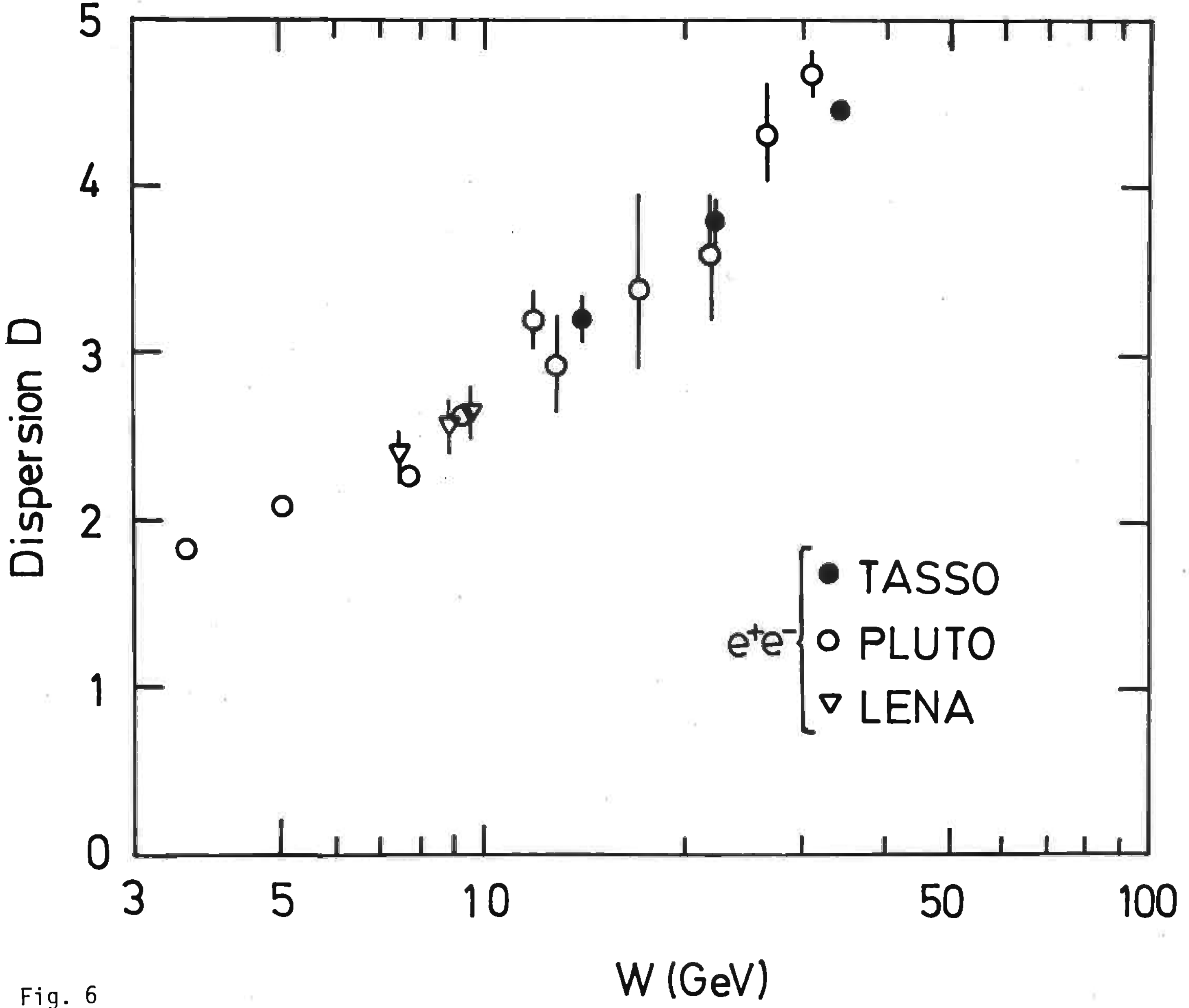

Fig. 6

36667

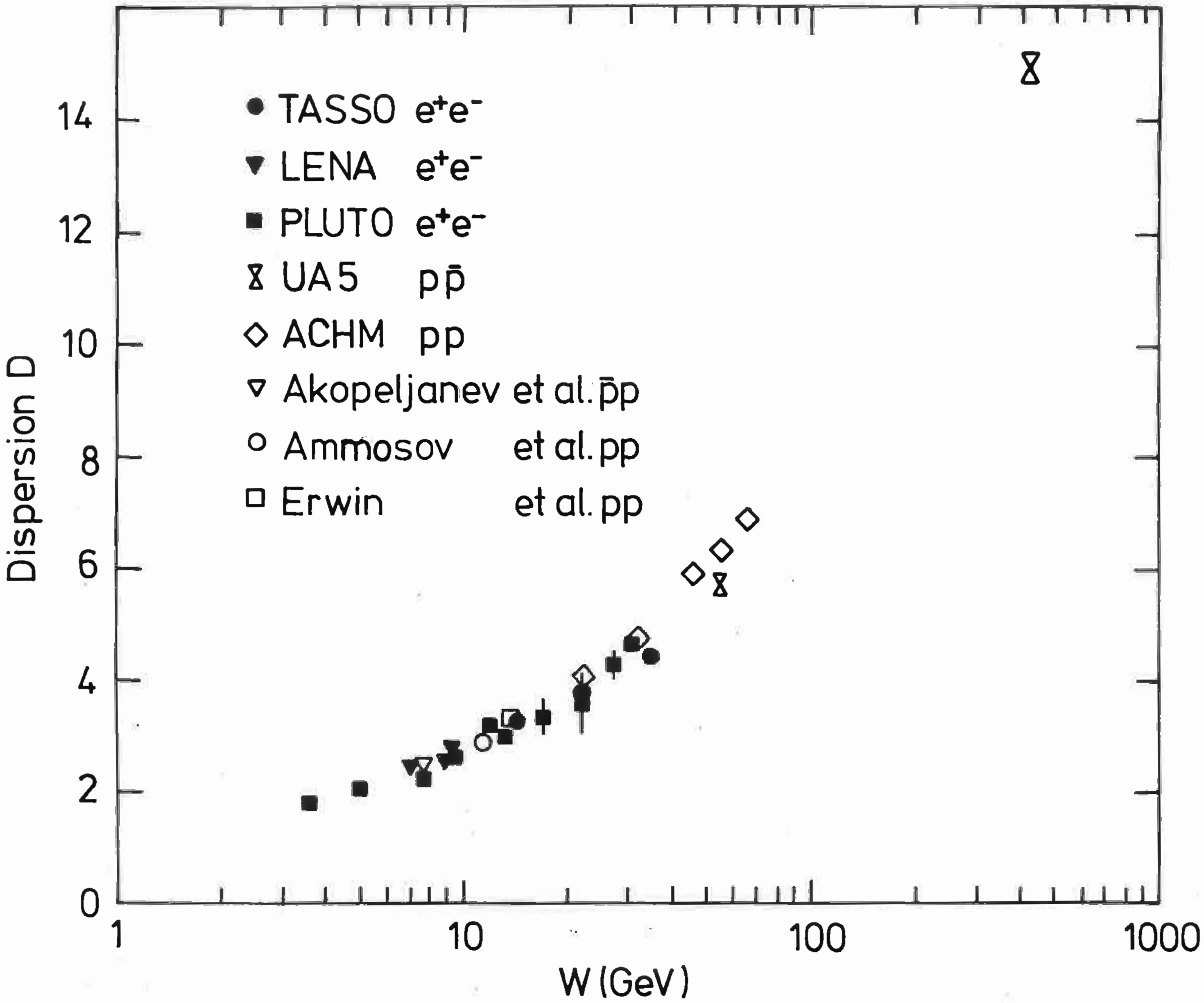

● TASSO e^+e^-
▼ LENA e^+e^-
■ PLUTO e^+e^-
UA5 $p\bar{p}$
◇ ACHM pp
▽ Akopeljanev et al. $\bar{p}p$
○ Ammosov et al. pp
□ Erwin et al. pp
Dispersion D
0
2
4
6
8
10
12
14
1
10
100
1000
W (GeV)

Fig. 7

36671

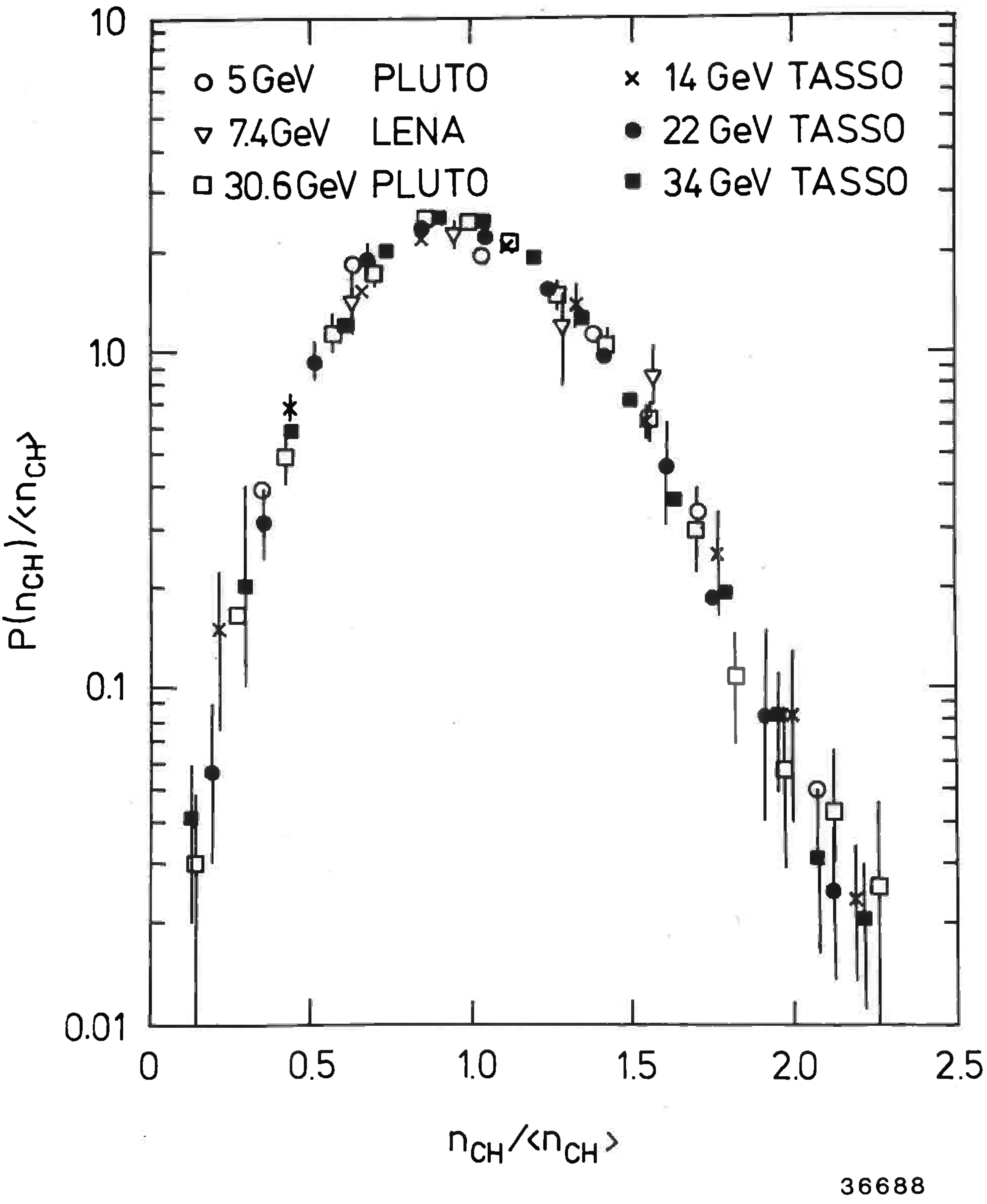

○ 5 GeV PLUTO
▽ 7.4 GeV LENA
□ 30.6 GeV PLUTO
× 14 GeV TASSO
● 22 GeV TASSO
■ 34 GeV TASSO
10
1.0
0.1
0.01
0
0.5
1.0
1.5
2.0
2.5
$P(n_{CH})/\langle n_{CH}\rangle$
$n_{CH}/\langle n_{CH}\rangle$
36688

Fig. 8a

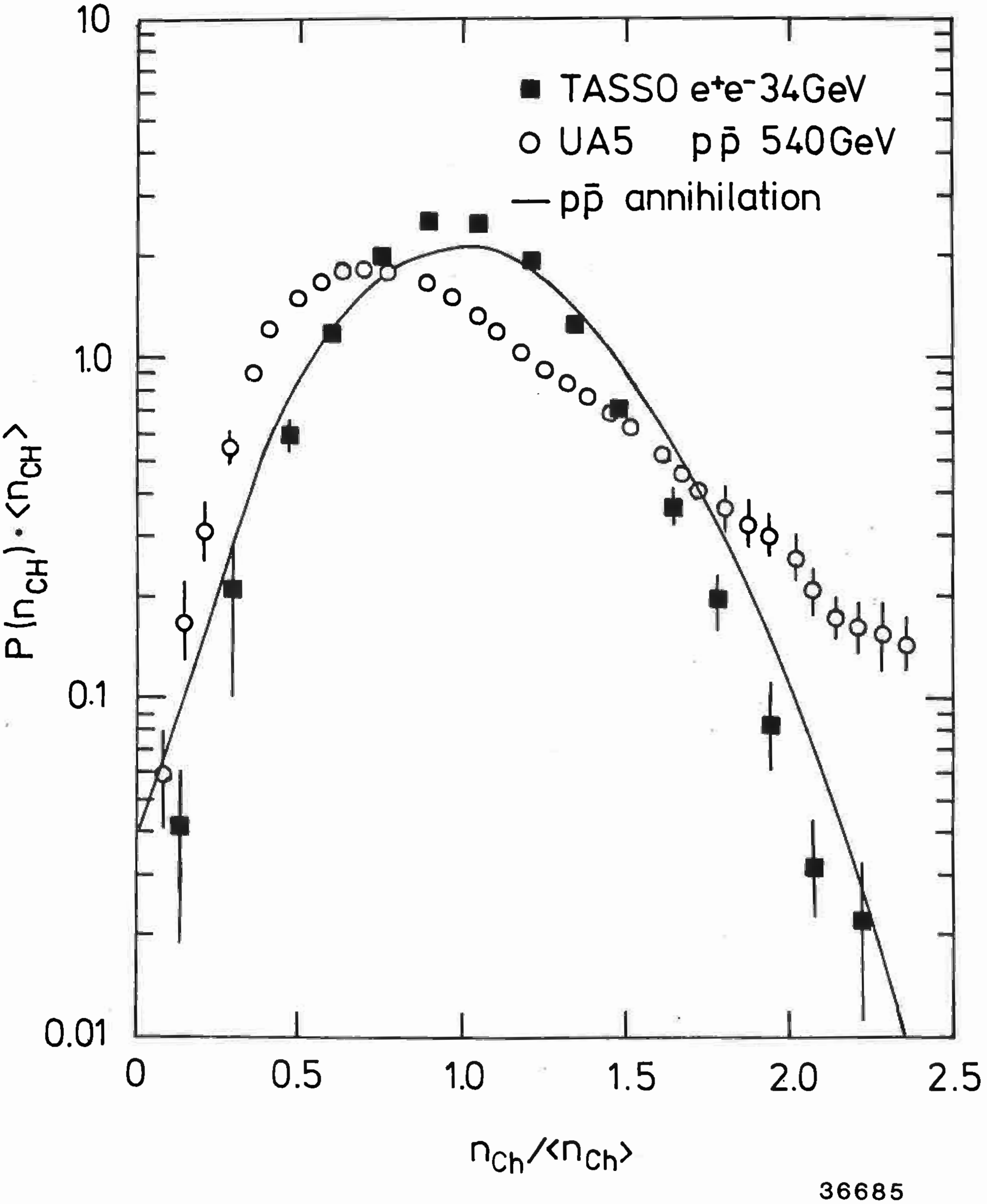
■ TASSO e⁺e⁻ 34GeV
○ UA5 p p̄ 540GeV
— p p̄ annihilation
10
1.0
0.1
0.01
0
0.5
1.0
1.5
2.0
2.5
P(n_CH) · ⟨n_CH⟩
n_Ch/⟨n_Ch⟩
36685

Fig. 8b

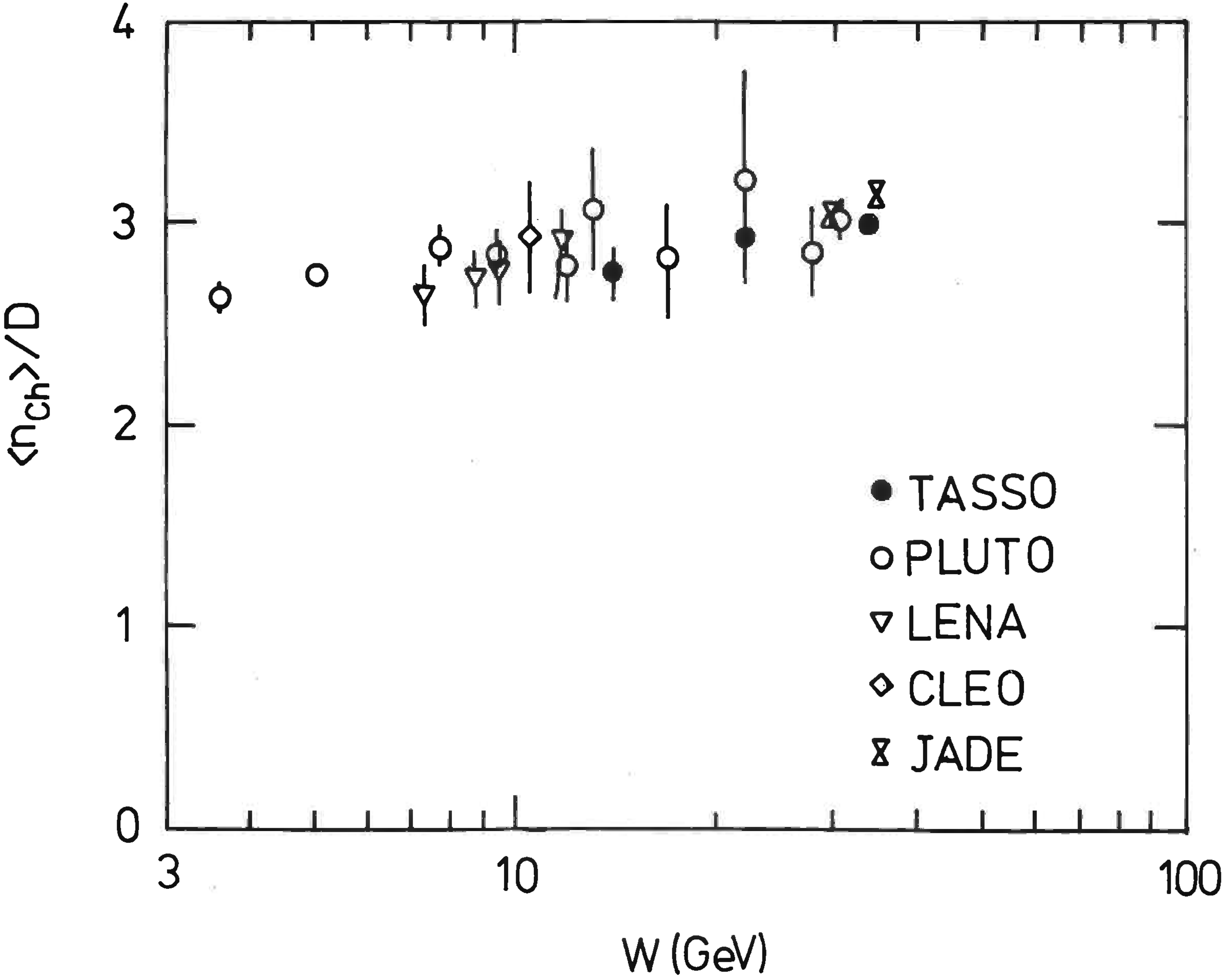

Fig. 9a

36666

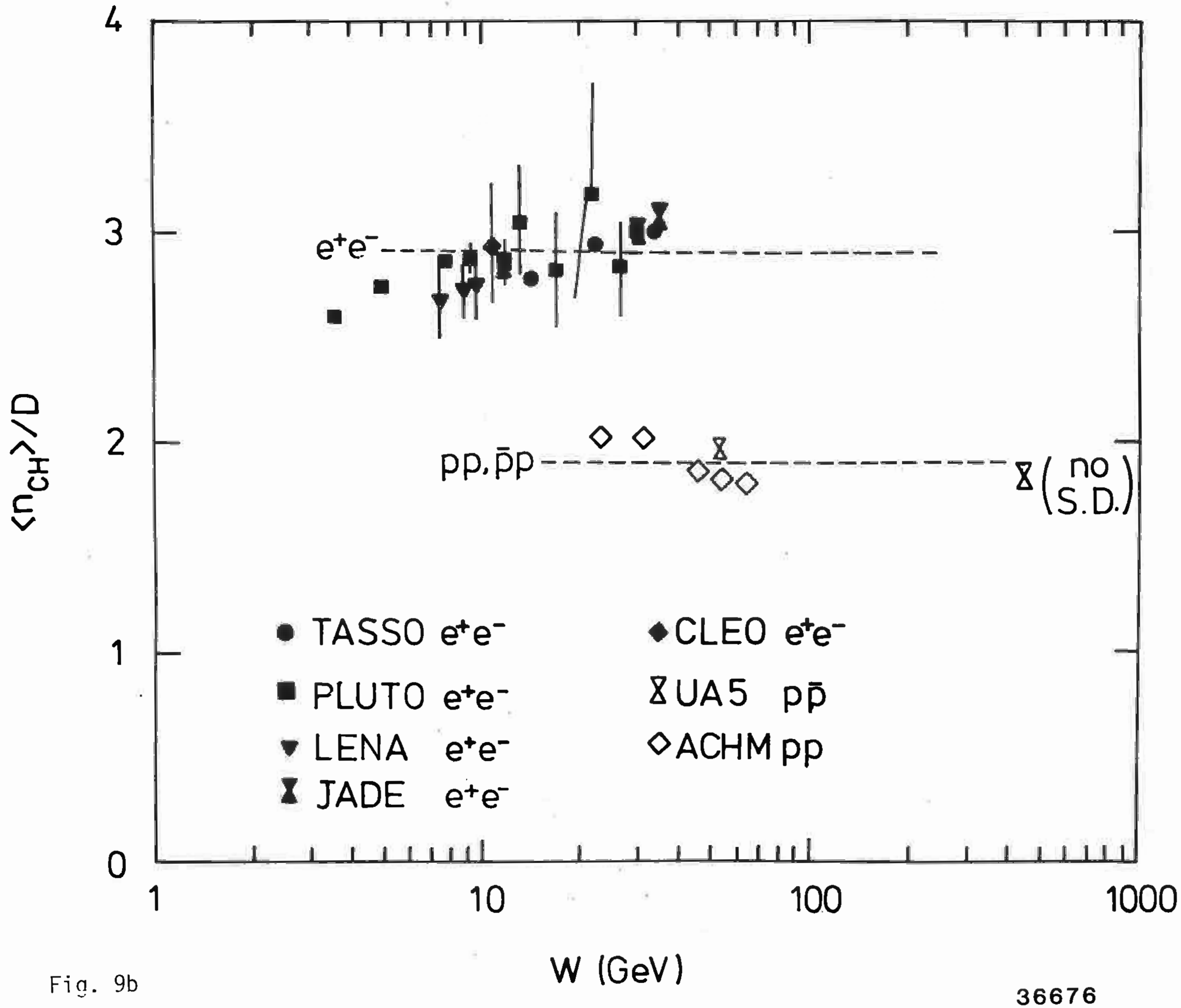
4
3
2
1
0
1
10
100
1000
W (GeV)
⟨n_CH⟩/D
e⁺e⁻
pp, p̄p
no S.D.
● TASSO e⁺e⁻
■ PLUTO e⁺e⁻
▼ LENA e⁺e⁻
JADE e⁺e⁻
◆ CLEO e⁺e⁻
UA5 pp̄
◇ ACHM pp

Fig. 9b

36676

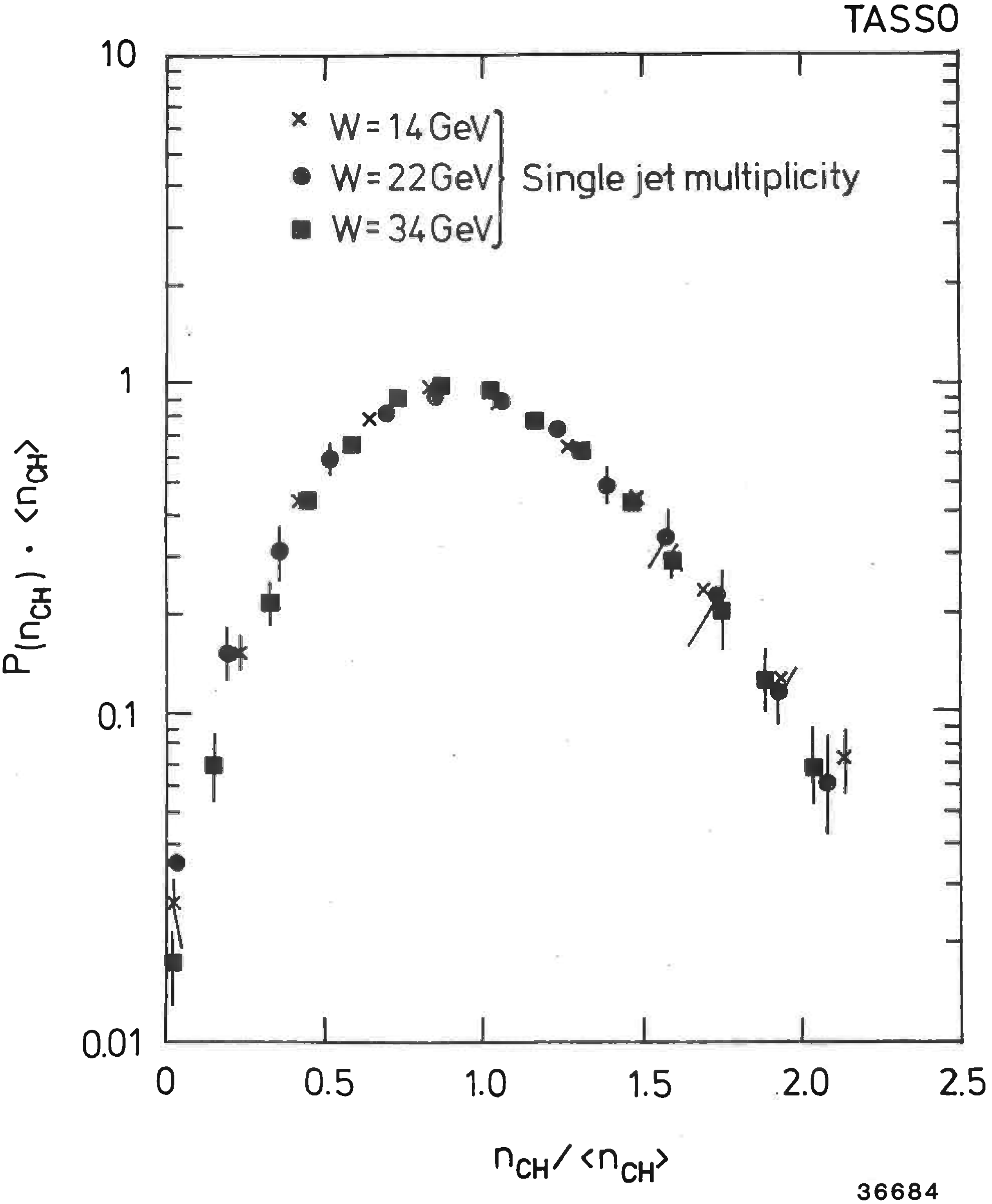
TASSO
× W = 14 GeV
● W = 22 GeV
■ W = 34 GeV
Single jet multiplicity
10
1
0.1
0.01
0
0.5
1.0
1.5
2.0
2.5
P(n_CH) · ⟨n_CH⟩
n_CH / ⟨n_CH⟩
36684

Fig. 10

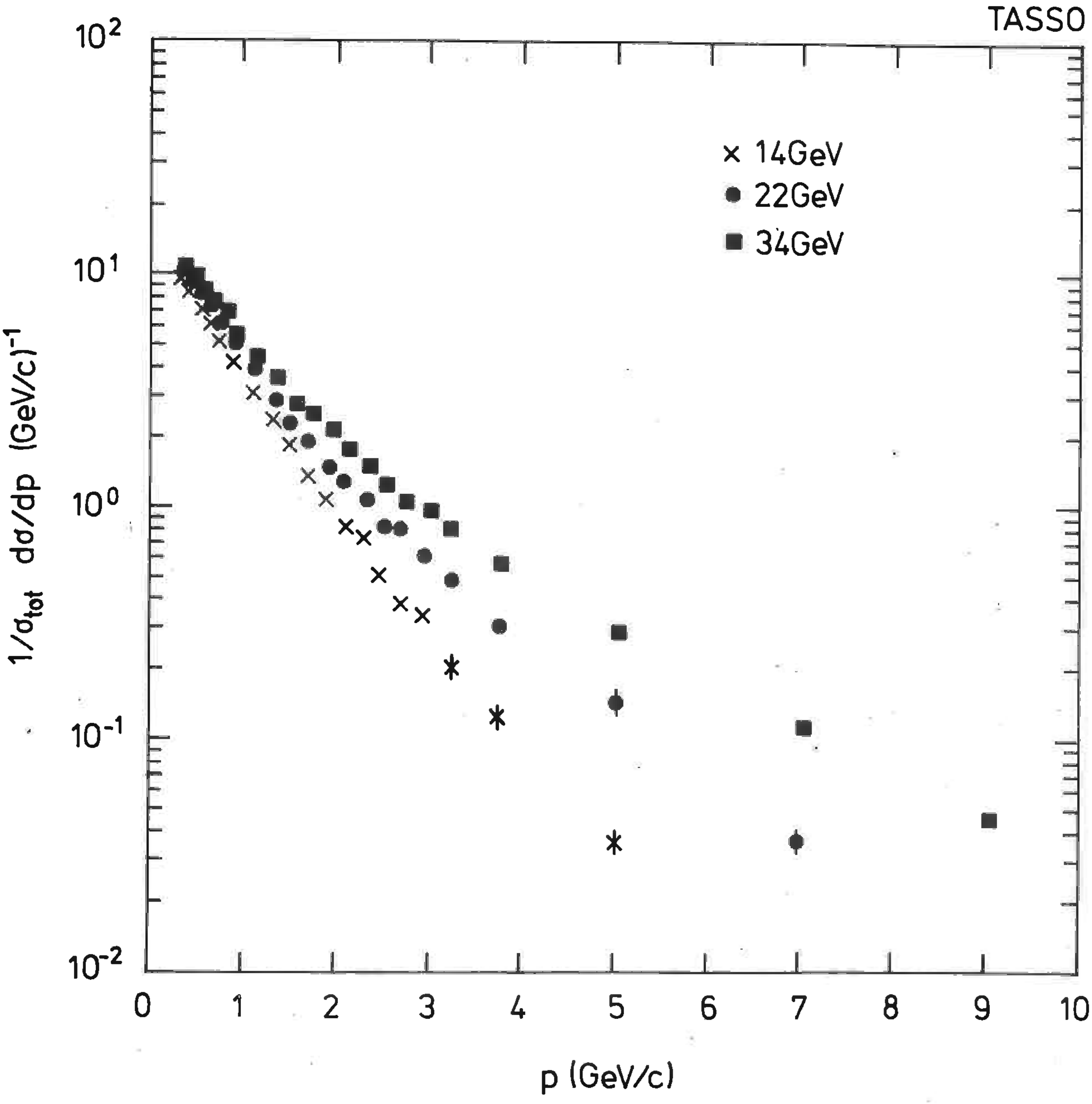
TASSO
× 14GeV
● 22GeV
■ 34GeV
10^2
10^1
10^0
10^{-1}
10^{-2}
$1/\sigma_{tot}\ d\sigma/dp\ (GeV/c)^{-1}$
0
1
2
3
4
5
6
7
8
9
10
p (GeV/c)
36693

Fig.11

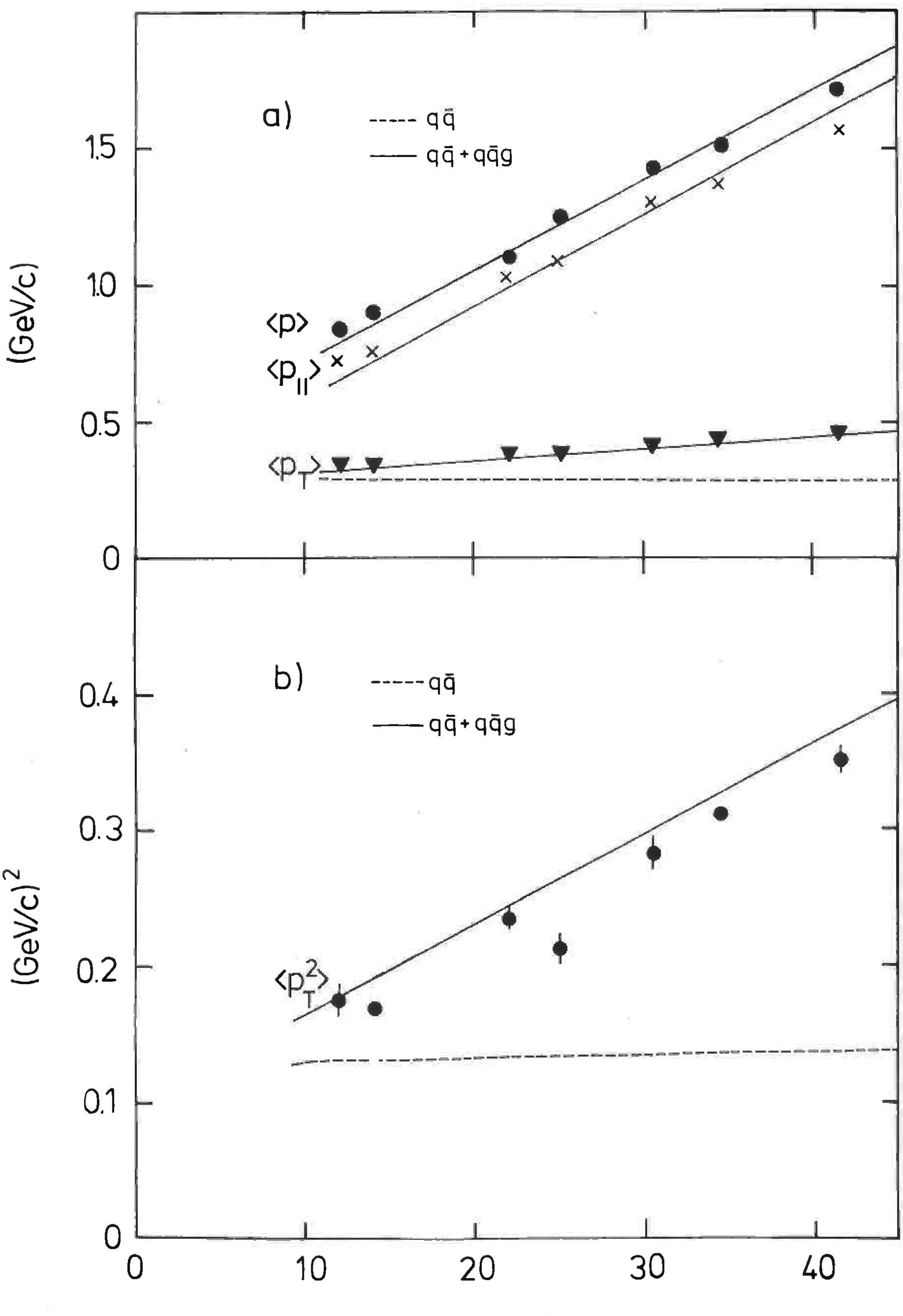
TASSO
a)
----- $q\bar{q}$
—— $q\bar{q}+q\bar{q}g$
$\langle p \rangle$
$\langle p_{\parallel} \rangle$
$\langle p_T \rangle$
(GeV/c)
1.5
1.0
0.5
0
b)
----- $q\bar{q}$
—— $q\bar{q}+q\bar{q}g$
$\langle p_T^2 \rangle$
$(\mathrm{GeV/c})^2$
0.4
0.3
0.2
0.1
0
0
10
20
30
40
W (GeV)
36719

Fig. 12

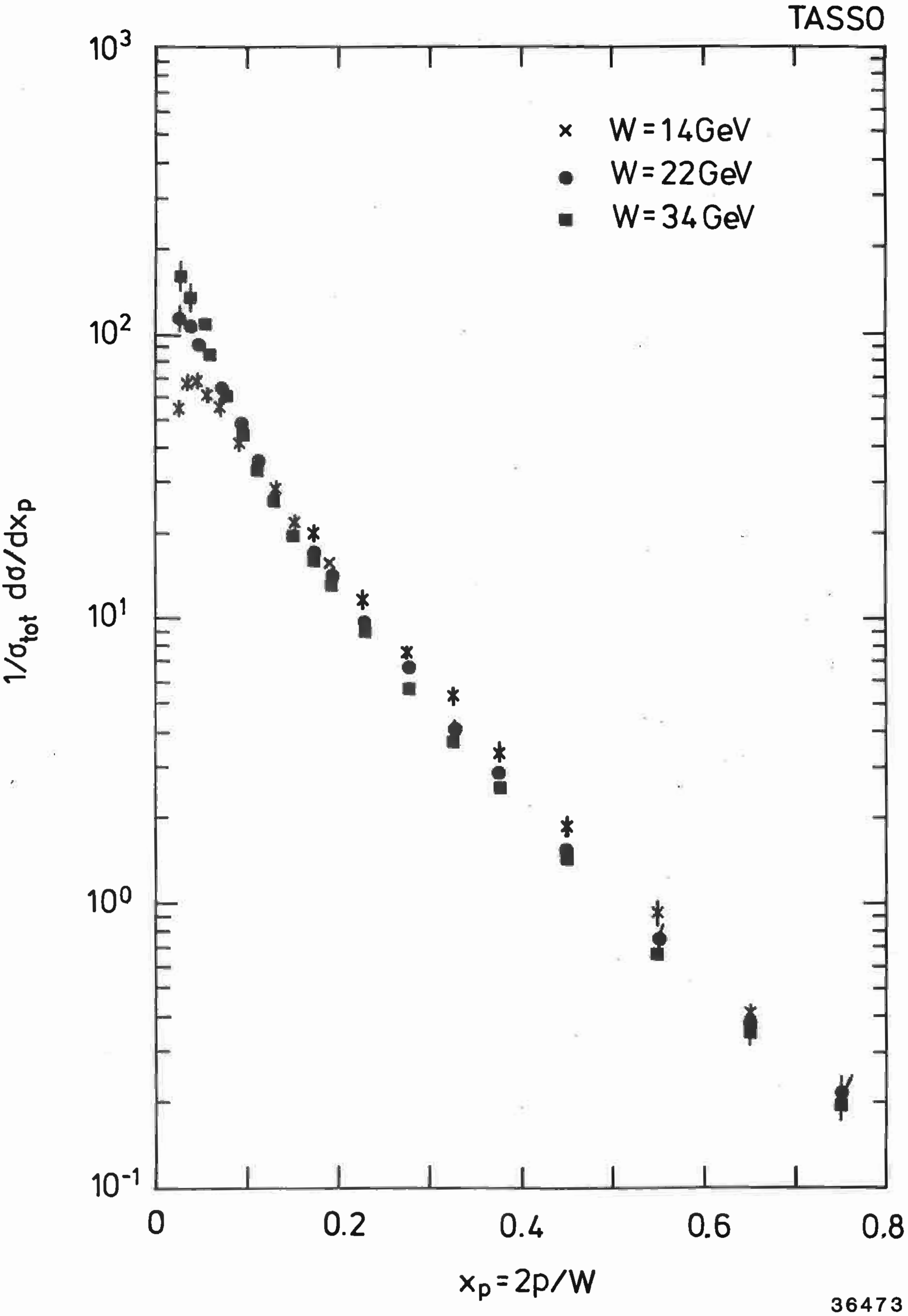
TASSO
× W = 14GeV
● W = 22GeV
■ W = 34GeV
10^3
10^2
10^1
10^0
10^{-1}
$1/\sigma_{tot}\ d\sigma/dx_p$
0
0.2
0.4
0.6
0.8
$x_p = 2p/W$
36473

Fig. 13

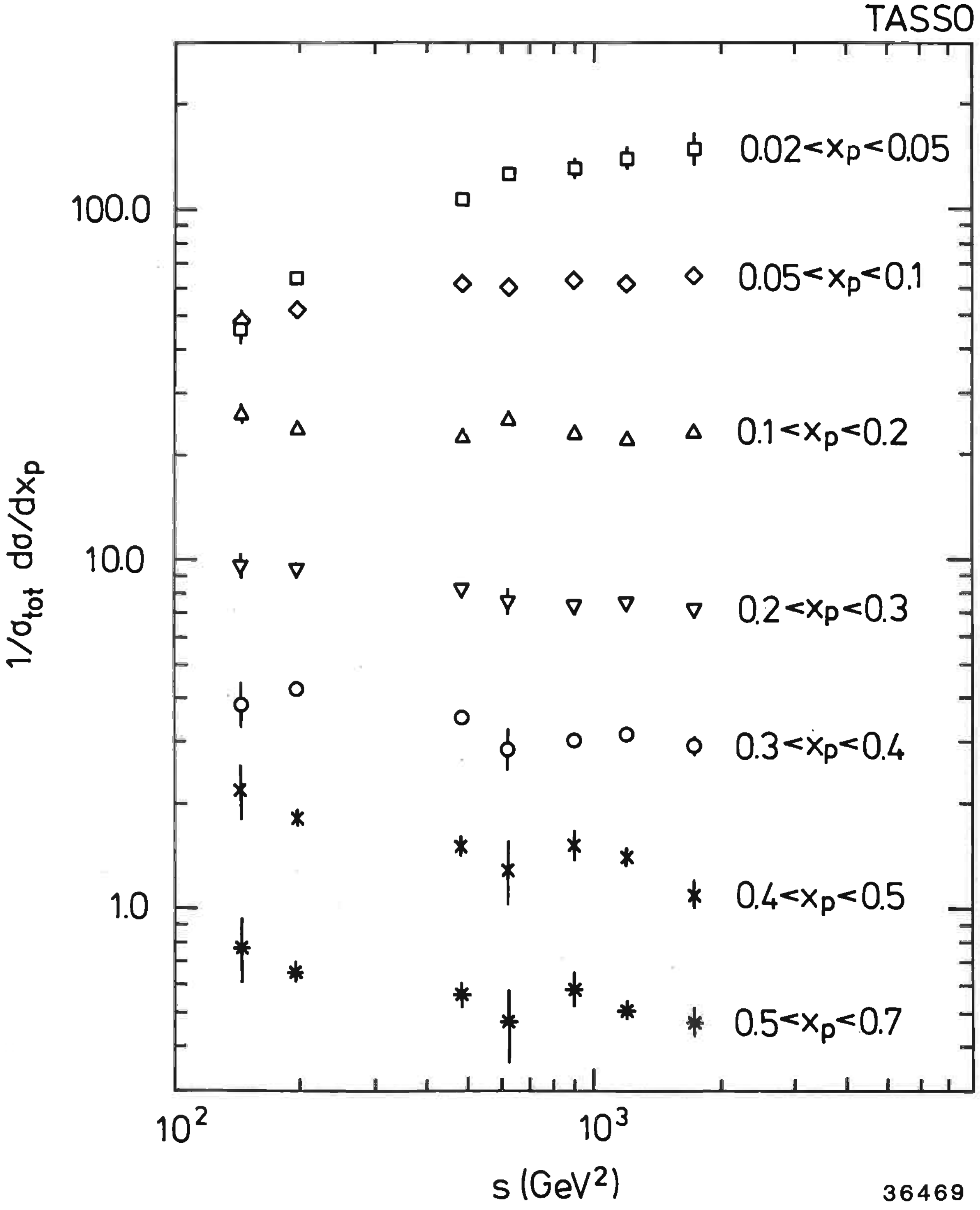
TASSO
100.0
10.0
1.0
$1/\sigma_{tot}\ d\sigma/dx_p$
10^2
10^3
s (GeV^2)
$0.02<x_p<0.05$
$0.05<x_p<0.1$
$0.1<x_p<0.2$
$0.2<x_p<0.3$
$0.3<x_p<0.4$
$0.4<x_p<0.5$
$0.5<x_p<0.7$
36469

Fig. 14

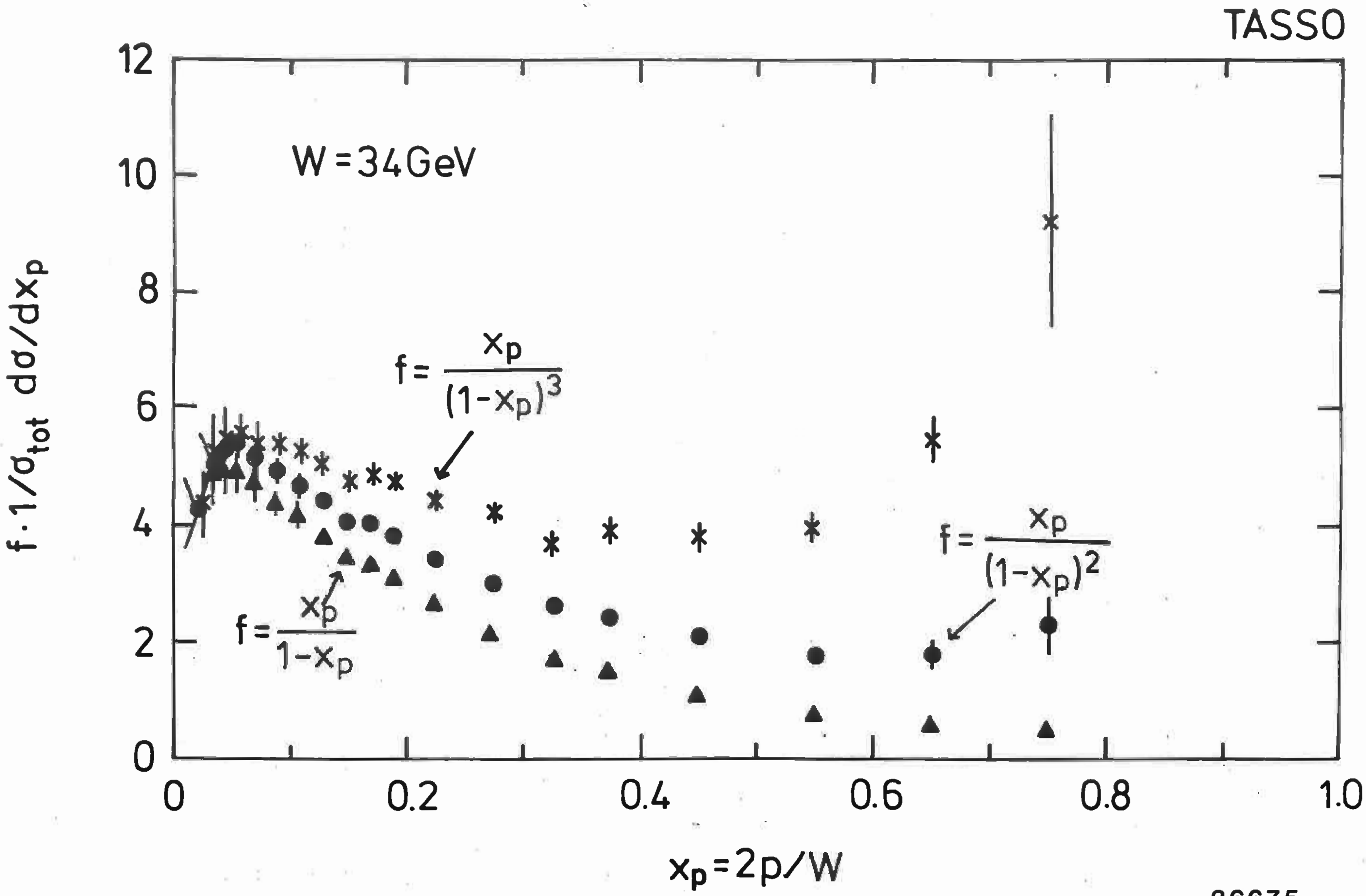
TASSO
W = 34 GeV
$f \cdot 1/\sigma_{tot}\ d\sigma/dx_p$
$x_p = 2p/W$
$f = \frac{x_p}{(1-x_p)^3}$
$f = \frac{x_p}{(1-x_p)^2}$
$f = \frac{x_p}{1-x_p}$
0
2
4
6
8
10
12
0
0.2
0.4
0.6
0.8
1.0

36675

Fig. 15

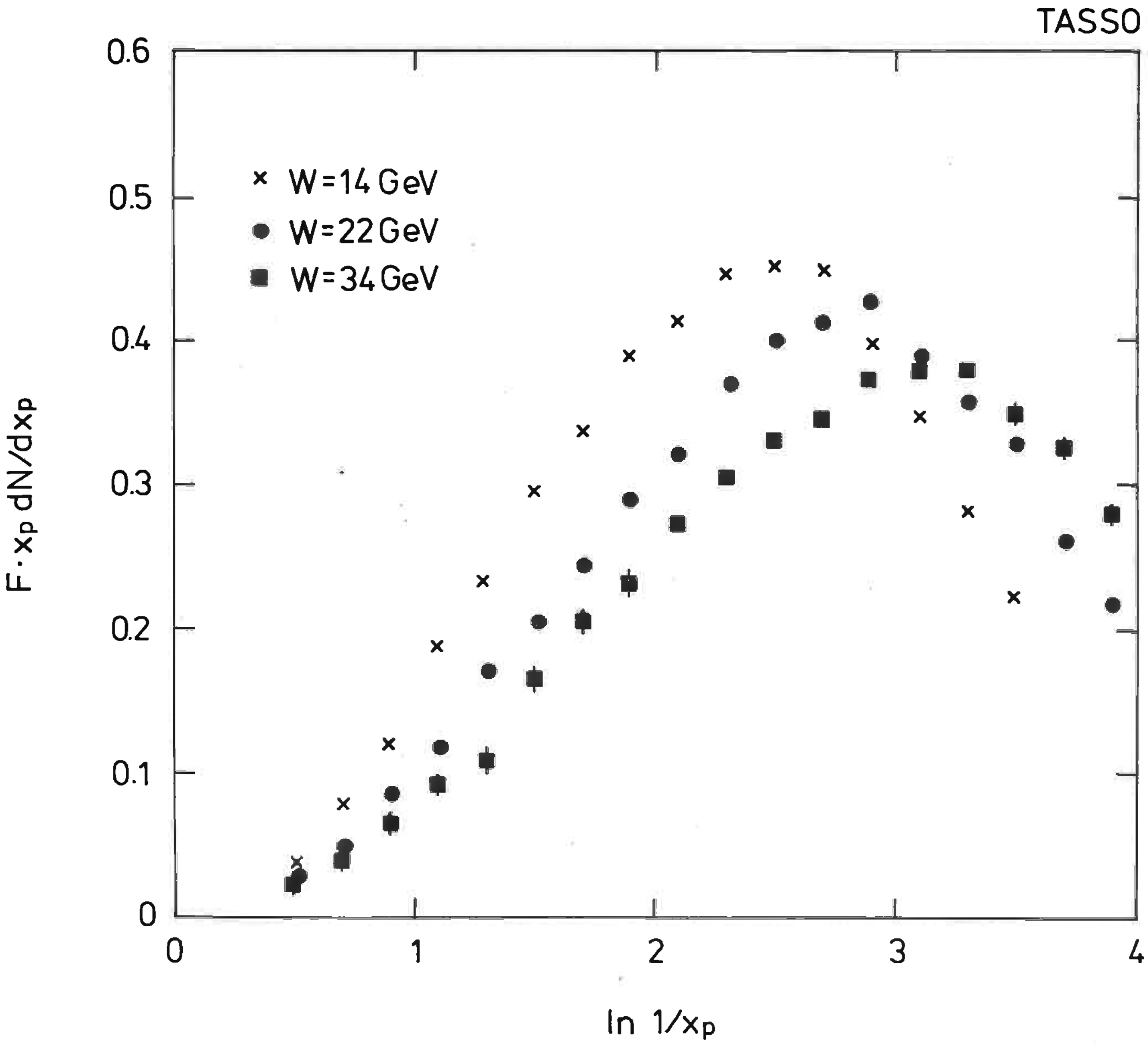

Fig. 16a

36690

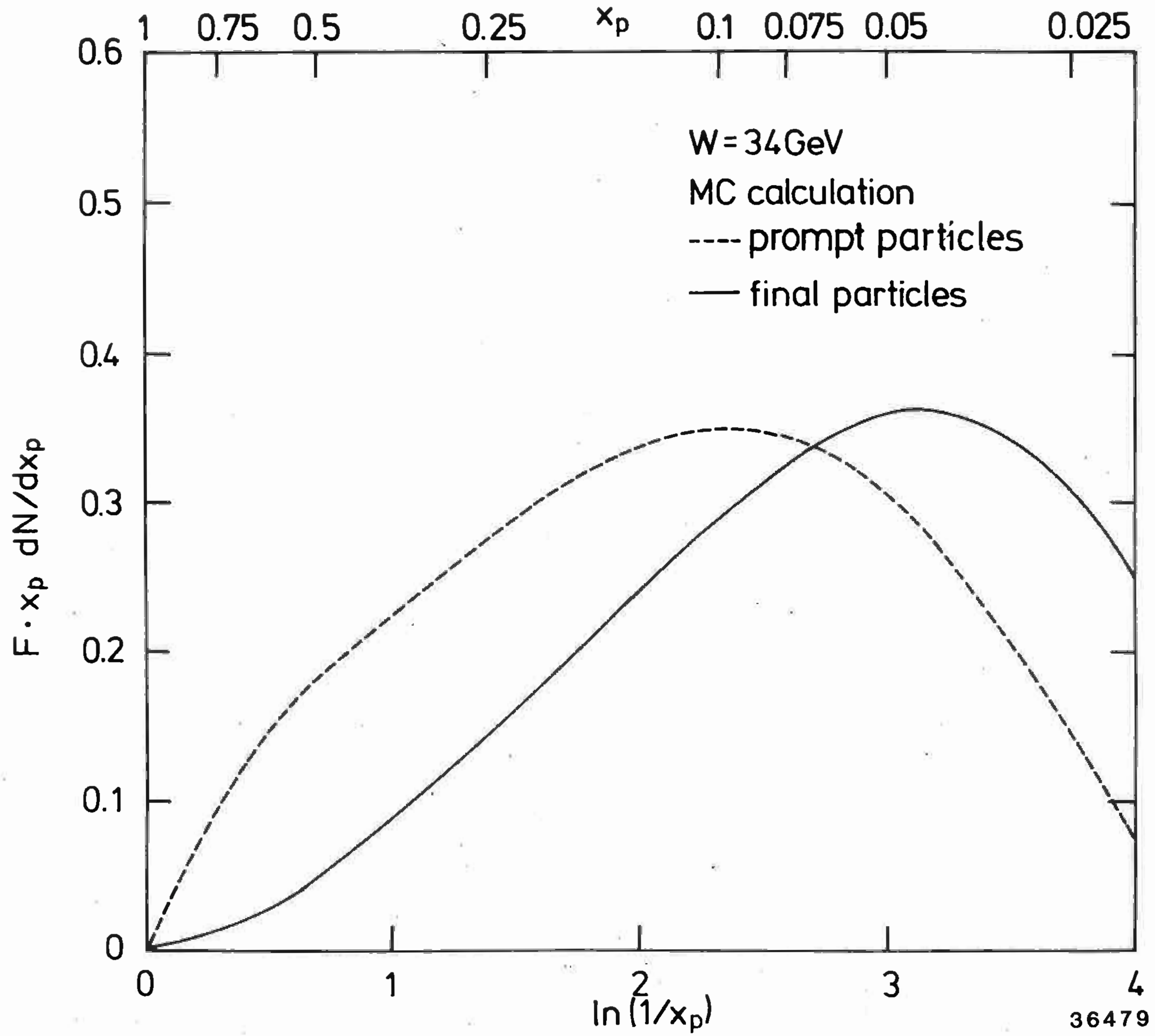
x_p
1
0.75
0.5
0.25
0.1
0.075
0.05
0.025
0.6
0.5
0.4
0.3
0.2
0.1
0
W = 34GeV
MC calculation
---- prompt particles
—— final particles
$F \cdot x_p \, dN/dx_p$
0
1
2
3
4
$\ln(1/x_p)$
36479

Fig. 16b

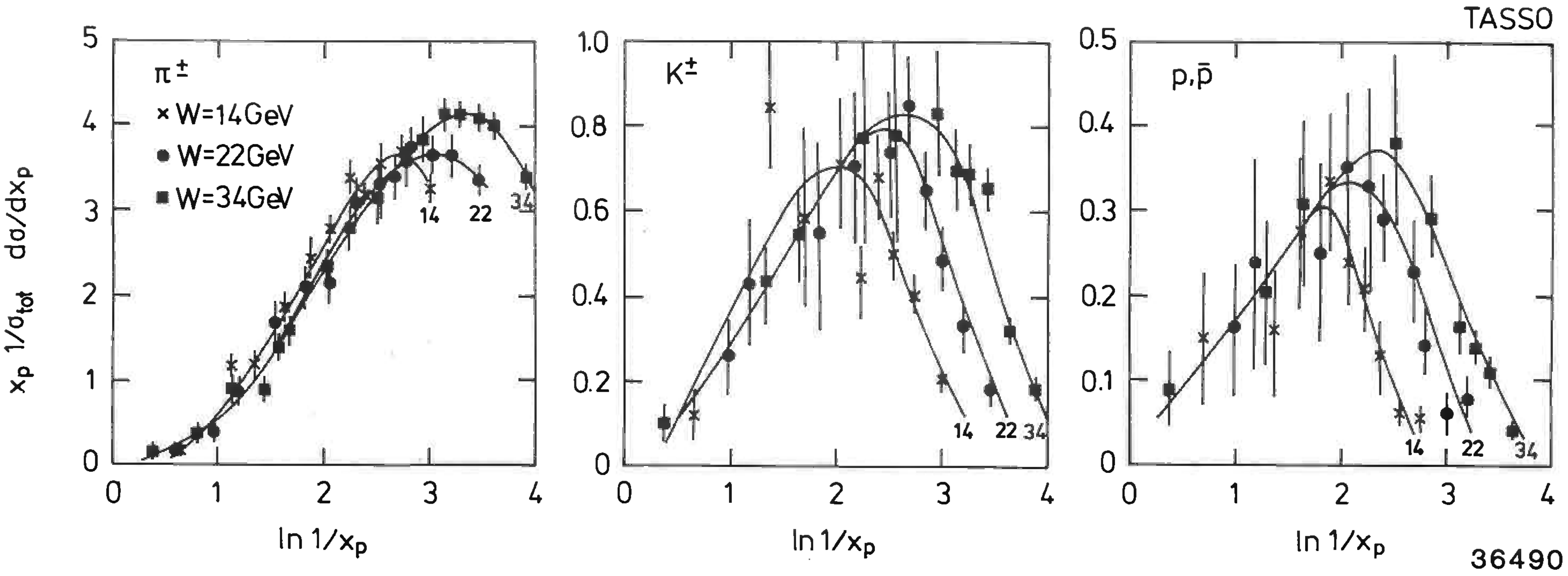
TASSO
π±
× W=14GeV
● W=22GeV
■ W=34GeV
K±
p,p̄
$x_p \; 1/\sigma_{tot} \; d\sigma/dx_p$
ln 1/x_p
14
22
34
0
1
2
3
4
5
0.2
0.4
0.6
0.8
1.0
0.1
0.3
0.5
36490

Fig. 17a

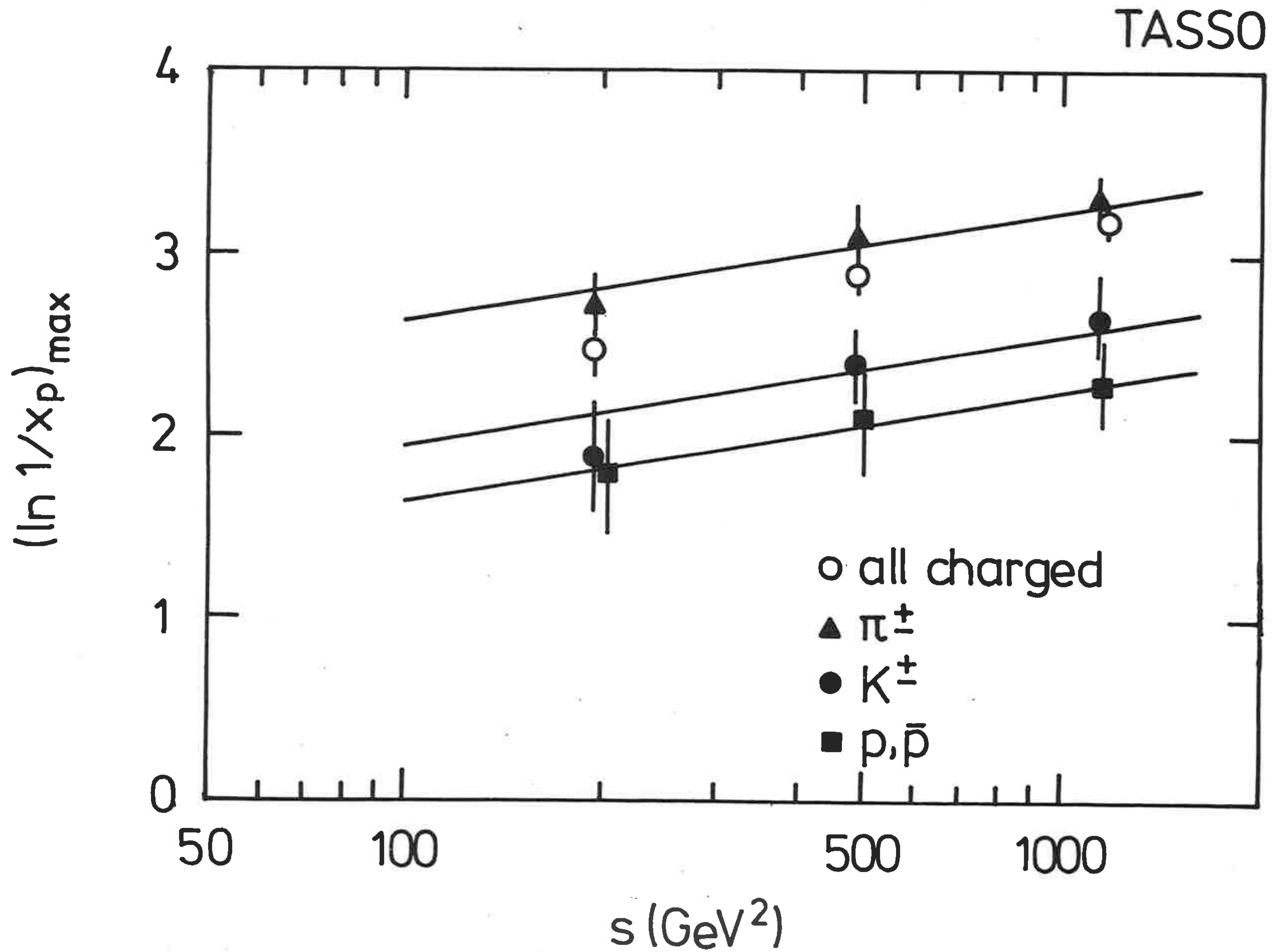

Fig. 17b

36665

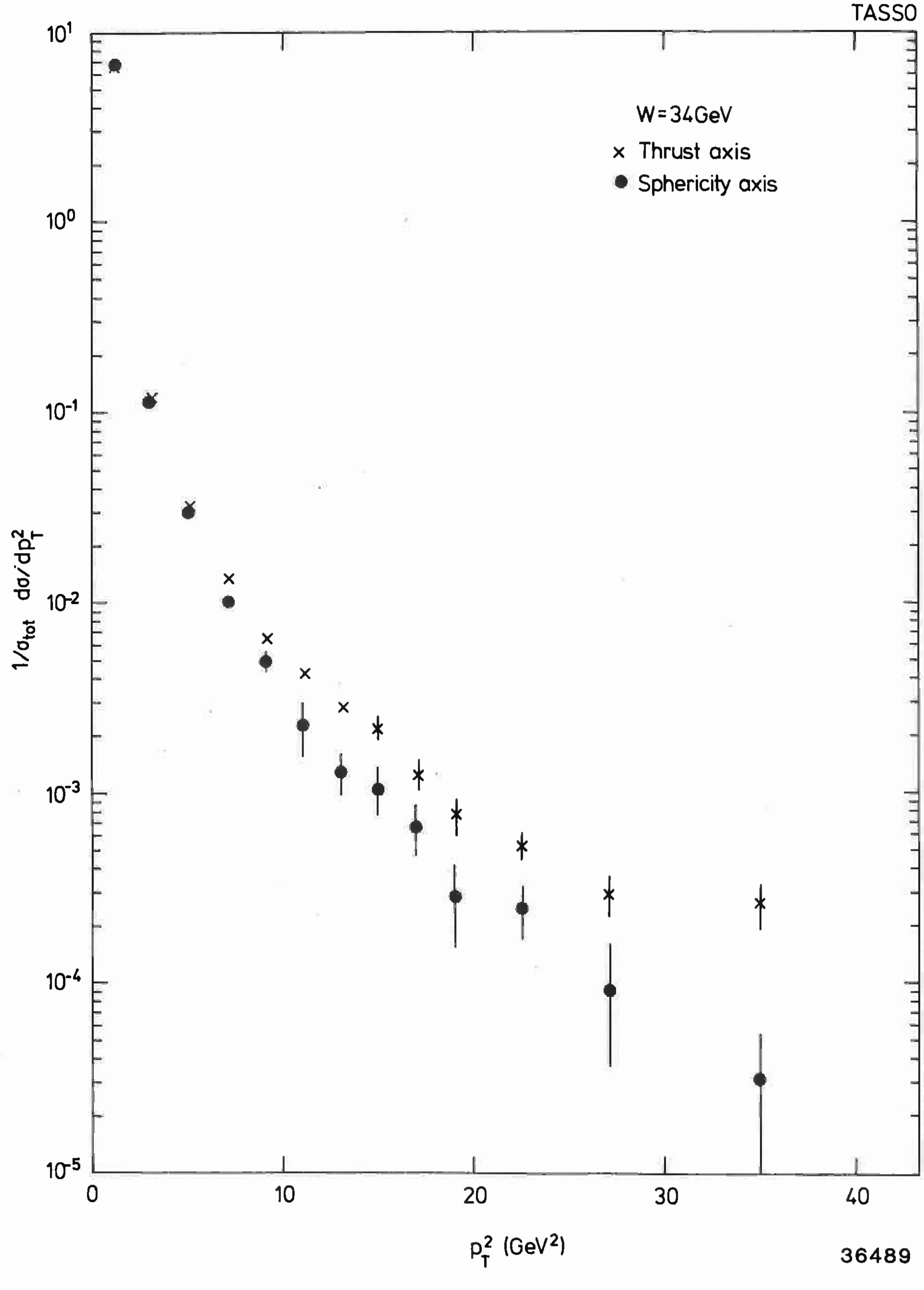TASSO
W=34GeV
× Thrust axis
● Sphericity axis
10^1
10^0
10^{-1}
10^{-2}
10^{-3}
10^{-4}
10^{-5}
$1/\sigma_{tot}\ d\sigma/dp_T^2$
0
10
20
30
40
p_T^2 (GeV^2)
36489

Fig. 18

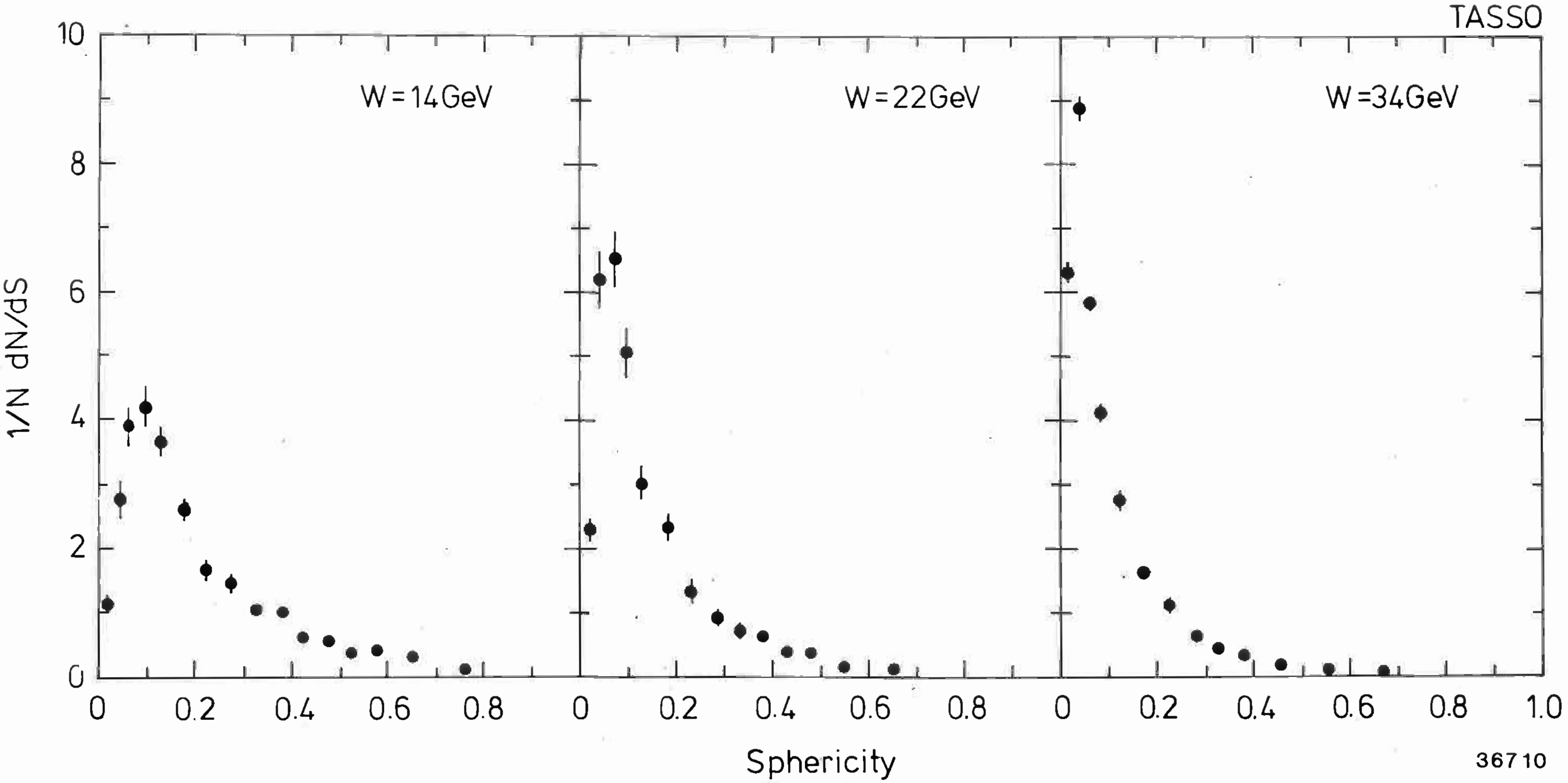
TASSO
10
8
6
4
2
0
1/N dN/dS
W = 14GeV
W = 22GeV
W = 34GeV
0
0.2
0.4
0.6
0.8
1.0
Sphericity
36710

Fig. 19

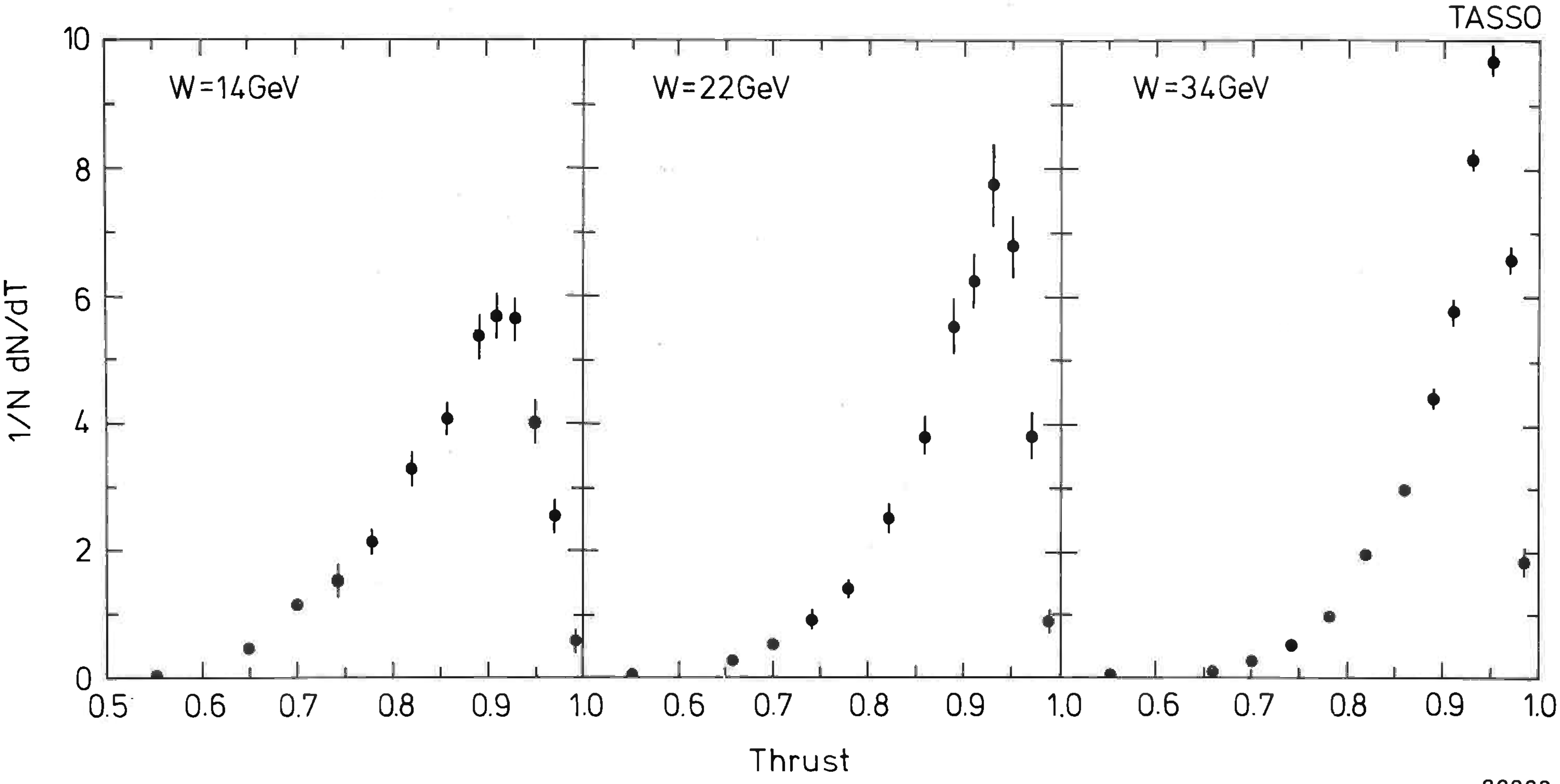
TASSO
W=14GeV
W=22GeV
W=34GeV
1/N dN/dT
10
8
6
4
2
0
0.5
0.6
0.7
0.8
0.9
1.0
Thrust
36368

Fig. 20

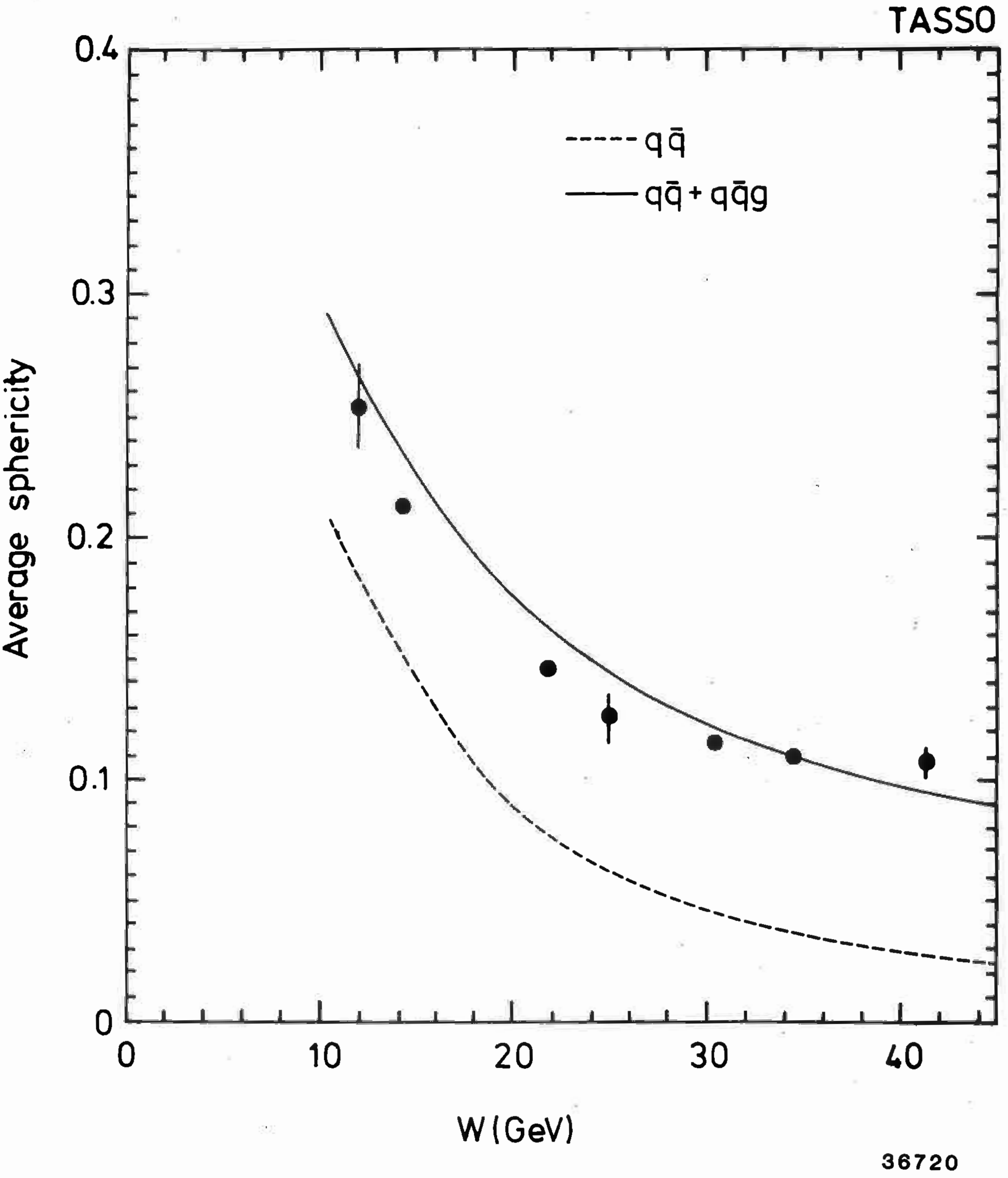
TASSO
Average sphericity
W (GeV)
----- $q\bar{q}$
—— $q\bar{q} + q\bar{q}g$
0
0.1
0.2
0.3
0.4
0
10
20
30
40
36720

Fig. 21

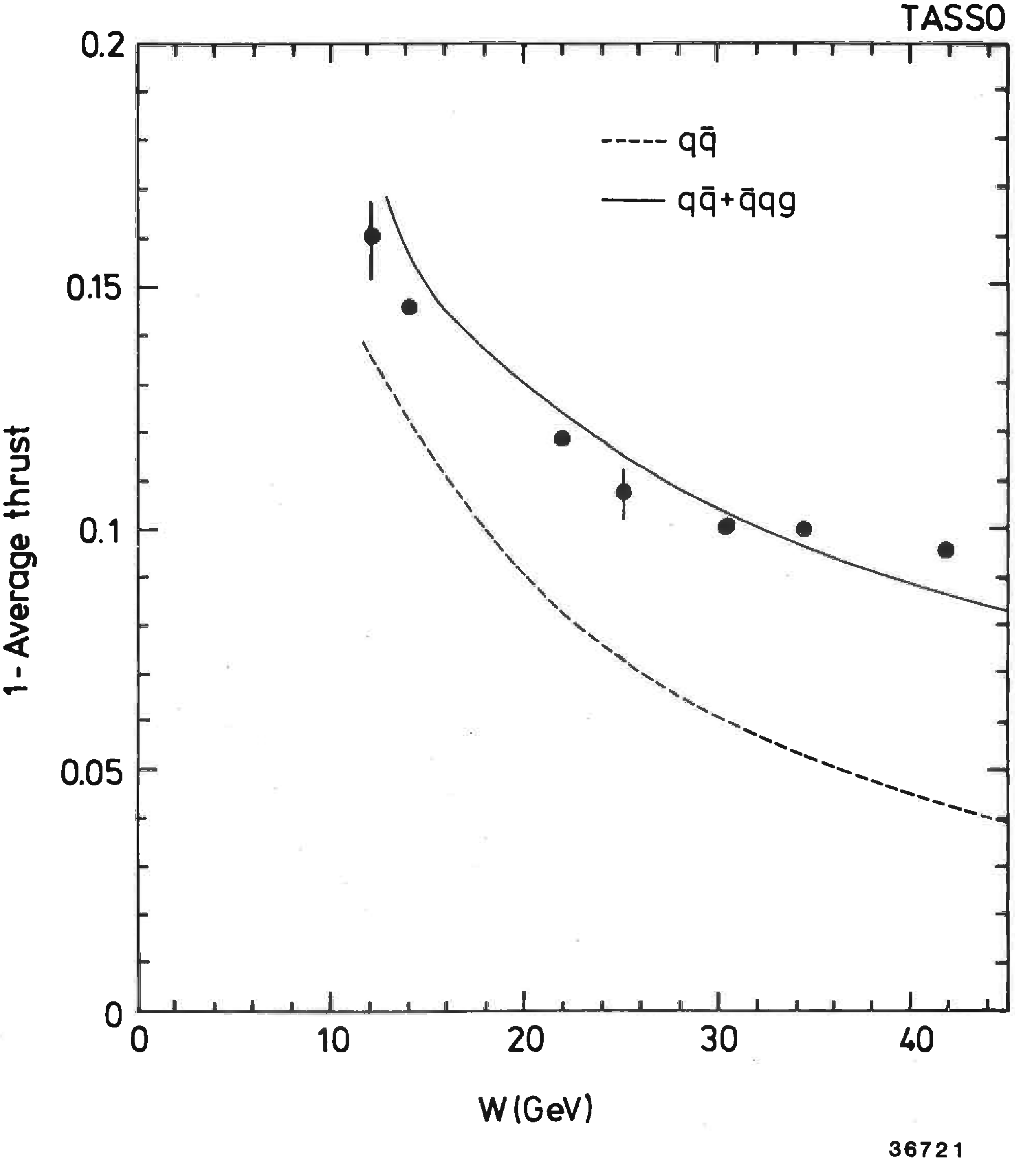
TASSO
0.2
0.15
0.1
0.05
0
1- Average thrust
----- $q\bar{q}$
—— $q\bar{q}+\bar{q}qg$
0
10
20
30
40
W (GeV)
36721

Fig. 22

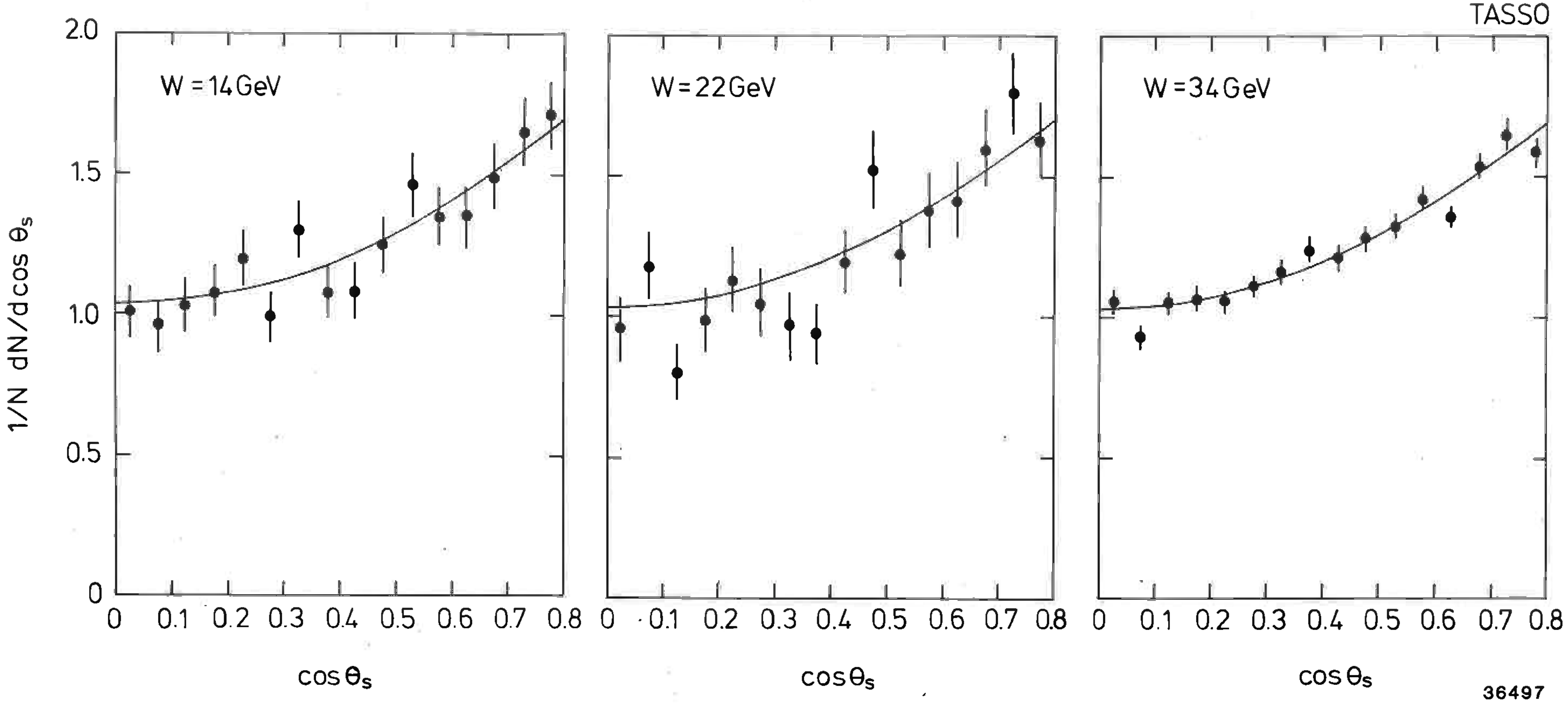
TASSO
W = 14 GeV
W = 22 GeV
W = 34 GeV
1/N dN/d cos θ_s
2.0
1.5
1.0
0.5
0
0 0.1 0.2 0.3 0.4 0.5 0.6 0.7 0.8
cos θ_s
36497

Fig. 23a

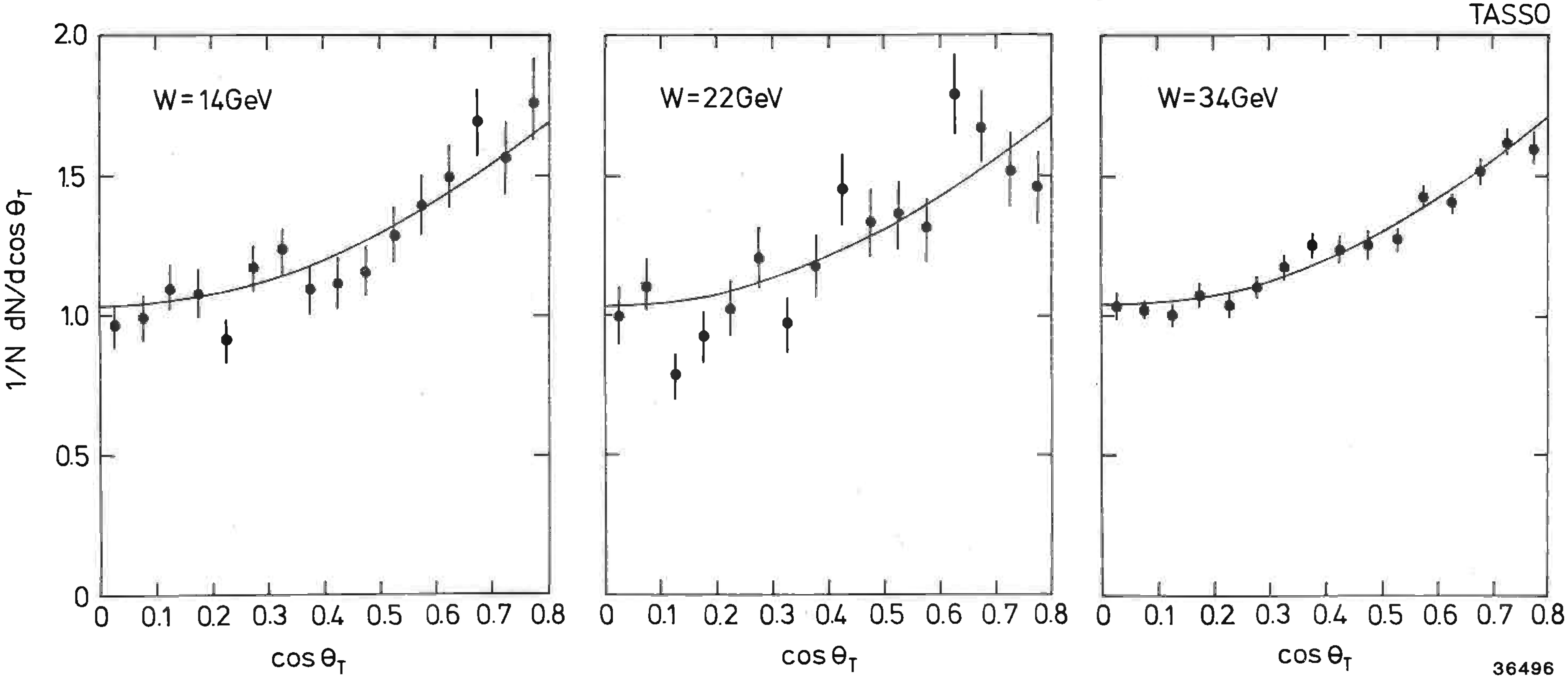
TASSO
W=14GeV
W=22GeV
W=34GeV
1/N dN/dcos θ_T
2.0
1.5
1.0
0.5
0
0
0.1
0.2
0.3
0.4
0.5
0.6
0.7
0.8
cos θ_T
36496

Fig.23b

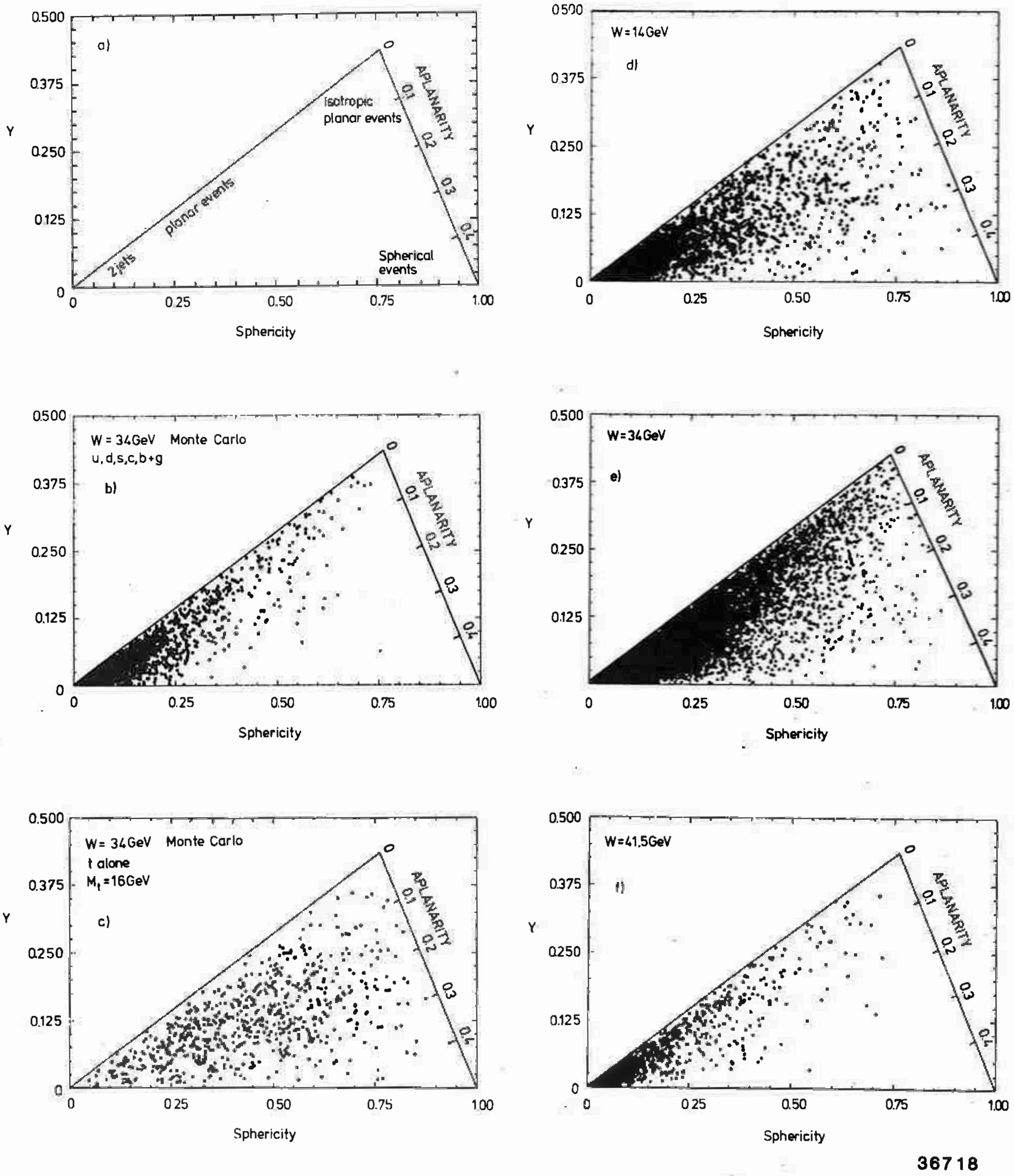
a)
0.500
0.375
0.250
0.125
0
Y
0
0.25
0.50
0.75
1.00
Sphericity
APLANARITY
0
0.1
0.2
0.3
0.4
Isotropic planar events
planar events
2 jets
Spherical events
W = 14GeV
d)
W = 34GeV Monte Carlo
u, d, s, c, b+g
b)
W = 34GeV
e)
W = 34GeV Monte Carlo
t alone
M_t = 16GeV
c)
W = 41.5GeV
f)
36718

Fig. 24

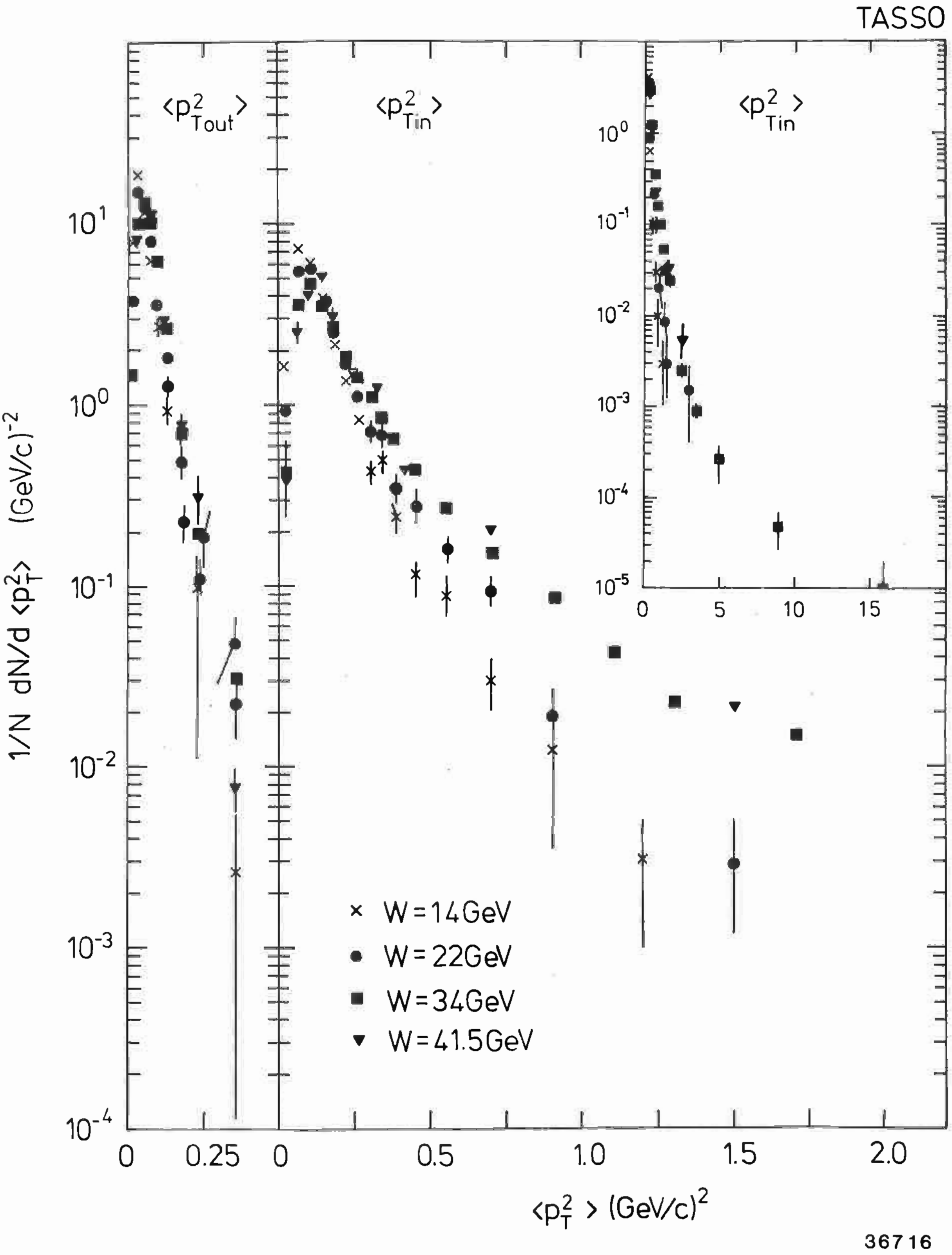
TASSO
$\langle p^2_{Tout} \rangle$
$\langle p^2_{Tin} \rangle$
$\langle p^2_{Tin} \rangle$
1/N dN/d $\langle p_T^2 \rangle$ (GeV/c)$^{-2}$
10^1
10^0
10^{-1}
10^{-2}
10^{-3}
10^{-4}
10^0
10^{-1}
10^{-2}
10^{-3}
10^{-4}
10^{-5}
0
5
10
15
0
0.25
0
0.5
1.0
1.5
2.0
$\langle p_T^2 \rangle$ (GeV/c)^2
× W = 14GeV
● W = 22GeV
■ W = 34GeV
▼ W = 41.5GeV
36716

Fig. 25

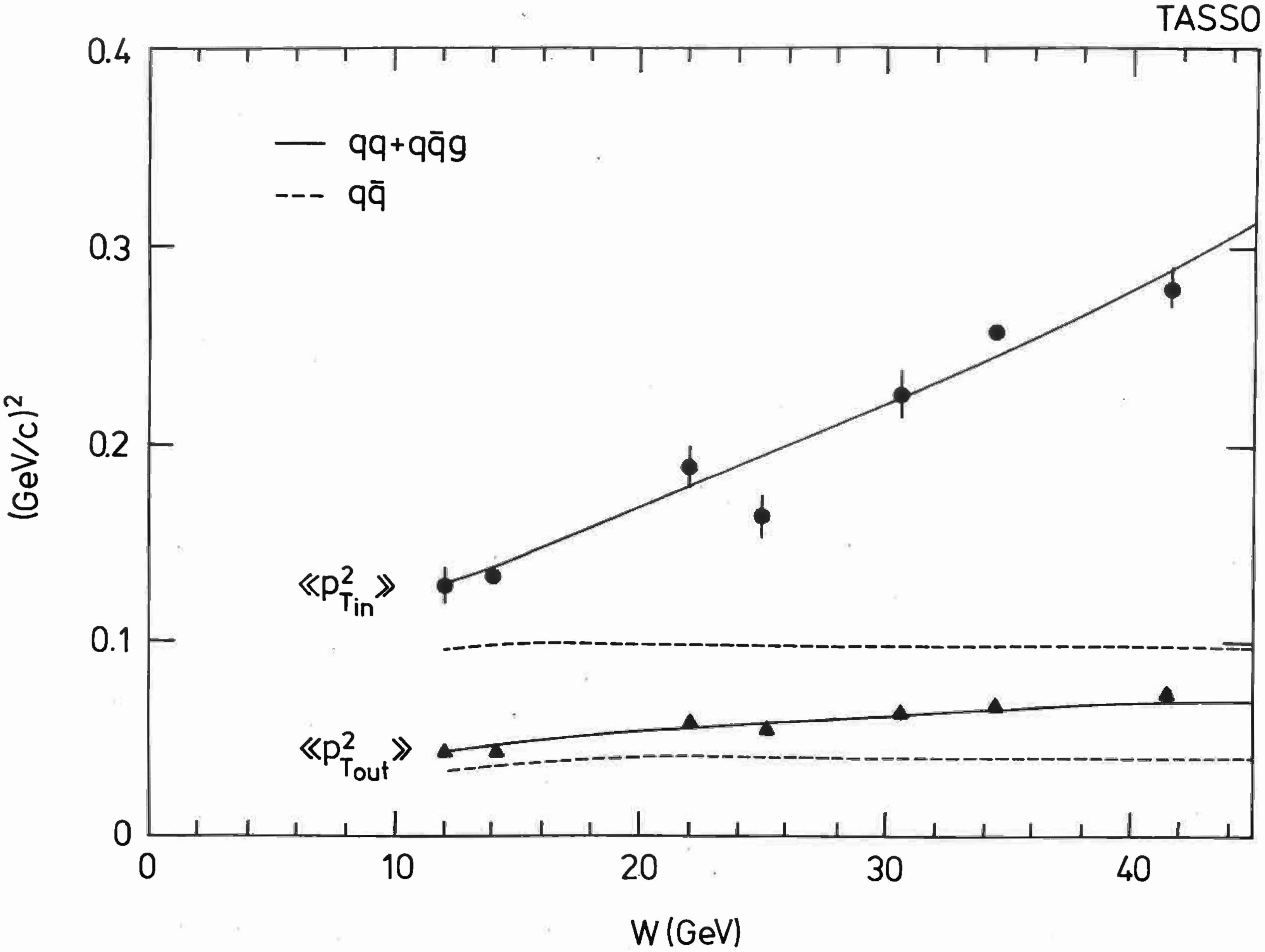
TASSO
0.4
0.3
0.2
0.1
0
(GeV/c)²
qq+qq̄g
qq̄
«p²_Tin»
«p²_Tout»
0
10
20
30
40
W (GeV)

Fig. 26

36680

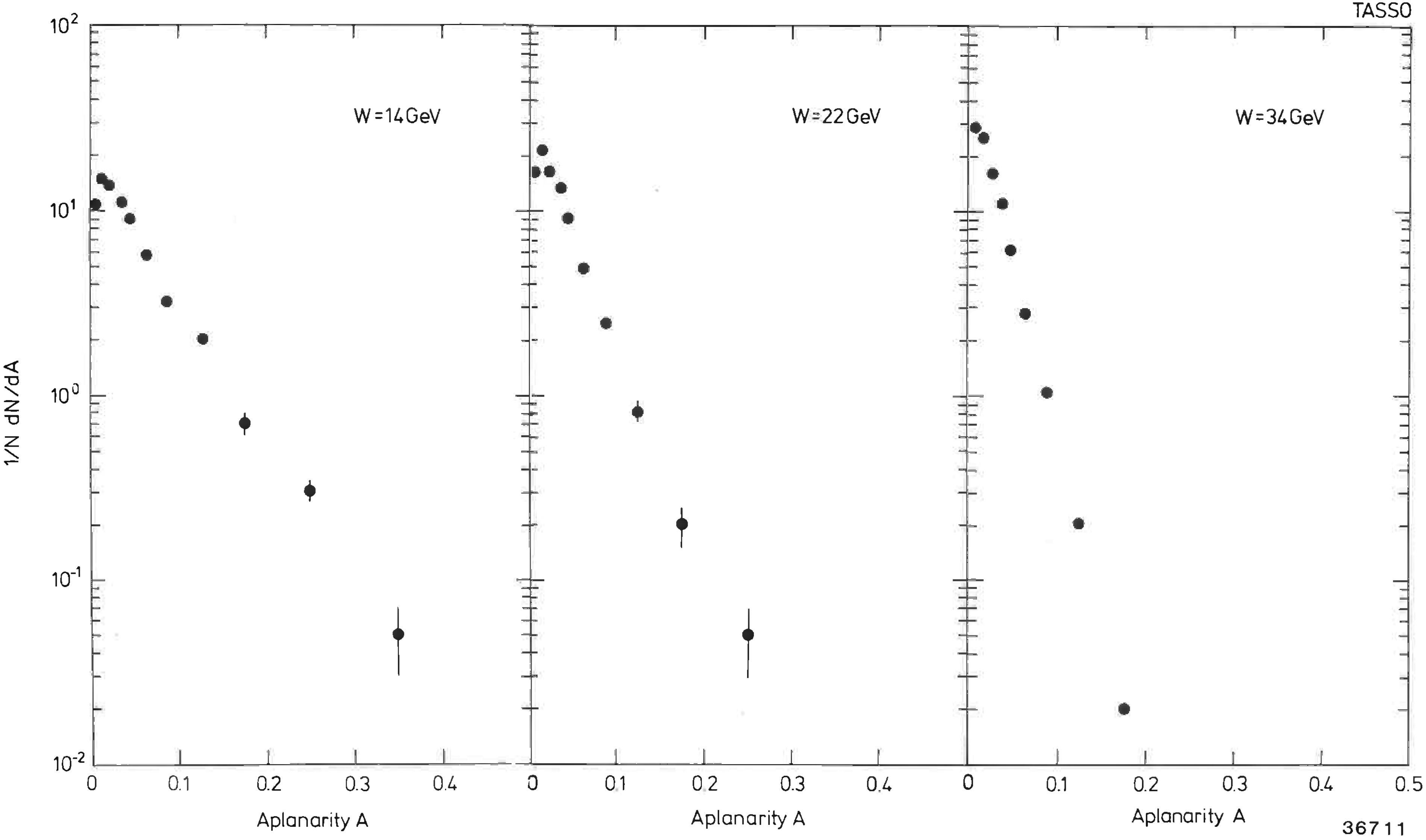
TASSO
W=14GeV
W=22GeV
W=34GeV
1/N dN/dA
10^2
10^1
10^0
10^{-1}
10^{-2}
0
0.1
0.2
0.3
0.4
0.5
Aplanarity A
36711

Fig. 27

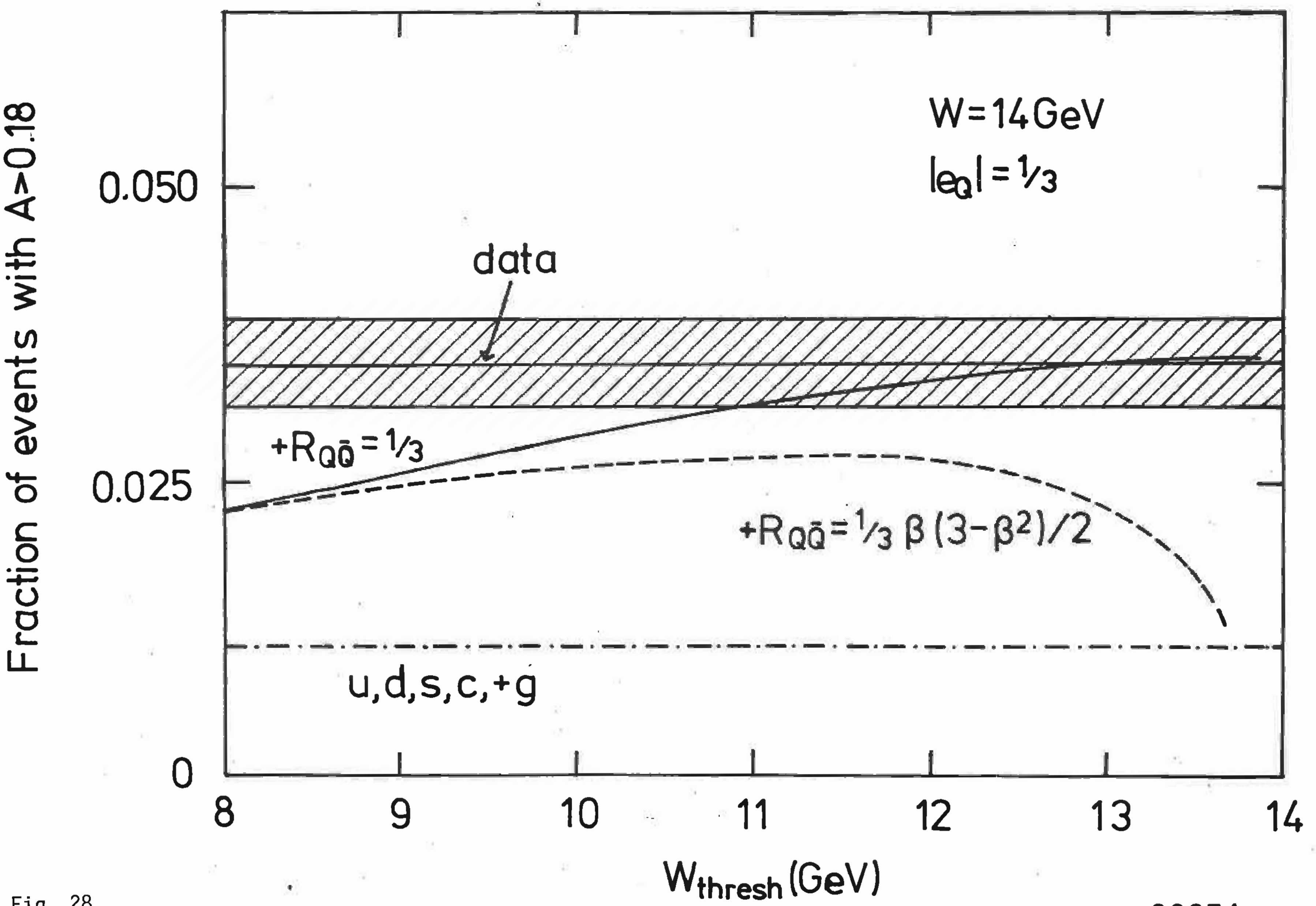
W=14GeV
$|e_Q|=1/3$
data
$+R_{Q\bar{Q}}=1/3$
$+R_{Q\bar{Q}}=1/3\,\beta(3-\beta^2)/2$
u,d,s,c,+g
Fraction of events with A>0.18
0.050
0.025
0
8
9
10
11
12
13
14
W_{thresh} (GeV)

Fig. 28

36674

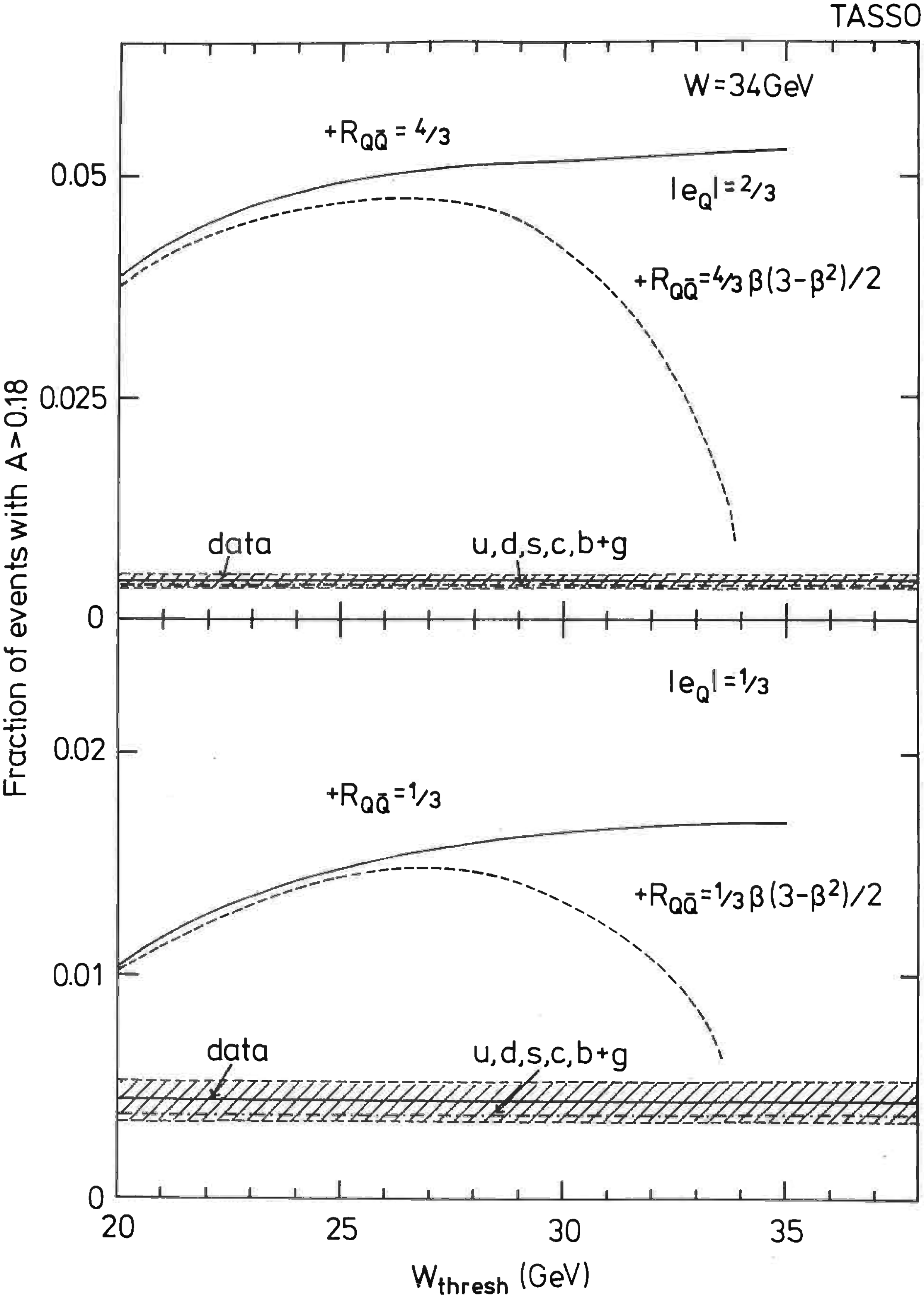
TASSO
W=34GeV
+$R_{Q\bar{Q}}$ = 4/3
$|e_Q|$=2/3
+$R_{Q\bar{Q}}$=4/3 $\beta(3-\beta^2)/2$
data
u,d,s,c,b+g
$|e_Q|$=1/3
+$R_{Q\bar{Q}}$=1/3
+$R_{Q\bar{Q}}$=1/3 $\beta(3-\beta^2)/2$
data
u,d,s,c,b+g
Fraction of events with A>0.18
0.05
0.025
0
0.02
0.01
0
20
25
30
35
W_{thresh} (GeV)
36686

Fig. 29a

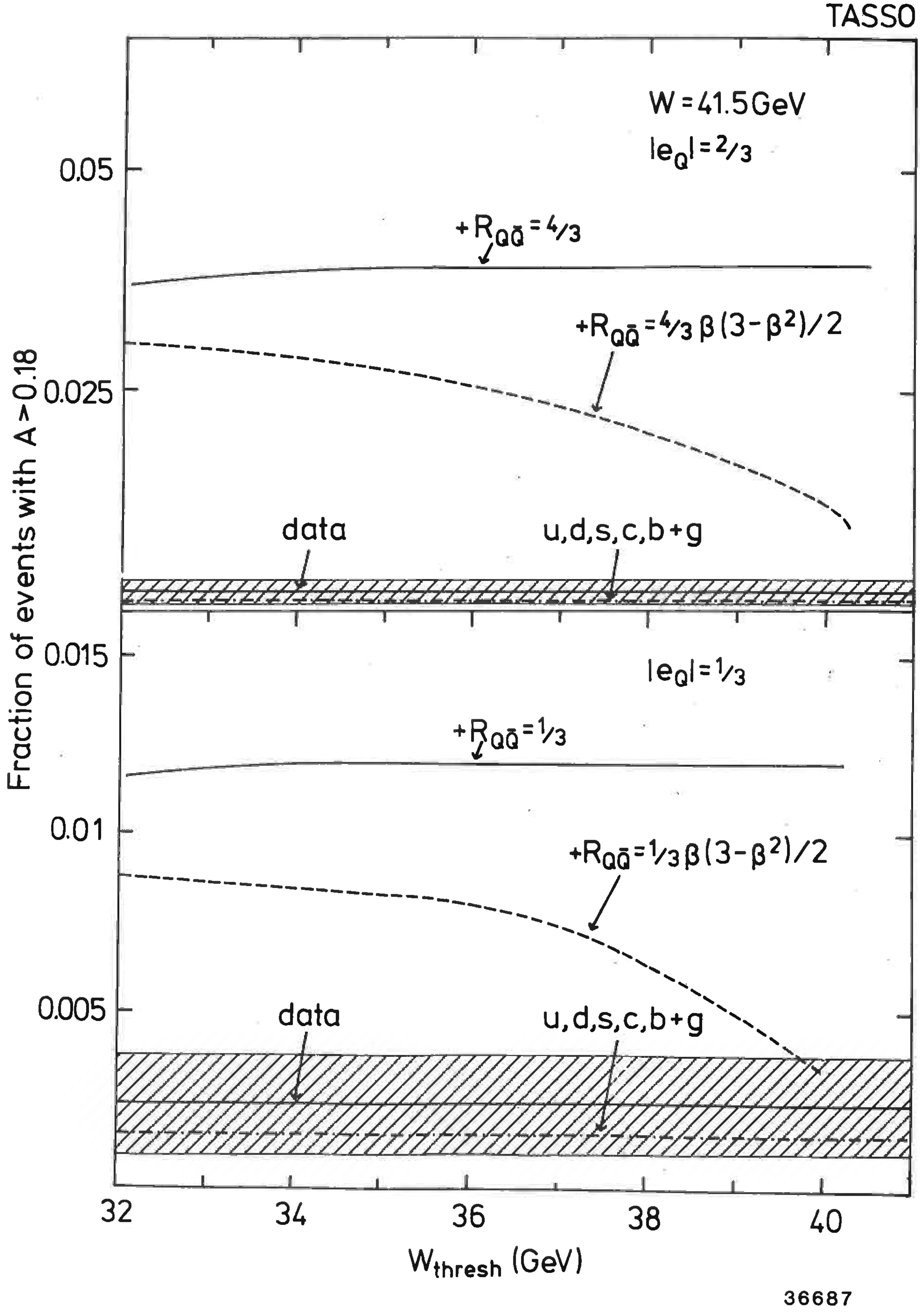
TASSO
W = 41.5 GeV
$|e_Q| = 2/3$
$+R_{Q\bar{Q}} = 4/3$
$+R_{Q\bar{Q}} = 4/3\,\beta(3-\beta^2)/2$
data
u,d,s,c,b+g
$|e_Q| = 1/3$
$+R_{Q\bar{Q}} = 1/3$
$+R_{Q\bar{Q}} = 1/3\,\beta(3-\beta^2)/2$
data
u,d,s,c,b+g
0.05
0.025
0.015
0.01
0.005
Fraction of events with A > 0.18
32
34
36
38
40
W_{thresh} (GeV)
36687

Fig. 29b

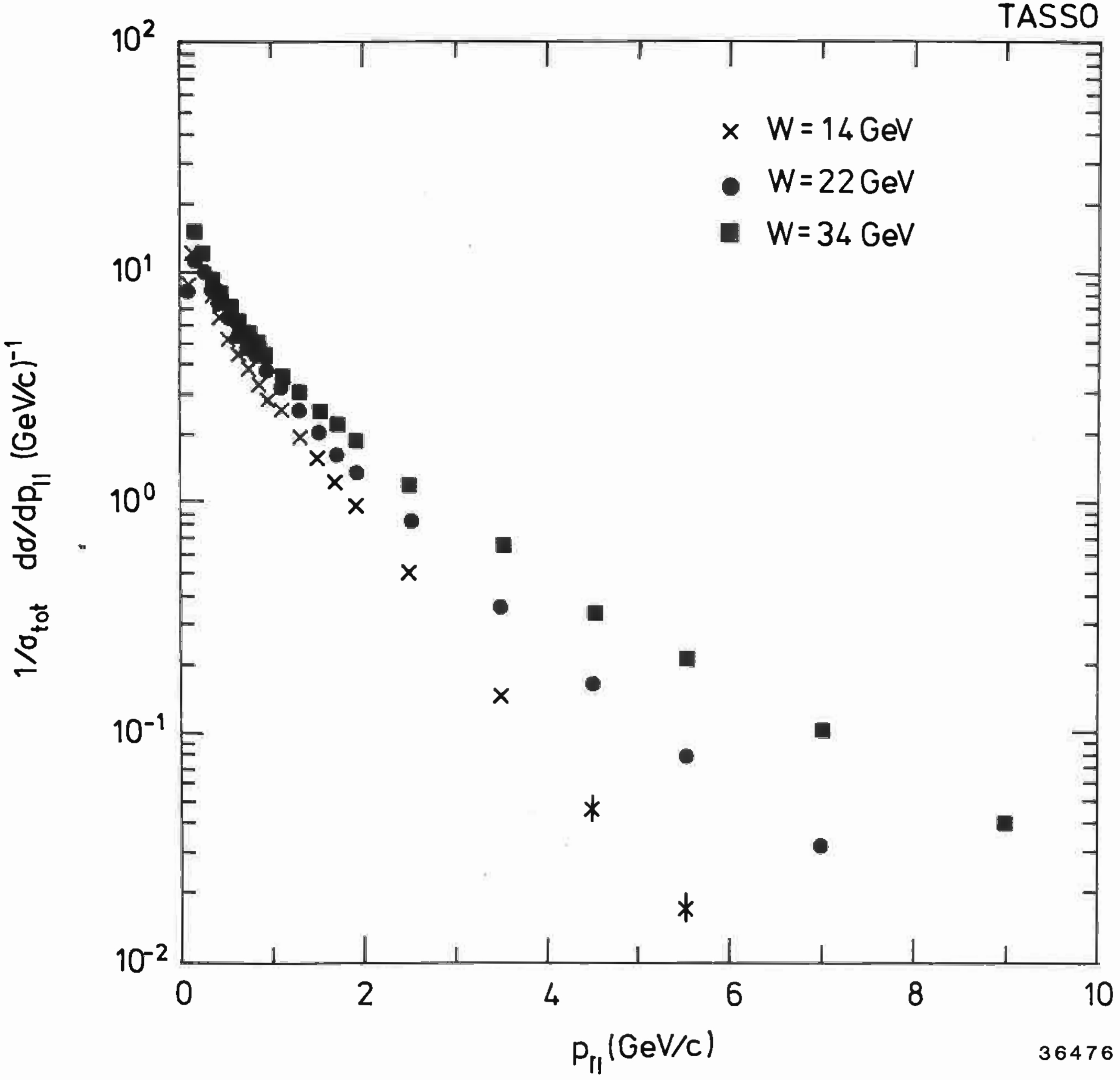
TASSO
× W = 14 GeV
● W = 22 GeV
■ W = 34 GeV
10^2
10^1
10^0
10^{-1}
10^{-2}
$1/\sigma_{tot} \ d\sigma/dp_{||} \ (GeV/c)^{-1}$
0
2
4
6
8
10
$p_{||}$ (GeV/c)
36476

Fig. 30

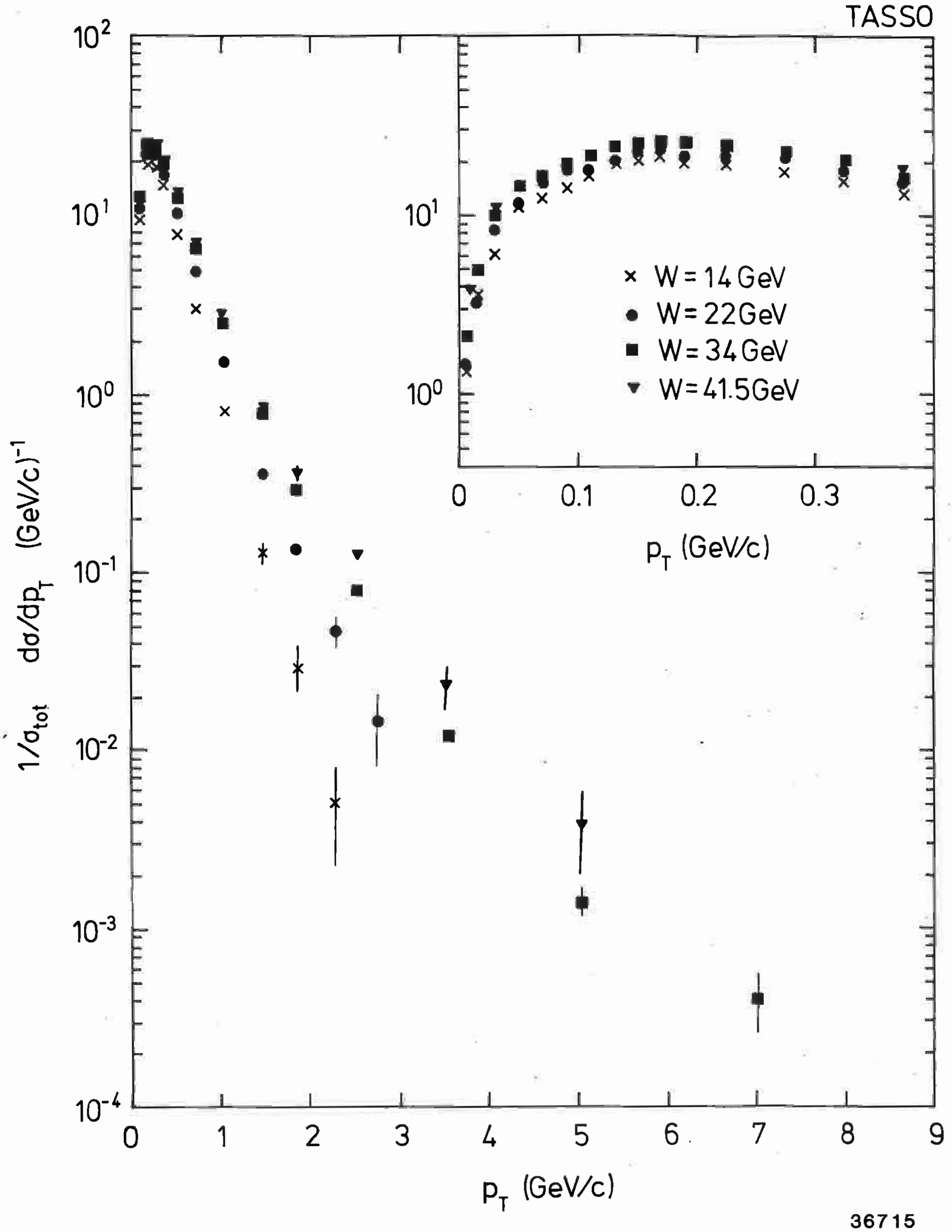
TASSO
$1/\sigma_{tot}\ d\sigma/dp_T\ (GeV/c)^{-1}$
10^2
10^1
10^0
10^{-1}
10^{-2}
10^{-3}
10^{-4}
0
1
2
3
4
5
6
7
8
9
p_T (GeV/c)
10^1
10^0
0
0.1
0.2
0.3
p_T (GeV/c)
× W = 14 GeV
● W = 22 GeV
■ W = 34 GeV
▼ W = 41.5 GeV

36715

Fig. 31

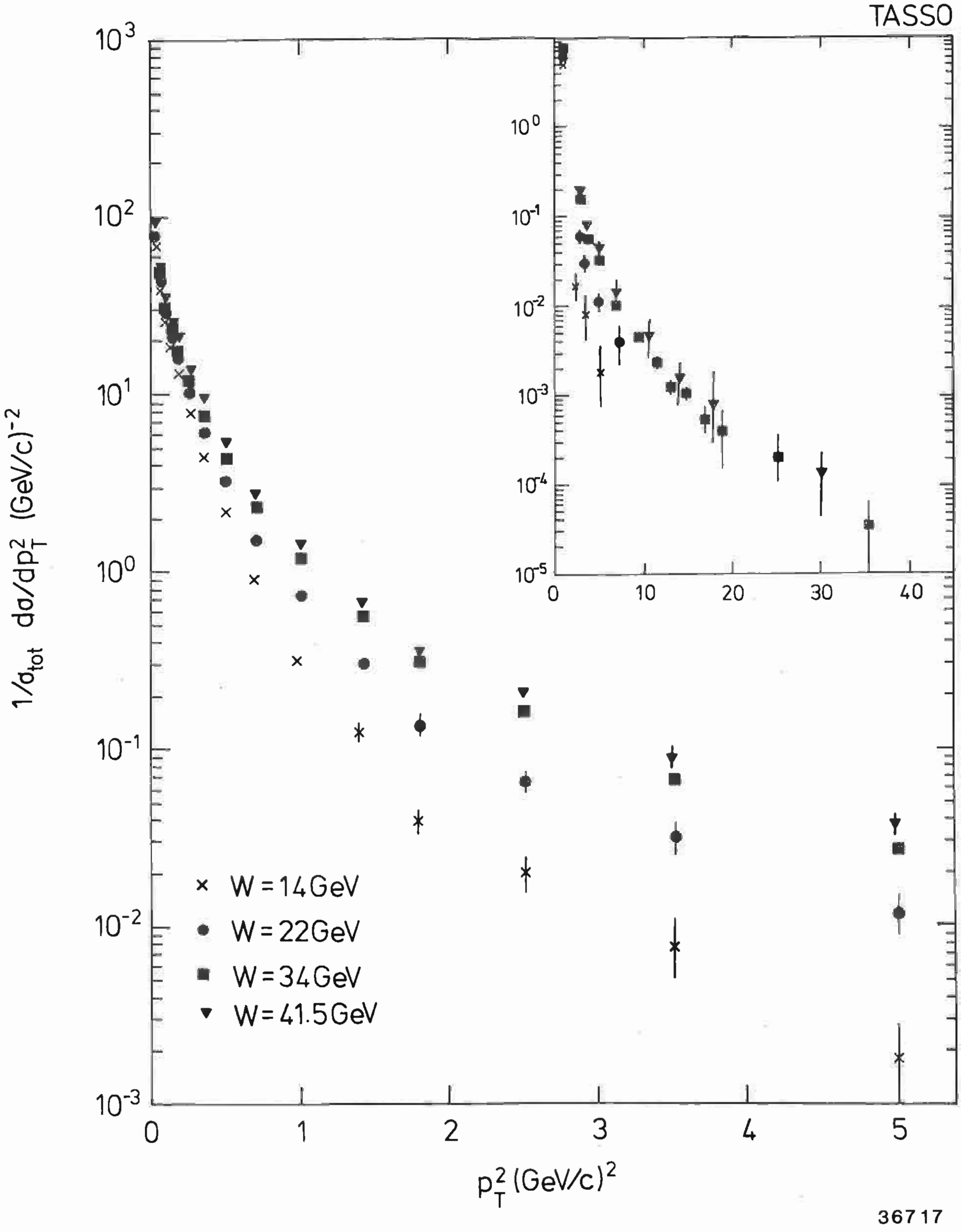
TASSO
10^3
10^2
10^1
10^0
10^{-1}
10^{-2}
10^{-3}
$1/\sigma_{tot}\ d\sigma/dp_T^2\ (GeV/c)^{-2}$
0
1
2
3
4
5
$p_T^2\ (GeV/c)^2$
× W = 14 GeV
● W = 22 GeV
■ W = 34 GeV
▼ W = 41.5 GeV
10^0
10^{-1}
10^{-2}
10^{-3}
10^{-4}
10^{-5}
0
10
20
30
40
36717

Fig. 32

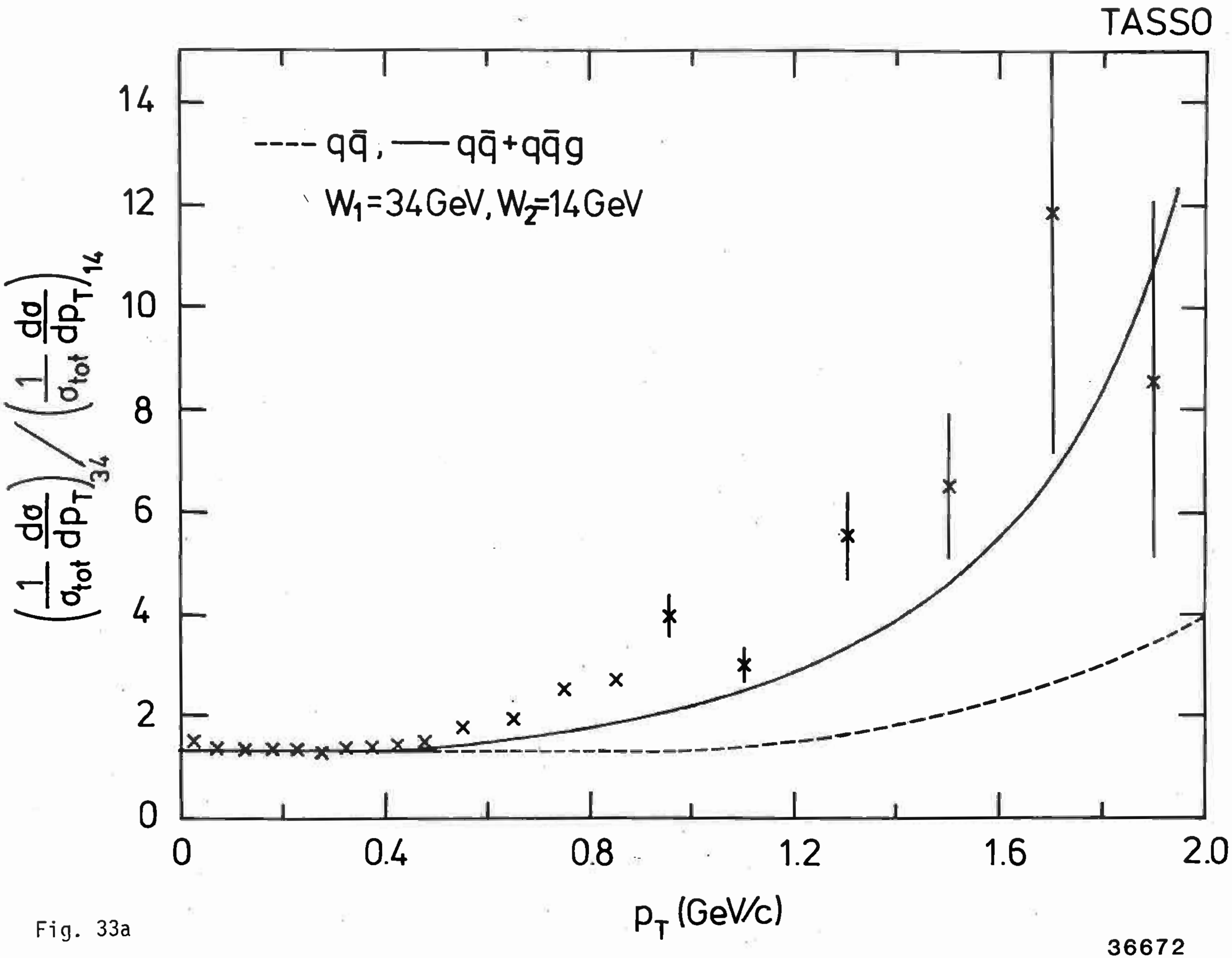

Fig. 33a

36672

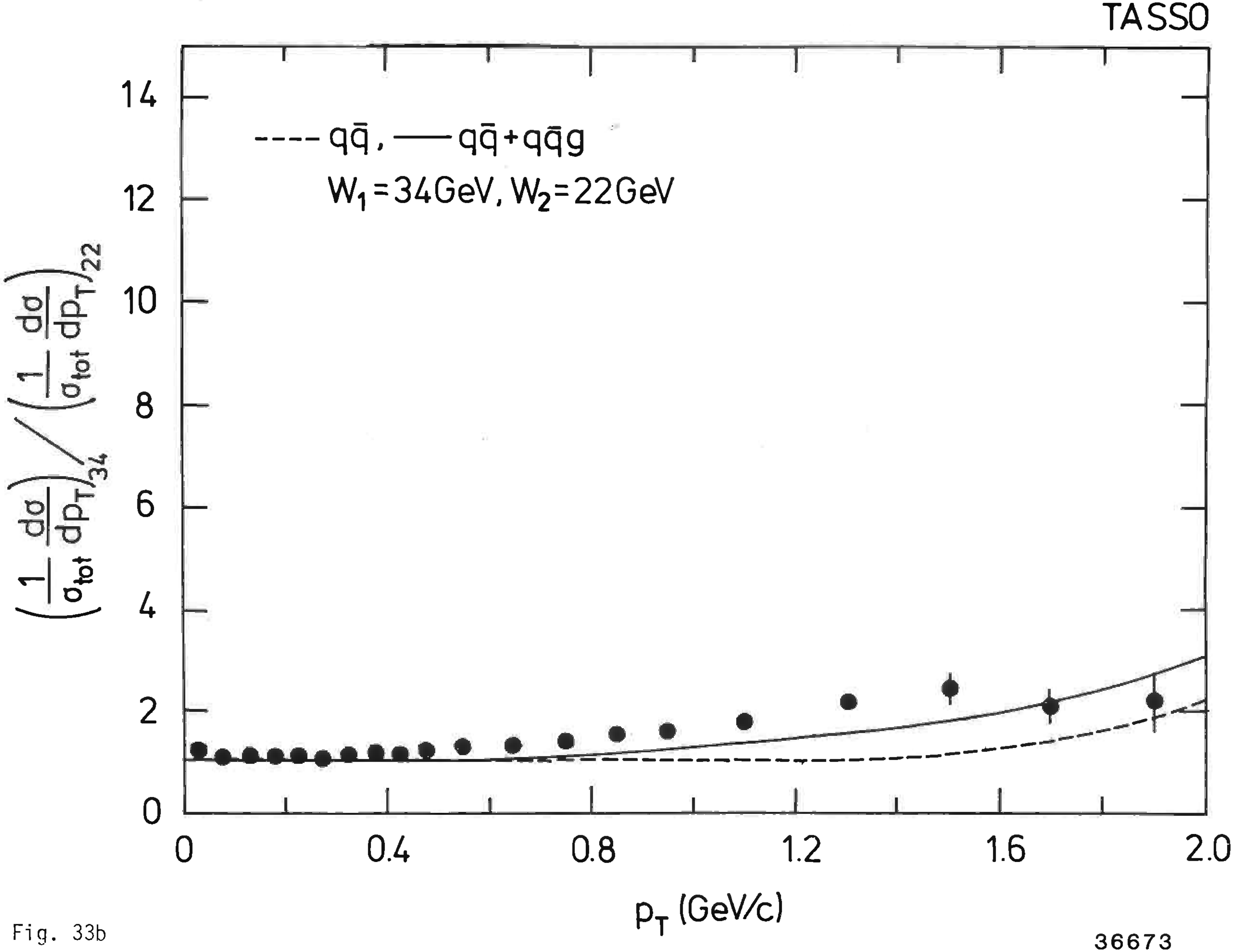

Fig. 33b

36673

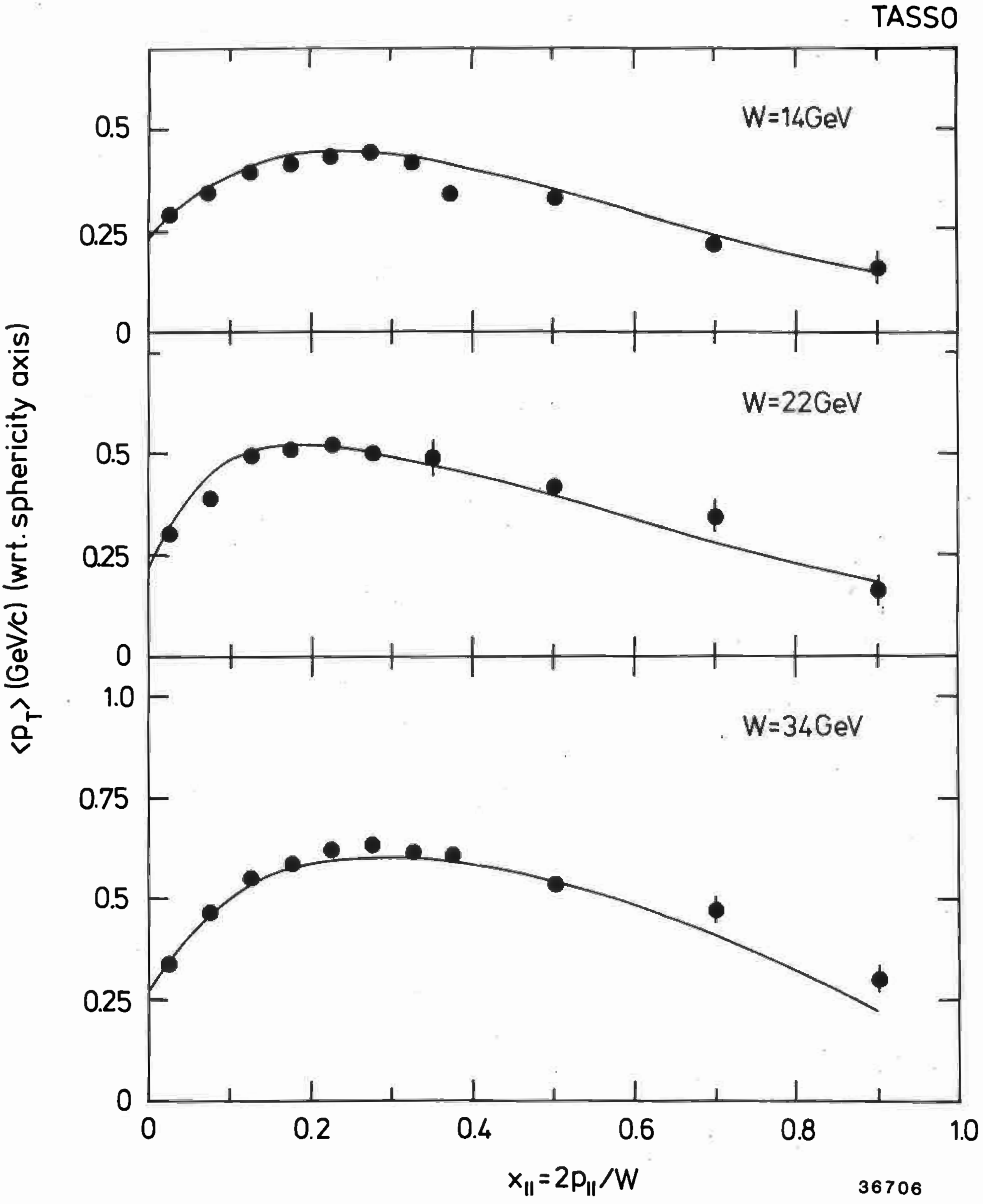
TASSO
W=14GeV
W=22GeV
W=34GeV
0.5
0.25
0
1.0
0.75
⟨p_T⟩ (GeV/c) (wrt. sphericity axis)
0
0.2
0.4
0.6
0.8
1.0
x_∥ = 2p_∥/W
36706

Fig. 34a

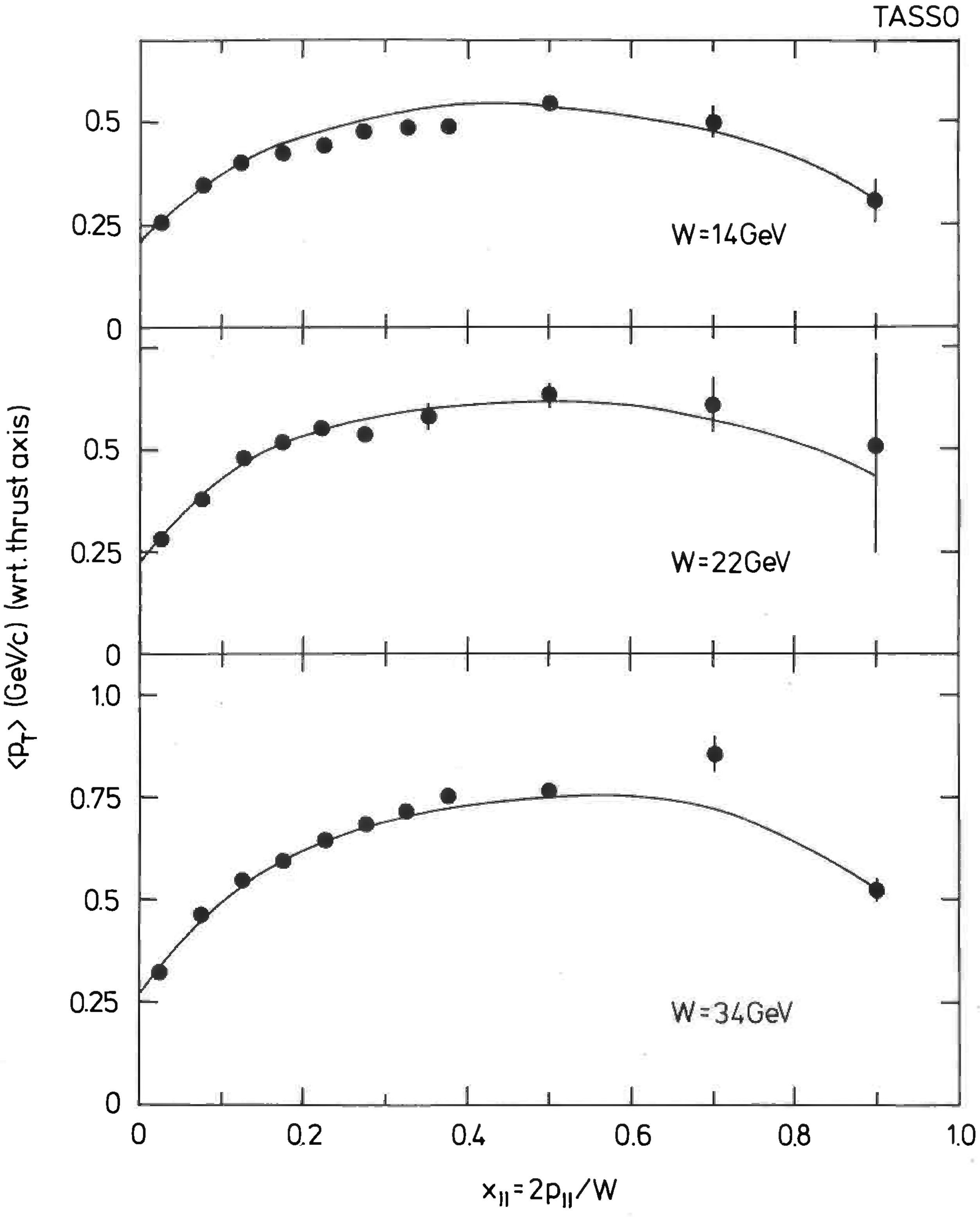
TASSO
W=14GeV
W=22GeV
W=34GeV
⟨p_T⟩ (GeV/c) (wrt. thrust axis)
$x_{||}=2p_{||}/W$
0
0.25
0.5
0.75
1.0
0
0.2
0.4
0.6
0.8
1.0
36700

Fig. 34b

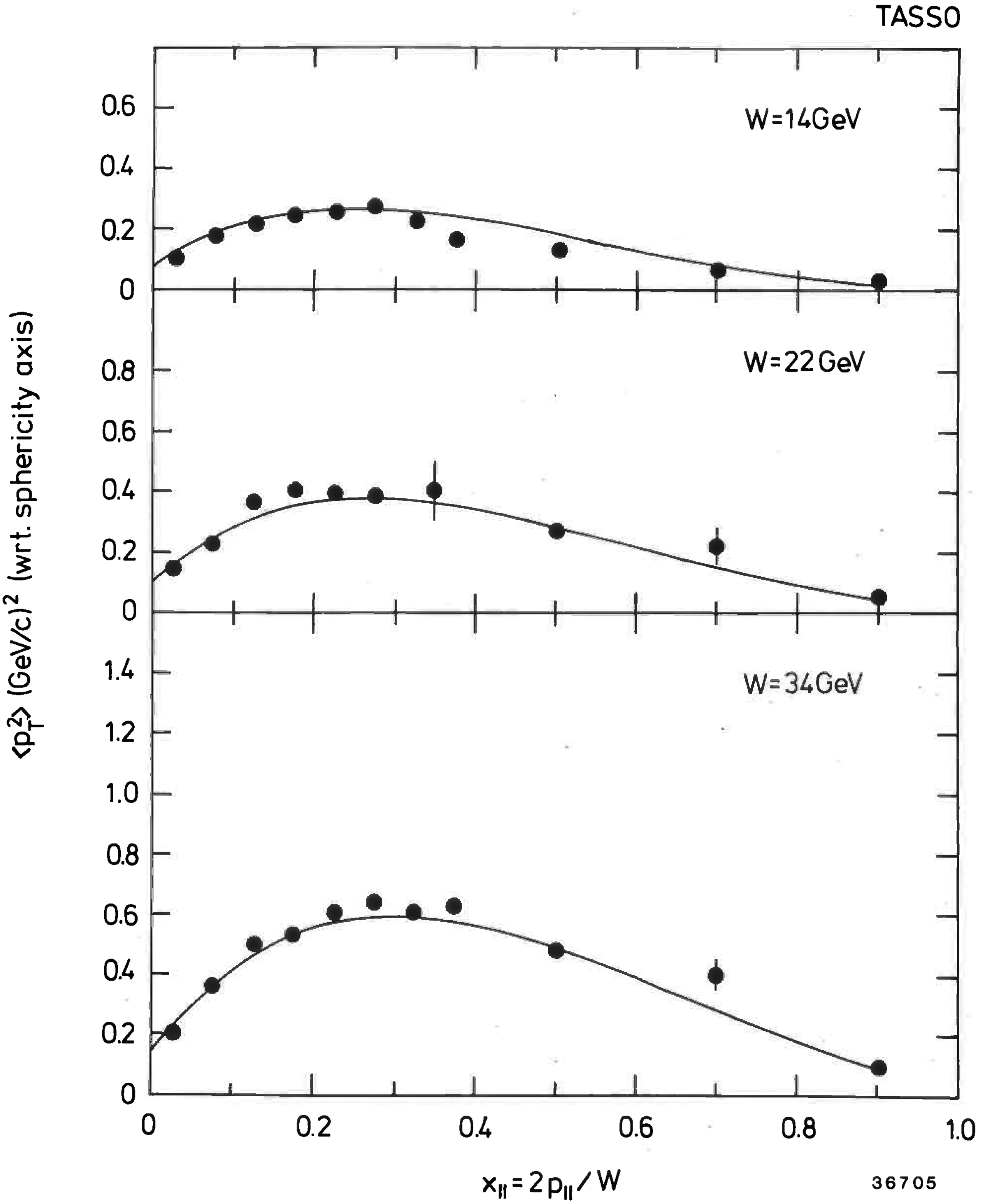
TASSO
W=14GeV
W=22GeV
W=34GeV
$\langle p_T^2 \rangle$ (GeV/c)^2 (wrt. sphericity axis)
0
0.2
0.4
0.6
0.8
1.0
1.2
1.4
0
0.2
0.4
0.6
0.8
1.0
$x_{\parallel} = 2p_{\parallel}/W$
36705

Fig. 35a

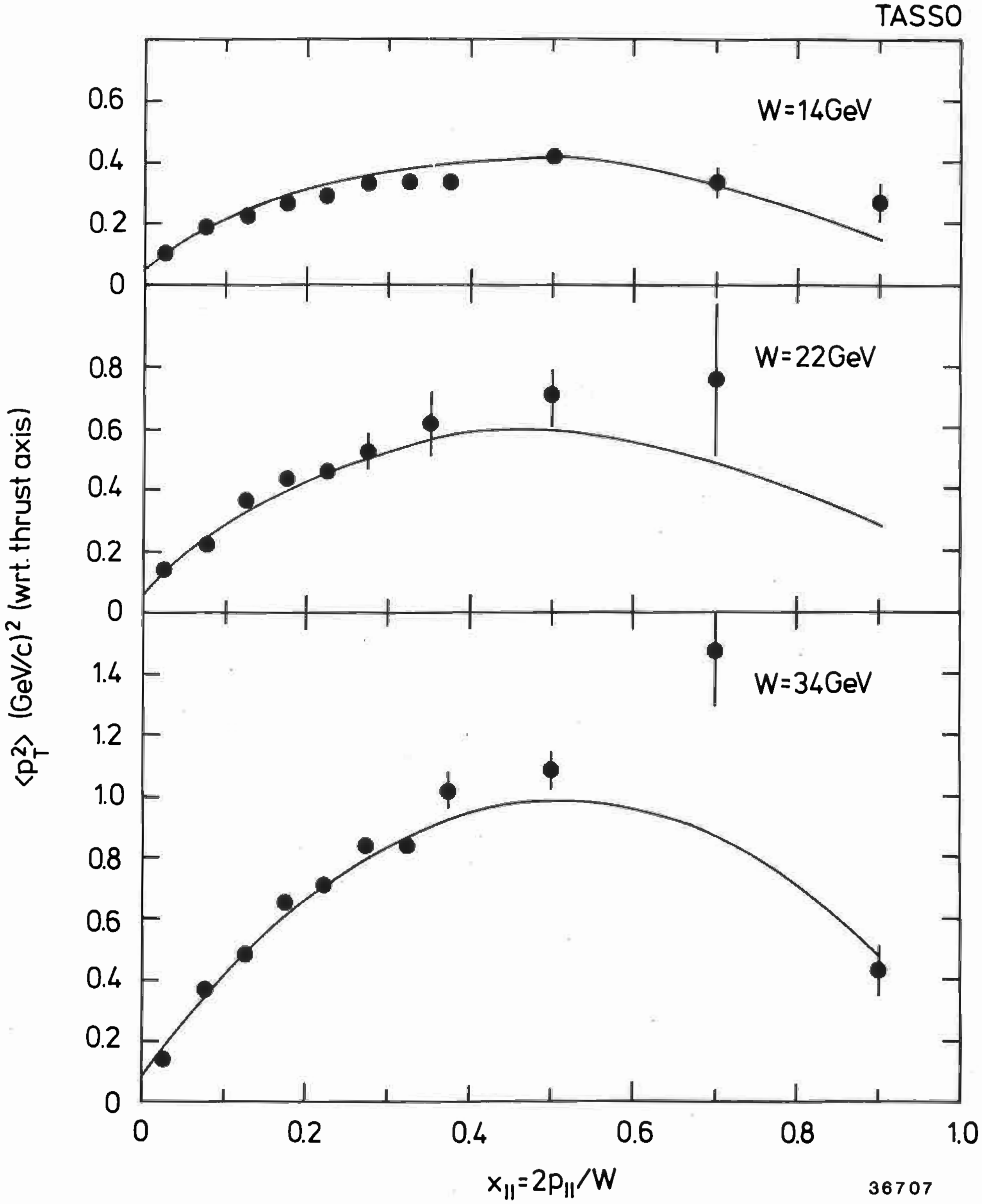
TASSO
W=14GeV
W=22GeV
W=34GeV
$\langle p_T^2 \rangle$ (GeV/c)^2 (wrt. thrust axis)
$x_{\parallel}=2p_{\parallel}/W$
0
0.2
0.4
0.6
0.8
1.0
1.2
1.4
36707

Fig. 35b

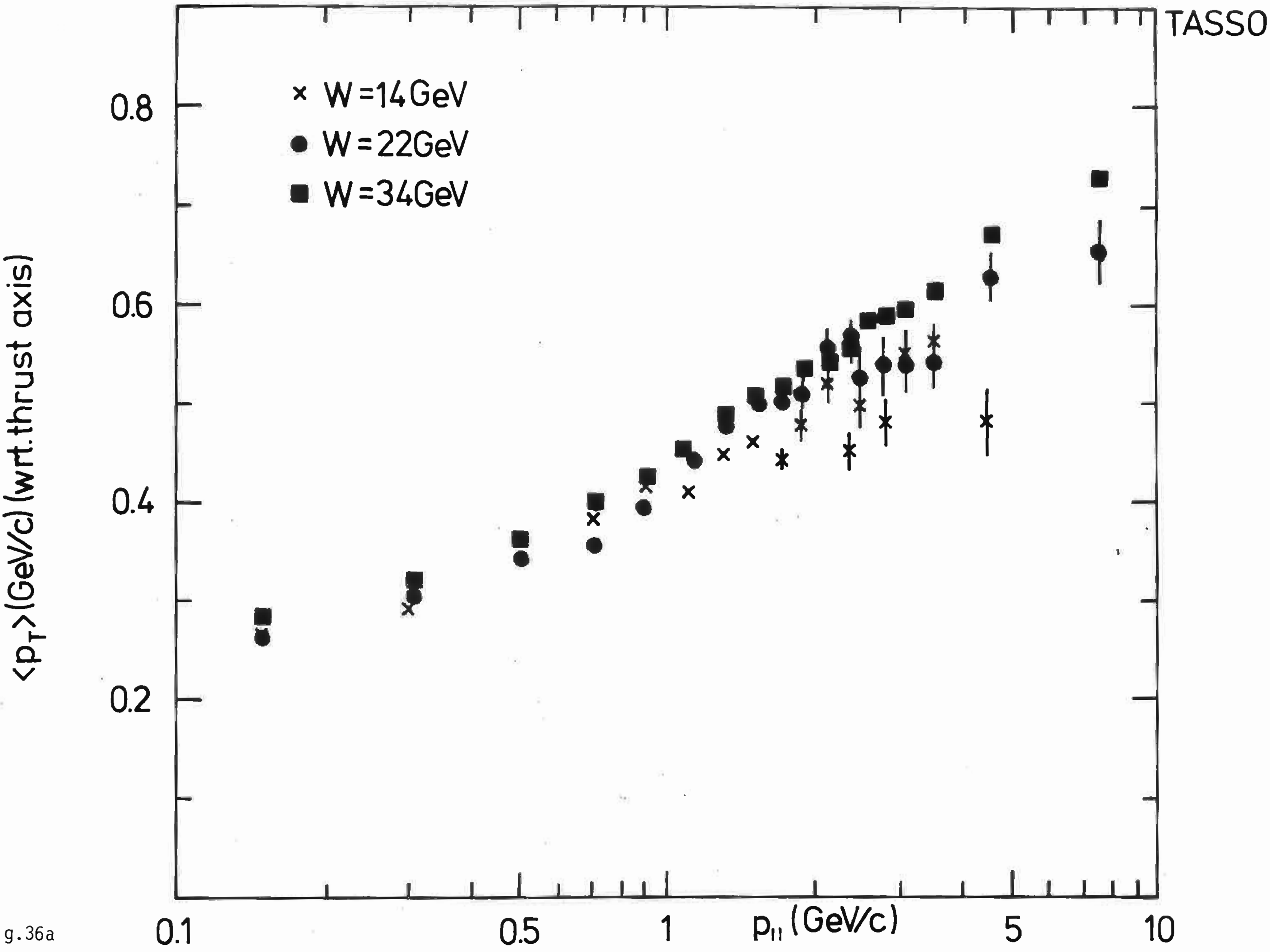
TASSO
× W = 14 GeV
● W = 22 GeV
■ W = 34 GeV
0.8
0.6
0.4
0.2
<p_T> (GeV/c) (wrt. thrust axis)
0.1
0.5
1
5
10
p_∥ (GeV/c)

Fig.36a

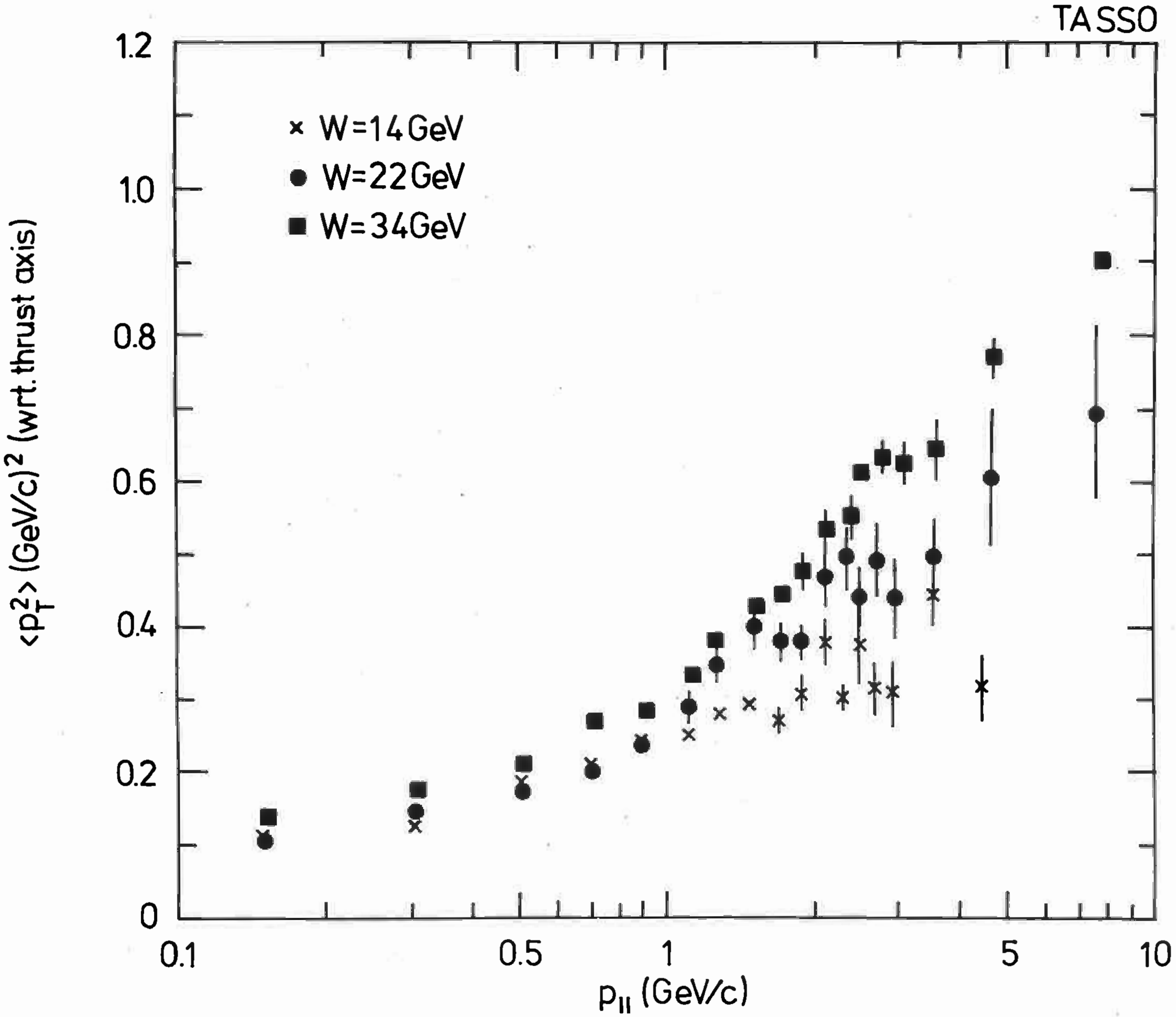

Fig. 36b

36679

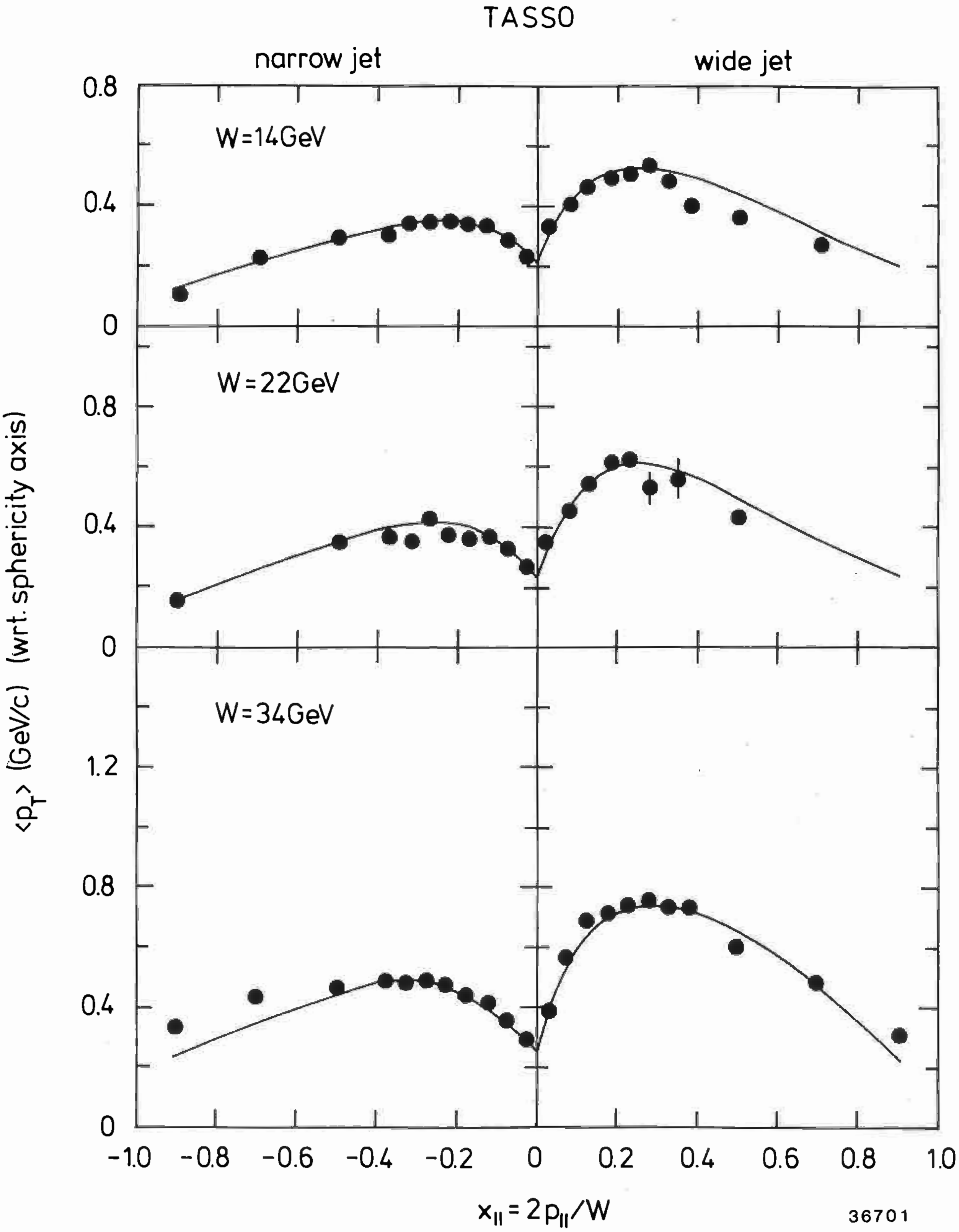
TASSO
narrow jet
wide jet
W=14GeV
W=22GeV
W=34GeV
0.8
0.4
0
0.8
0.4
0
1.2
0.8
0.4
0
<p_T> (GeV/c) (wrt. sphericity axis)
-1.0
-0.8
-0.6
-0.4
-0.2
0
0.2
0.4
0.6
0.8
1.0
x_∥ = 2p_∥/W
36701

Fig. 37a

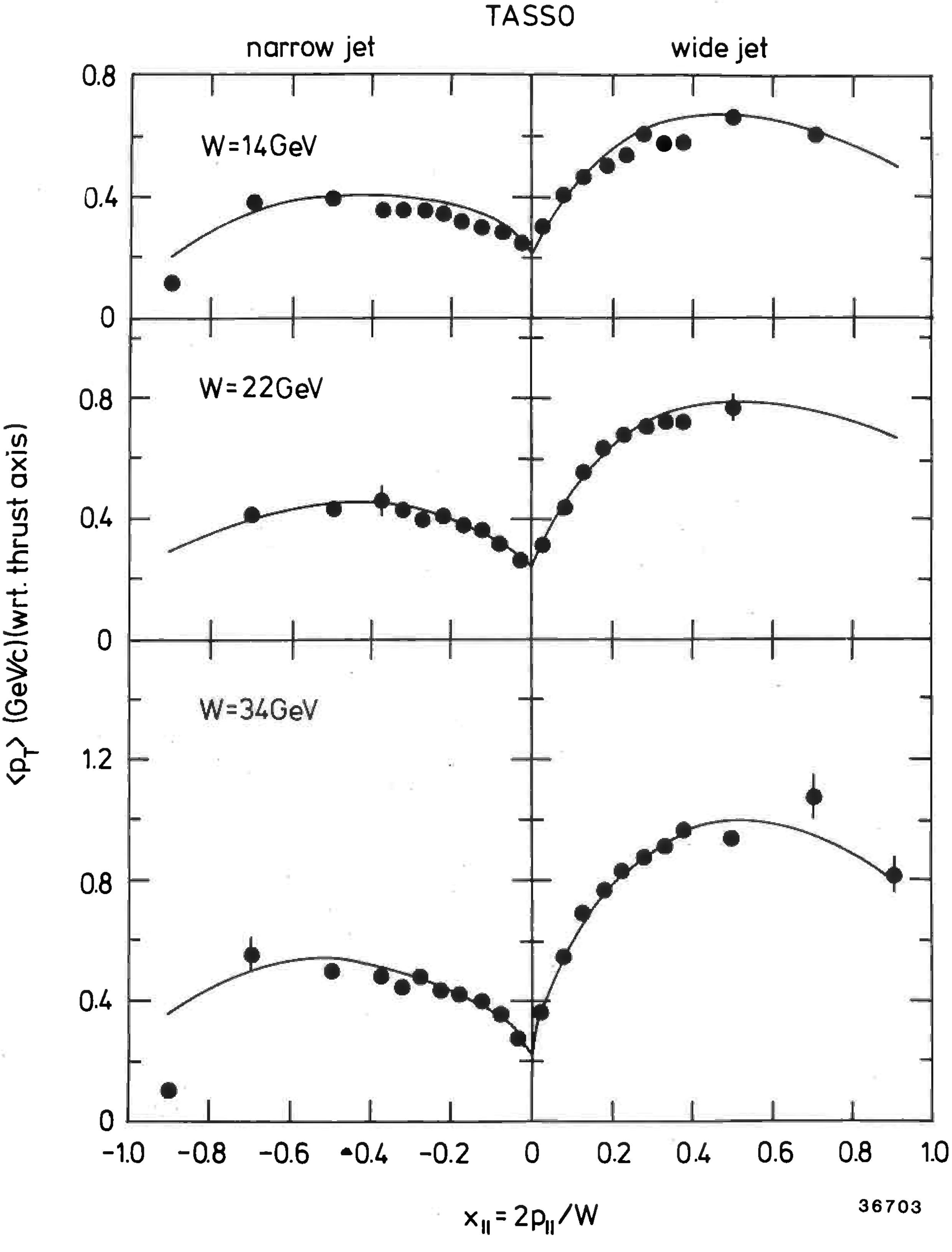
TASSO
narrow jet
wide jet
W=14GeV
W=22GeV
W=34GeV
0.8
0.4
0
0.8
0.4
0
1.2
0.8
0.4
0
⟨p_T⟩ (GeV/c)(wrt. thrust axis)
-1.0
-0.8
-0.6
-0.4
-0.2
0
0.2
0.4
0.6
0.8
1.0
x_∥ = 2p_∥/W
36703

Fig. 37b

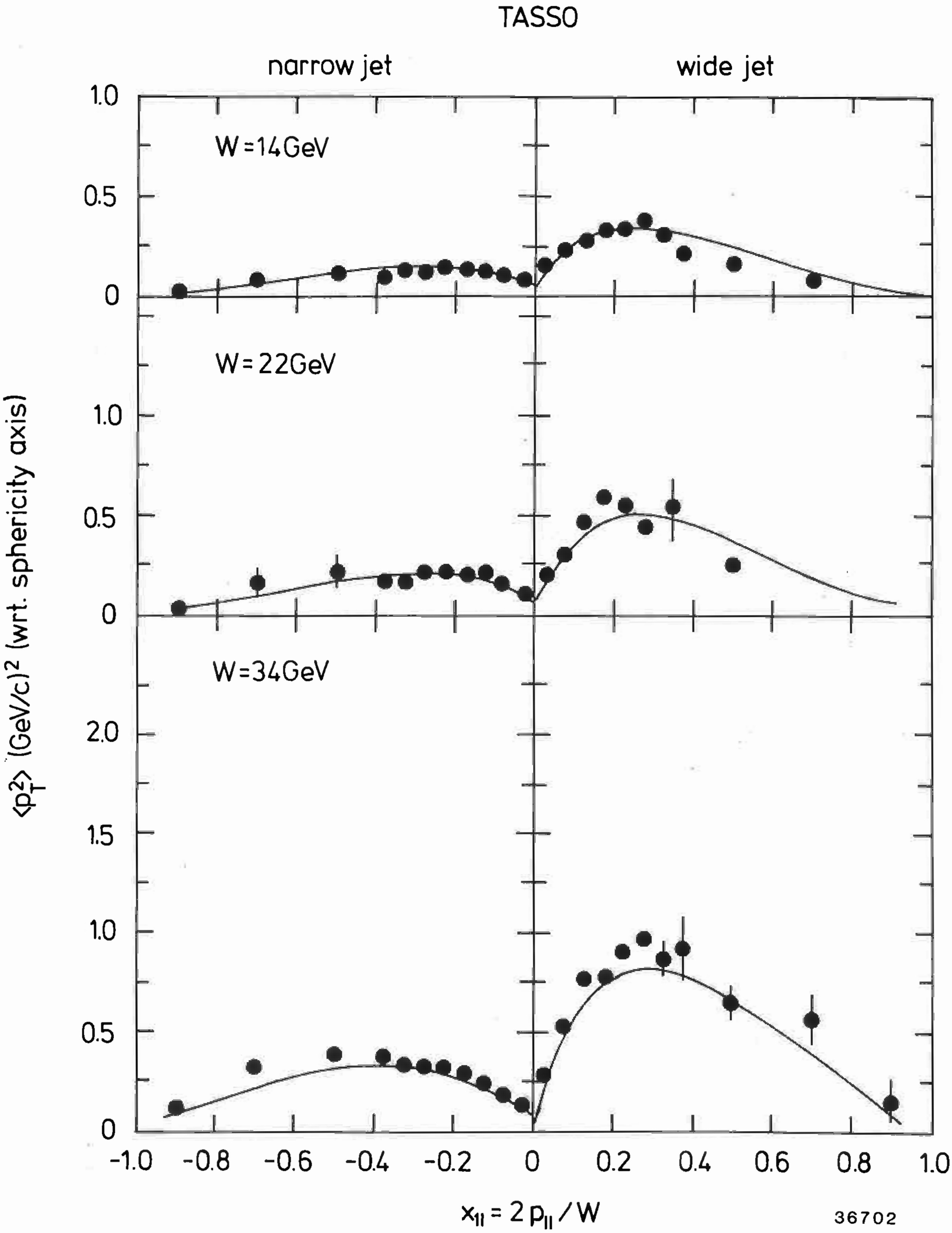
TASSO
narrow jet
wide jet
W=14GeV
W=22GeV
W=34GeV
$\langle p_T^2 \rangle$ (GeV/c)^2 (wrt. sphericity axis)
1.0
0.5
0
1.0
0.5
0
2.0
1.5
1.0
0.5
0
-1.0
-0.8
-0.6
-0.4
-0.2
0
0.2
0.4
0.6
0.8
1.0
$x_{\parallel} = 2\,p_{\parallel}/W$
36702

Fig. 38a

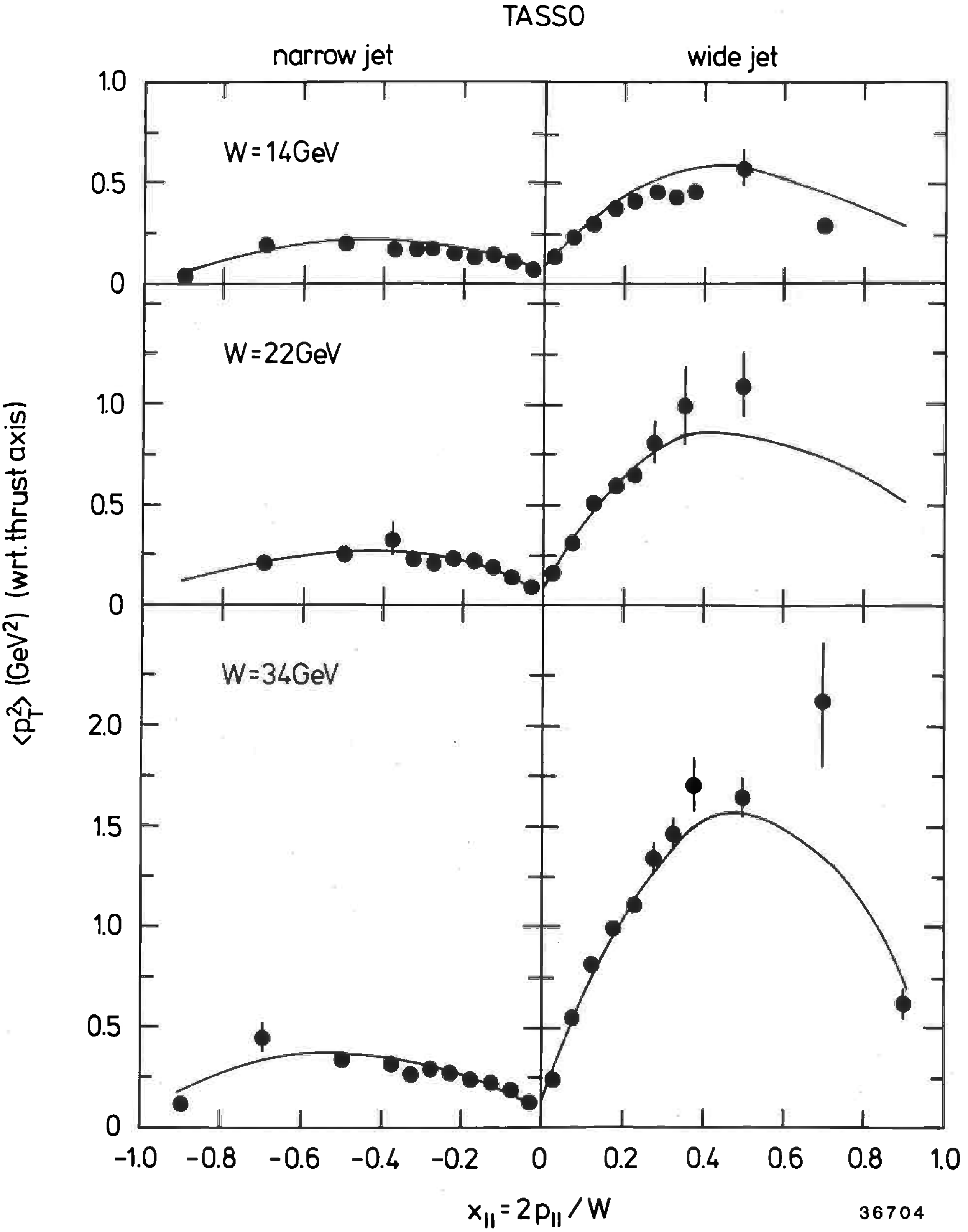
TASSO
narrow jet
wide jet
W=14GeV
W=22GeV
W=34GeV
$\langle p_T^2 \rangle$ (GeV^2) (wrt. thrust axis)
1.0
0.5
0
1.0
0.5
0
2.0
1.5
1.0
0.5
0
-1.0
-0.8
-0.6
-0.4
-0.2
0
0.2
0.4
0.6
0.8
1.0
$x_{II} = 2p_{II}/W$
36704

Fig. 38b

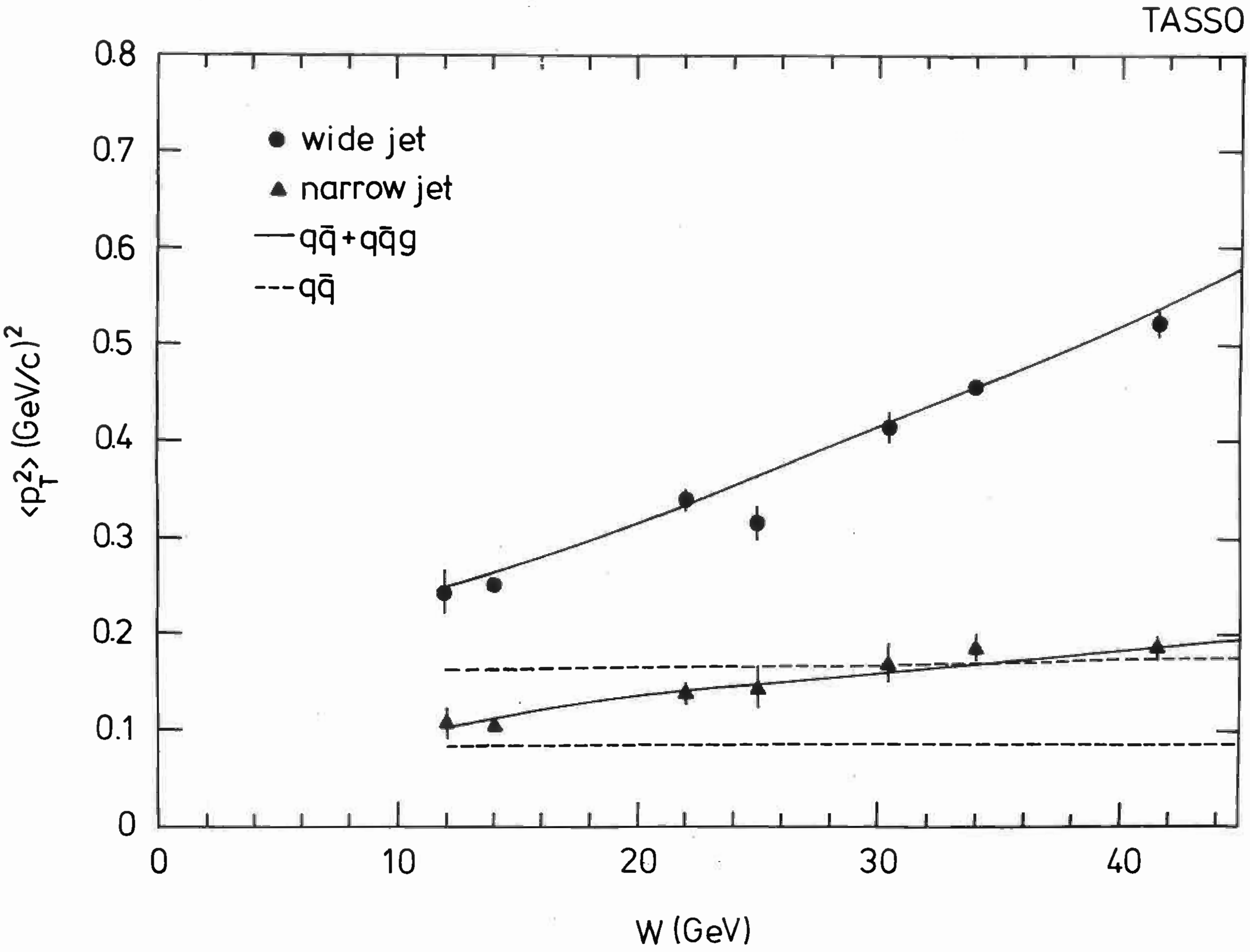
TASSO
● wide jet
▲ narrow jet
— $q\bar{q}+q\bar{q}g$
--- $q\bar{q}$
$\langle p_T^2 \rangle$ (GeV/c)^2
0.8
0.7
0.6
0.5
0.4
0.3
0.2
0.1
0
0
10
20
30
40
W (GeV)

Fig. 39

36681

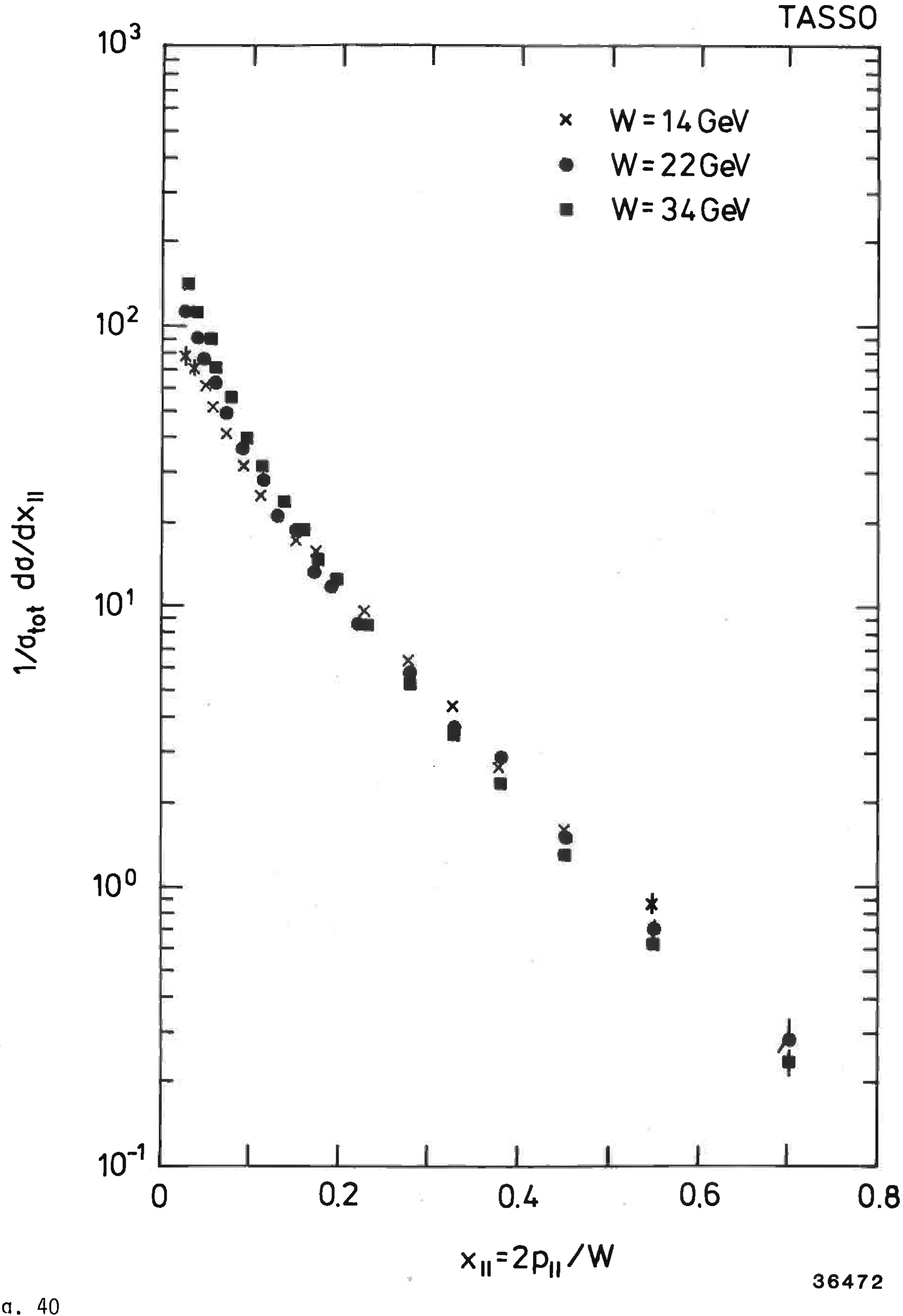TASSO
× W = 14 GeV
● W = 22 GeV
■ W = 34 GeV
10^3
10^2
10^1
10^0
10^{-1}
$1/\sigma_{tot}\ d\sigma/dx_{\parallel}$
0
0.2
0.4
0.6
0.8
$x_{\parallel} = 2p_{\parallel}/W$
36472

Fig. 40

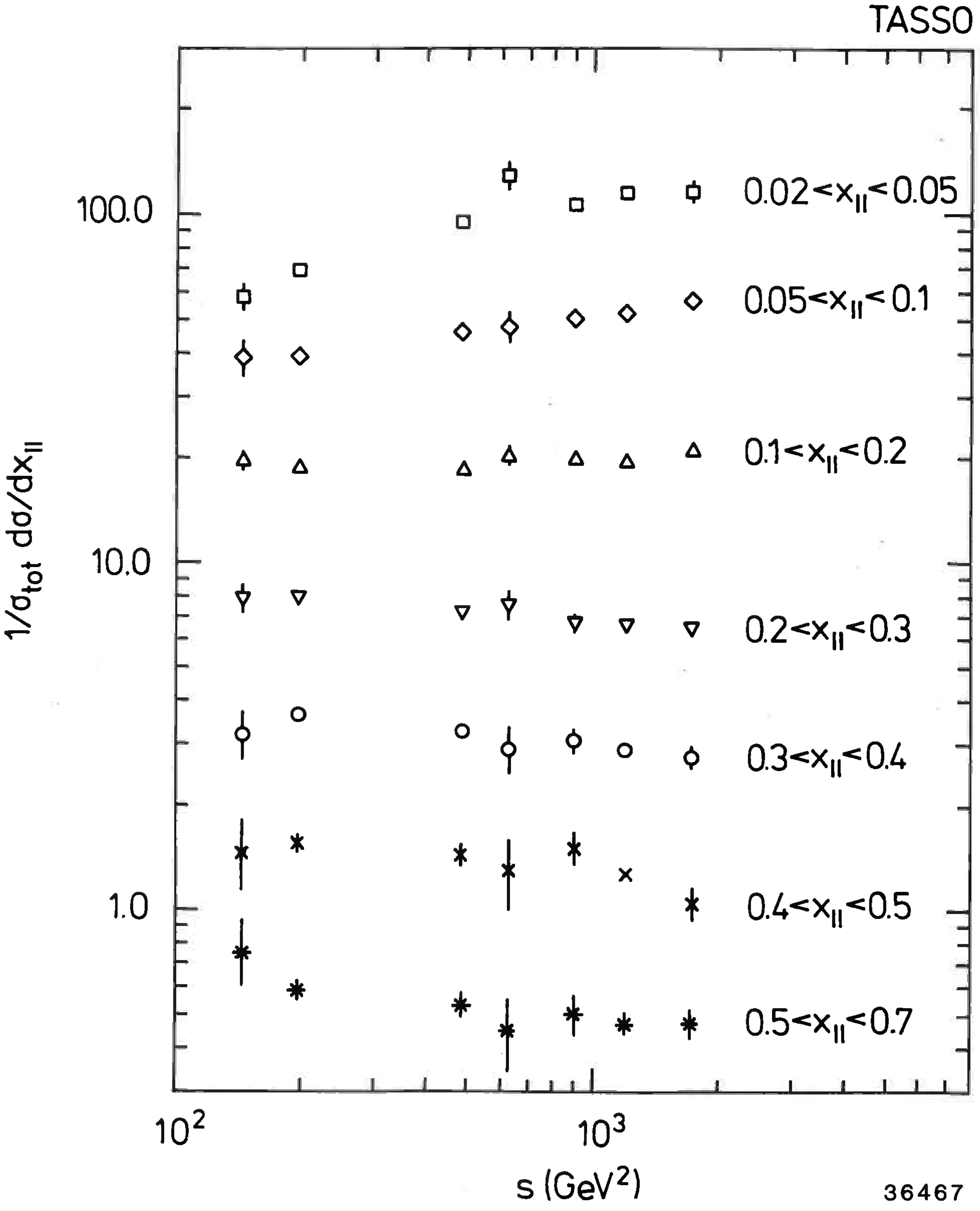
TASSO
100.0
10.0
1.0
$1/\sigma_{tot}\ d\sigma/dx_{\parallel}$
10^2
10^3
s (GeV^2)
$0.02<x_{\parallel}<0.05$
$0.05<x_{\parallel}<0.1$
$0.1<x_{\parallel}<0.2$
$0.2<x_{\parallel}<0.3$
$0.3<x_{\parallel}<0.4$
$0.4<x_{\parallel}<0.5$
$0.5<x_{\parallel}<0.7$
36467

Fig. 41

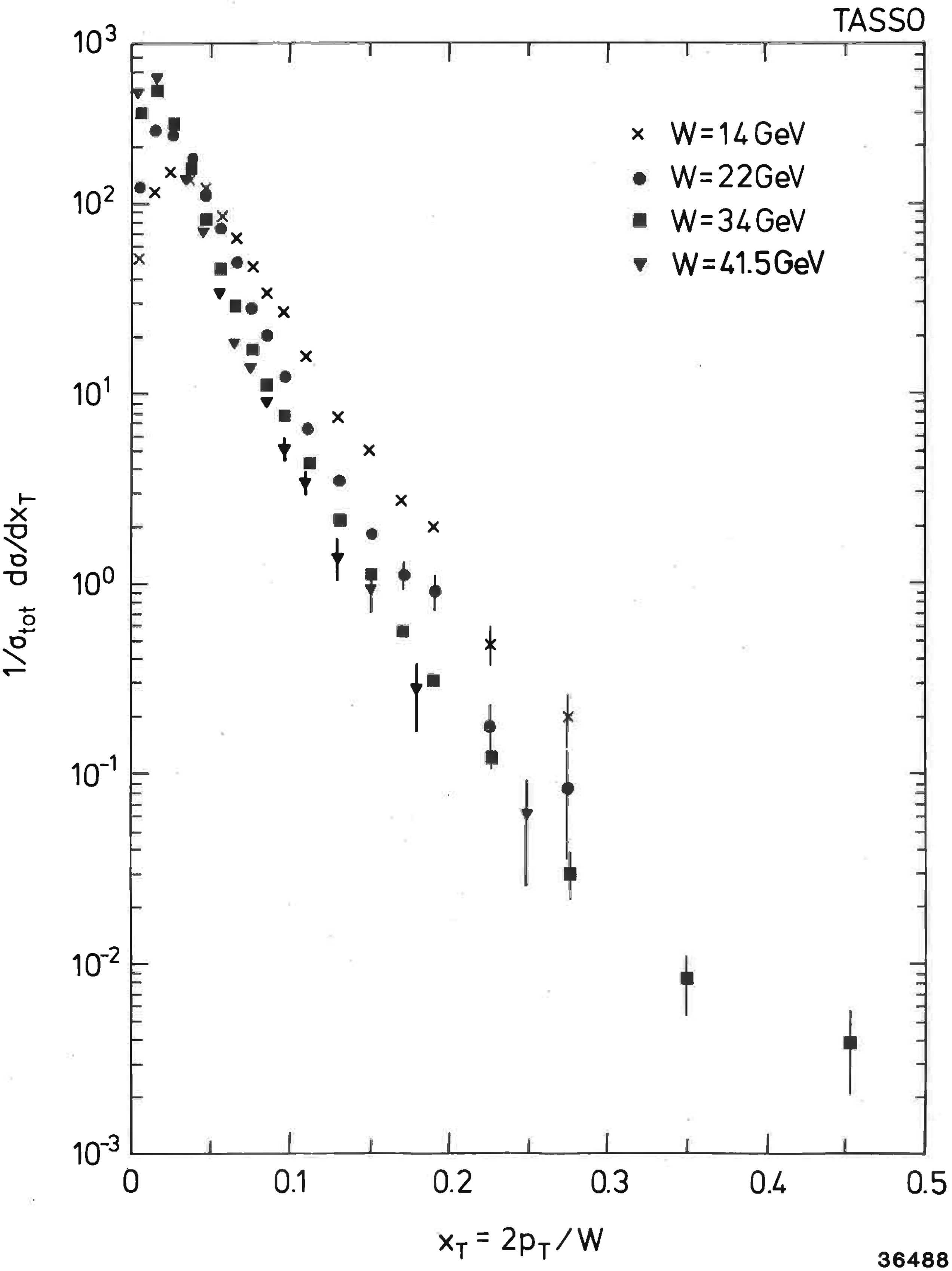
TASSO
× W=14 GeV
● W=22GeV
■ W=34GeV
▼ W=41.5GeV
$1/\sigma_{tot}\ d\sigma/dx_T$
10^3
10^2
10^1
10^0
10^{-1}
10^{-2}
10^{-3}
0
0.1
0.2
0.3
0.4
0.5
$x_T = 2p_T/W$
36488

Fig. 42

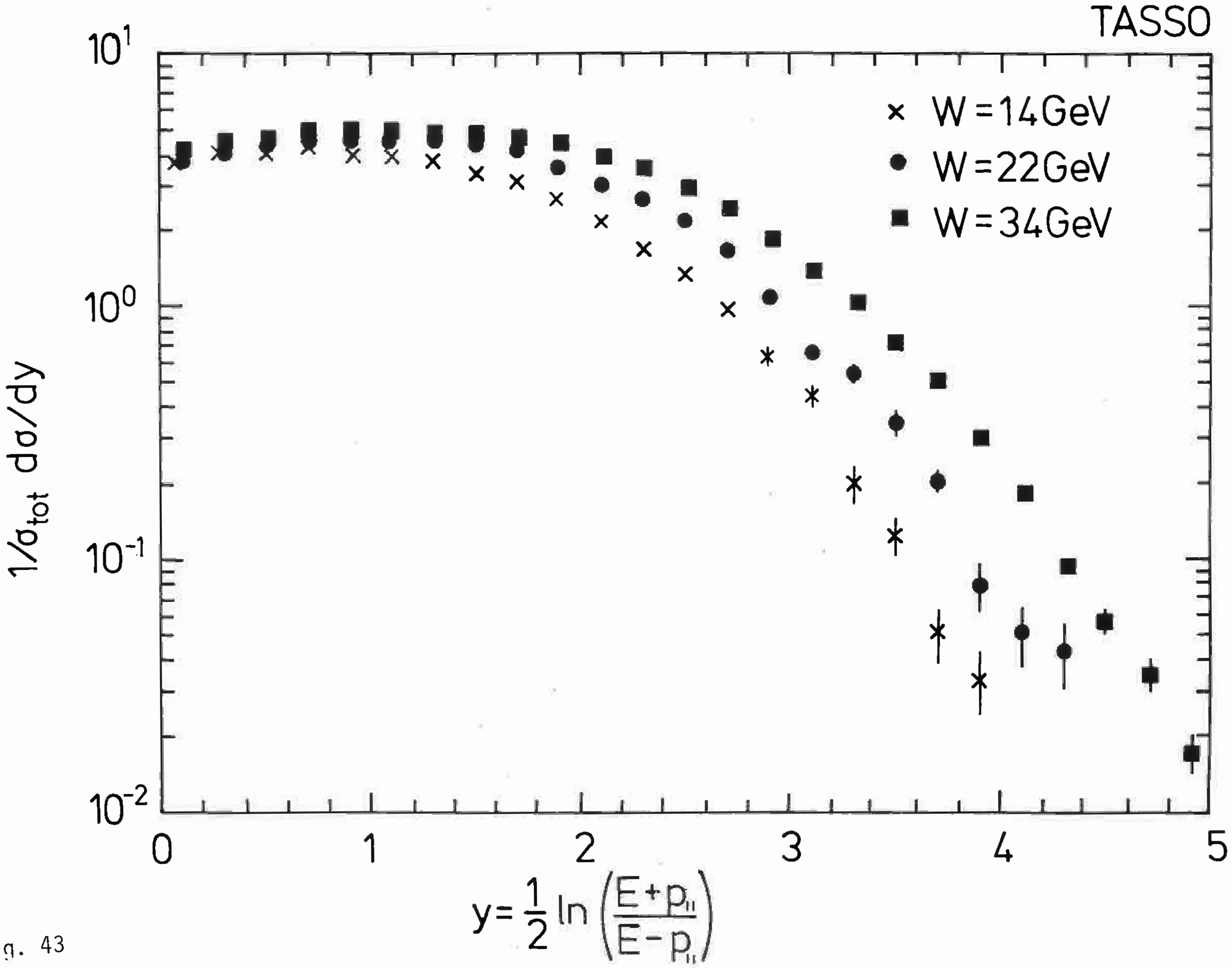
TASSO
× W = 14GeV
● W = 22GeV
■ W = 34GeV
10^1
10^0
10^{-1}
10^{-2}
$1/\sigma_{tot}\ d\sigma/dy$
0
1
2
3
4
5
$y = \frac{1}{2} \ln \left(\frac{E + p_{\parallel}}{E - p_{\parallel}} \right)$

Fig. 43

36691

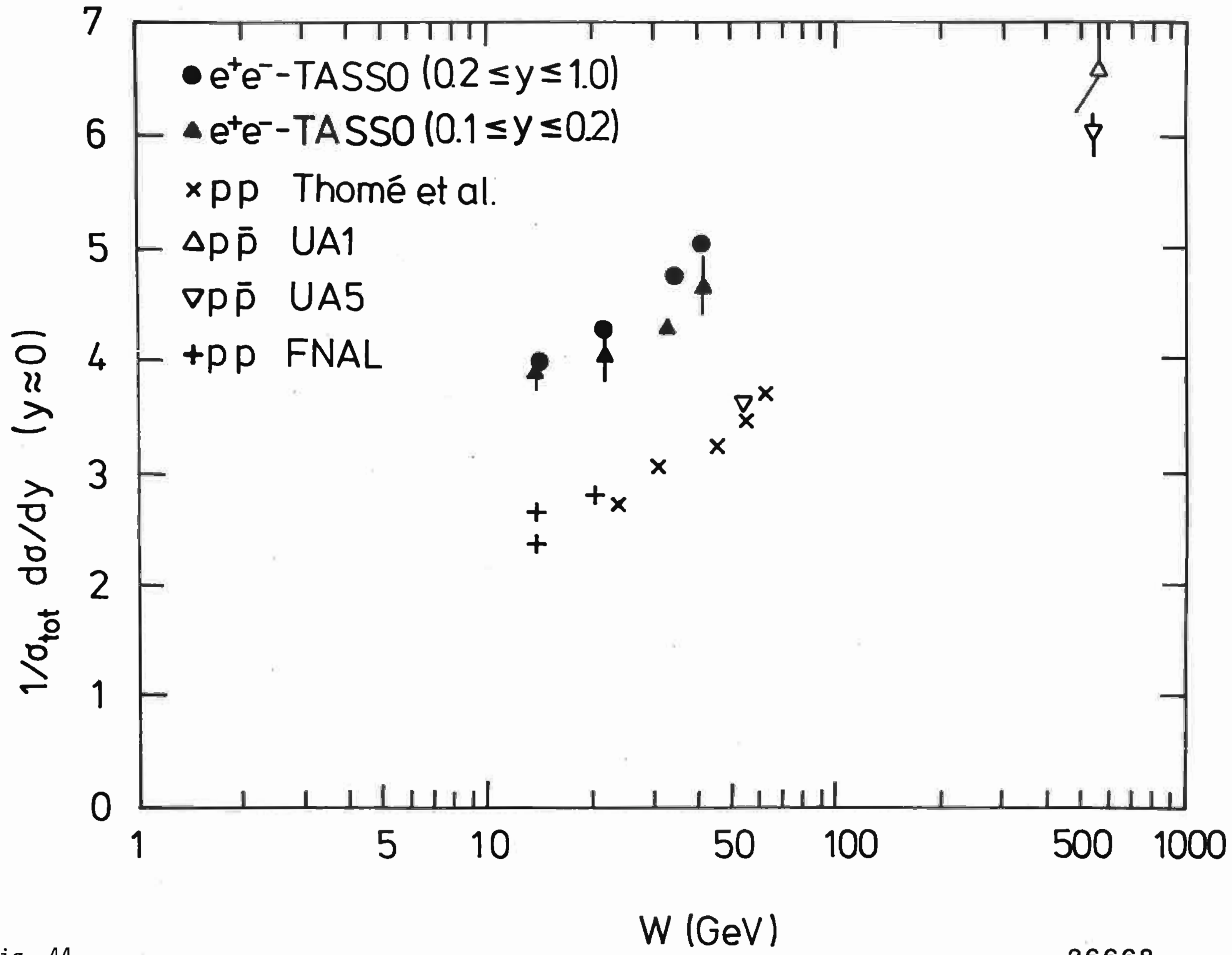

● e⁺e⁻-TASSO (0.2 ≤ y ≤ 1.0)
▲ e⁺e⁻-TASSO (0.1 ≤ y ≤ 0.2)
× p p Thomé et al.
△ p p̄ UA1
▽ p p̄ UA5
+ p p FNAL
$1/\sigma_{tot}\ d\sigma/dy\ (y \approx 0)$
W (GeV)
0
1
2
3
4
5
6
7
1
5
10
50
100
500
1000

Fig. 44

36668

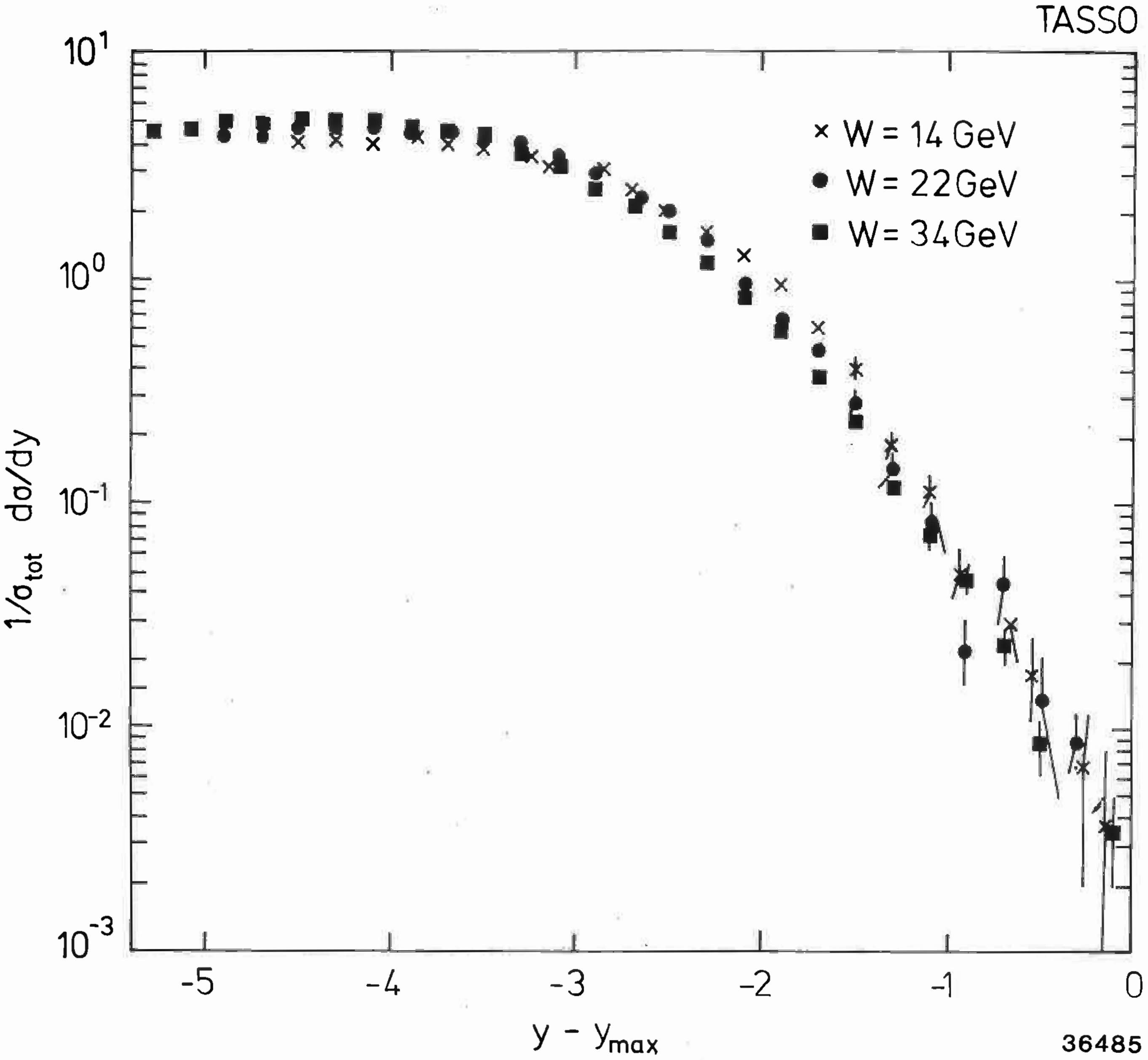
TASSO
× W = 14 GeV
● W = 22GeV
■ W = 34GeV
10^1
10^0
10^{-1}
10^{-2}
10^{-3}
$1/\sigma_{tot}\ d\sigma/dy$
-5
-4
-3
-2
-1
0
$y - y_{max}$
36485

Fig. 45

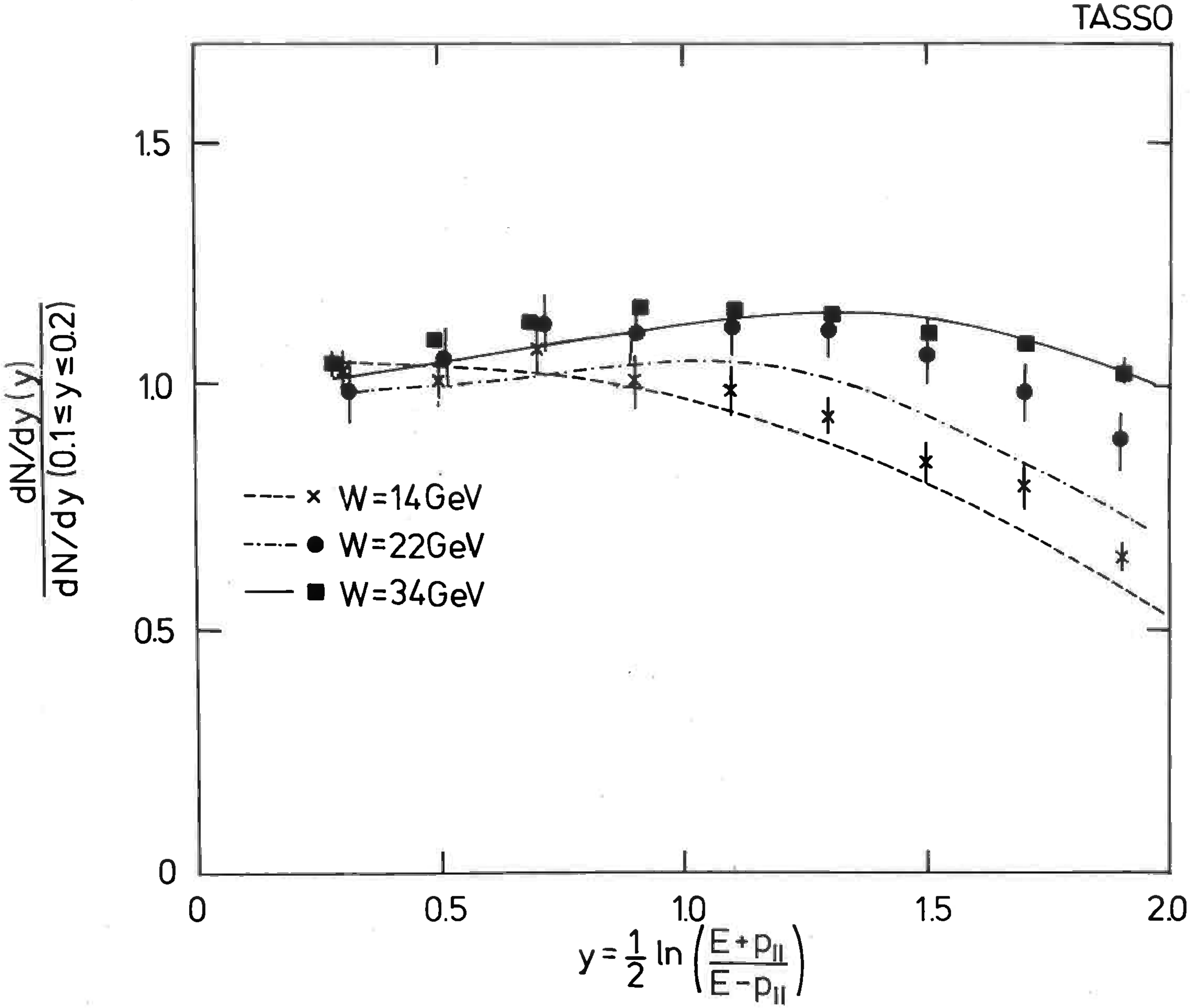

Fig. 46a

36669

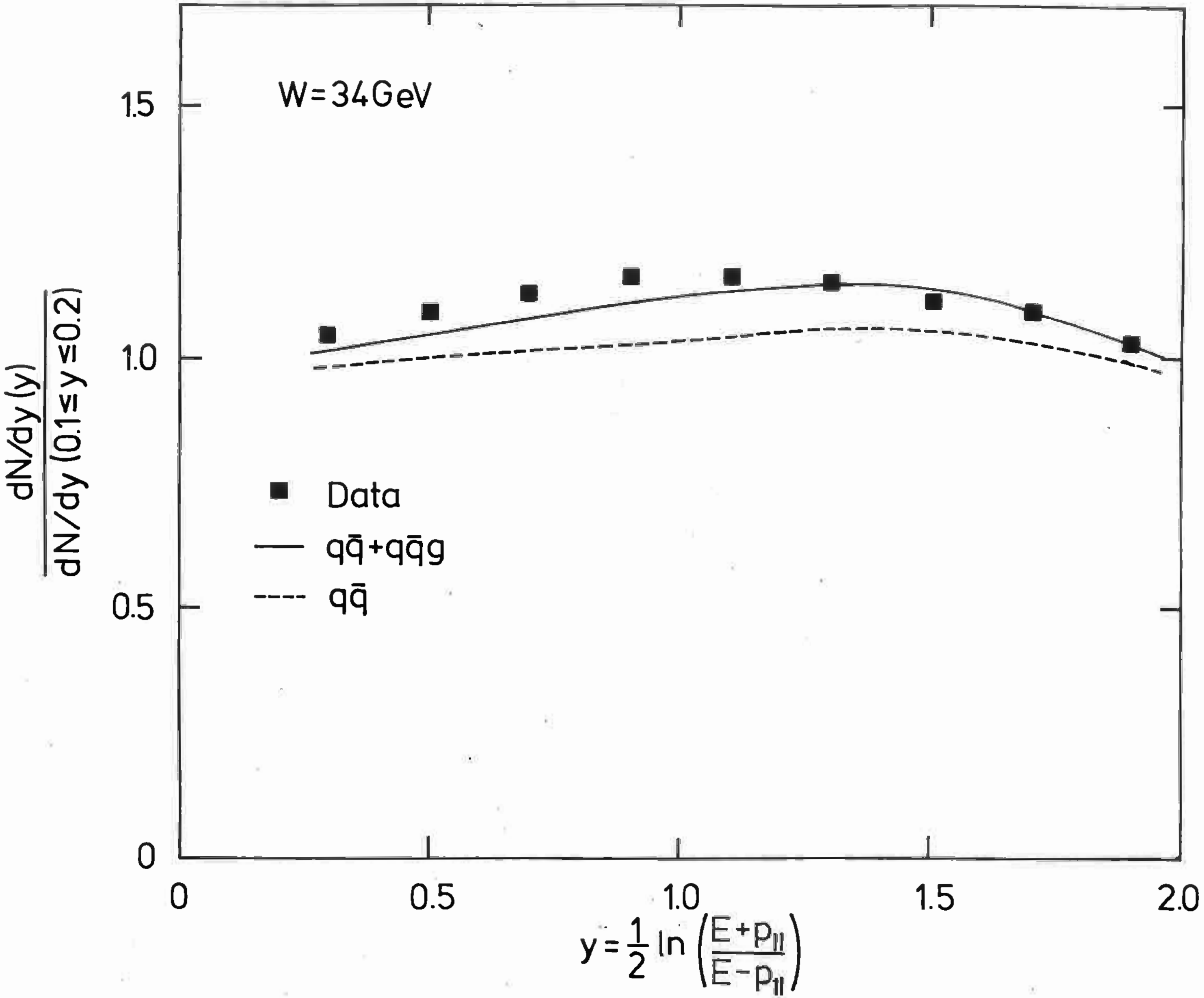
W=34GeV
1.5
1.0
0.5
0
$\frac{dN/dy\,(y)}{dN/dy\,(0.1 \leq y \leq 0.2)}$
■ Data
—— $q\bar{q}+q\bar{q}g$
----- $q\bar{q}$
0
0.5
1.0
1.5
2.0
$y = \frac{1}{2} \ln \left(\frac{E+p_{\parallel}}{E-p_{\parallel}} \right)$
36670

Fig. 46b

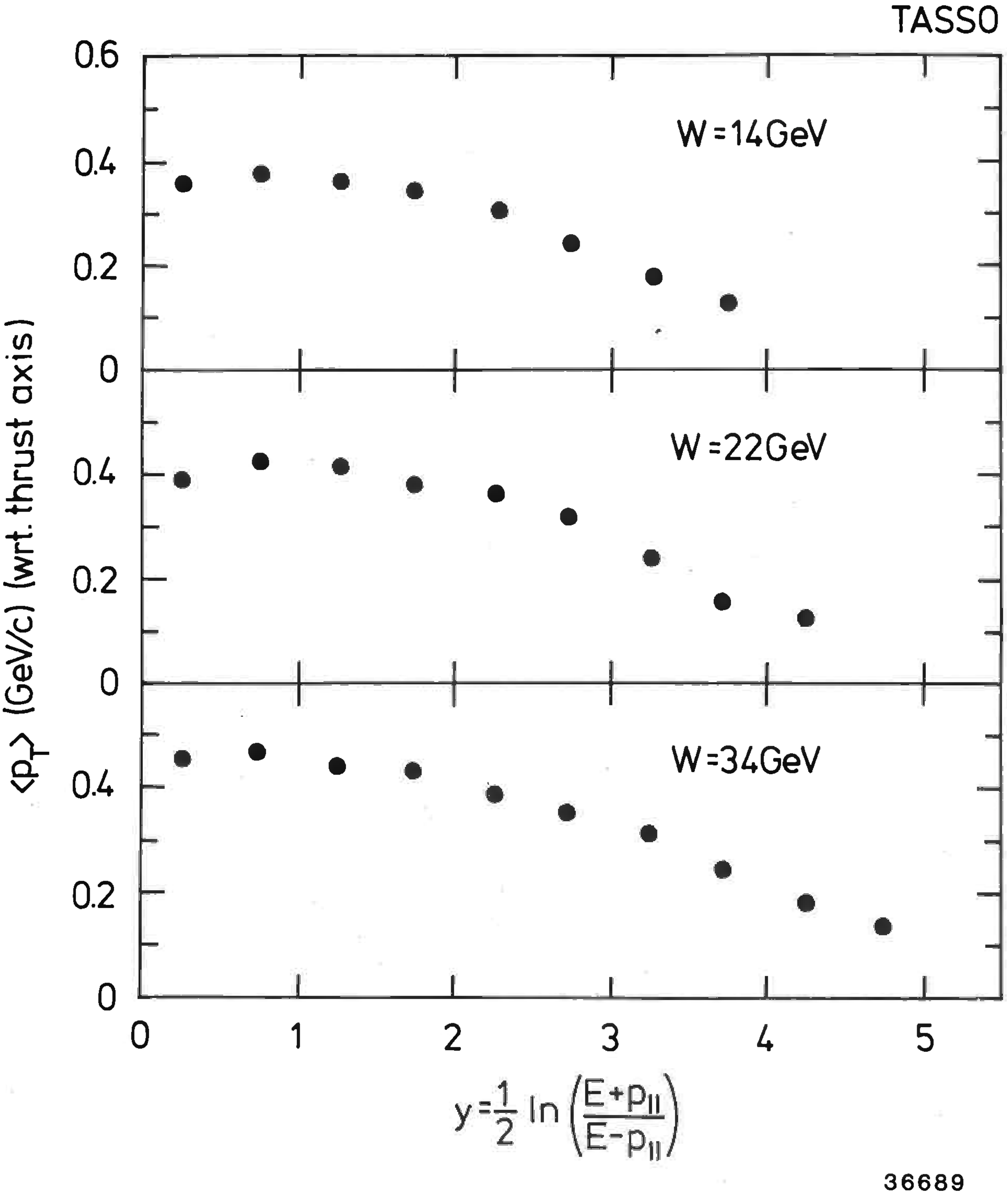
TASSO
W=14GeV
W=22GeV
W=34GeV
0.6
0.4
0.2
0
0.4
0.2
0
0.4
0.2
0
0
1
2
3
4
5
$\langle p_T \rangle$ (GeV/c) (wrt. thrust axis)
$y = \frac{1}{2} \ln \left(\frac{E + p_{\parallel}}{E - p_{\parallel}} \right)$
36689

Fig. 47a

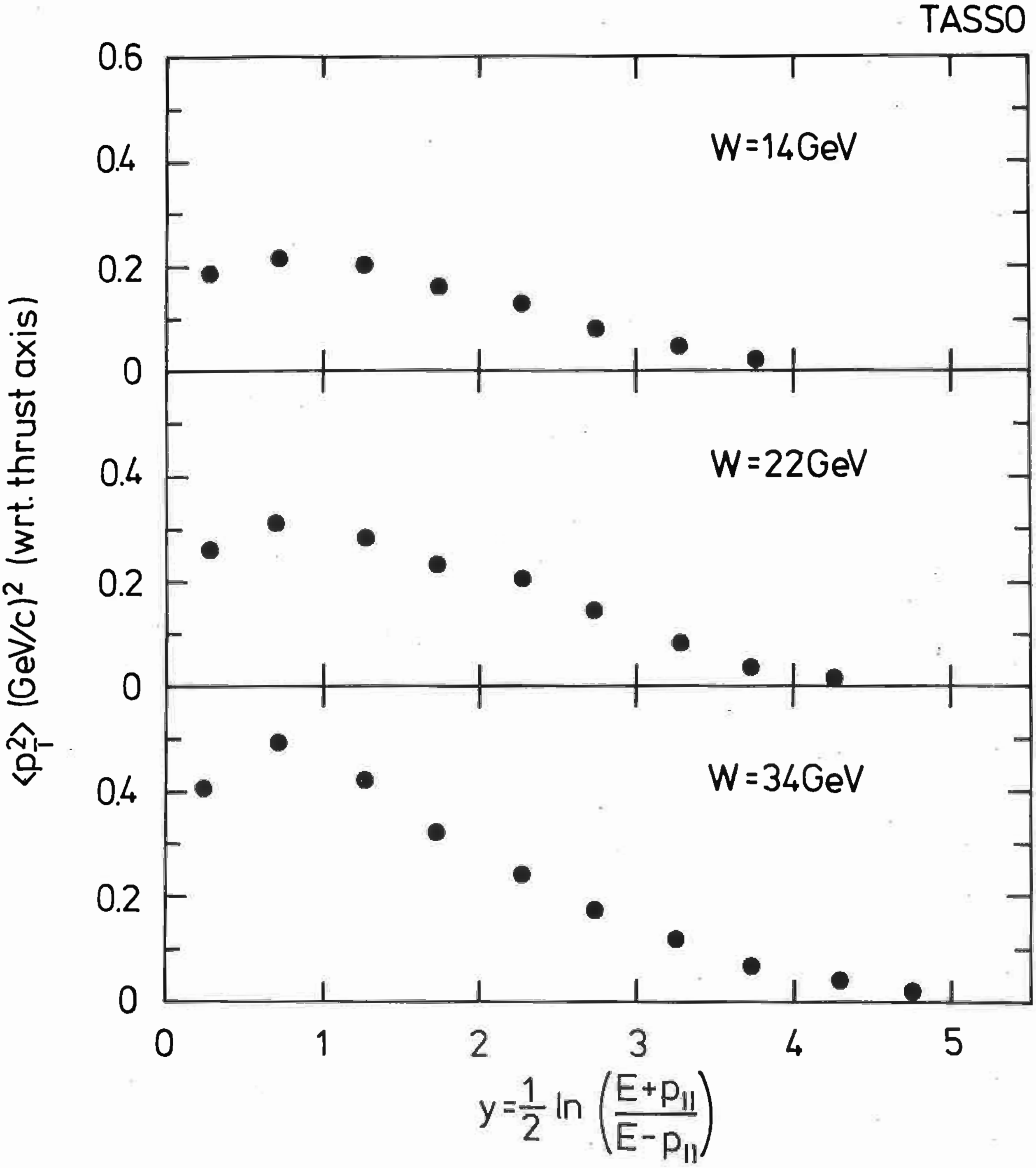
TASSO
W=14GeV
W=22GeV
W=34GeV
0.6
0.4
0.2
0
0.4
0.2
0
0.4
0.2
0
0
1
2
3
4
5
$\langle p_T^2 \rangle$ (GeV/c)^2 (wrt. thrust axis)
$y = \frac{1}{2} \ln \left(\frac{E + p_{\parallel}}{E - p_{\parallel}} \right)$
36682

Fig. 47b

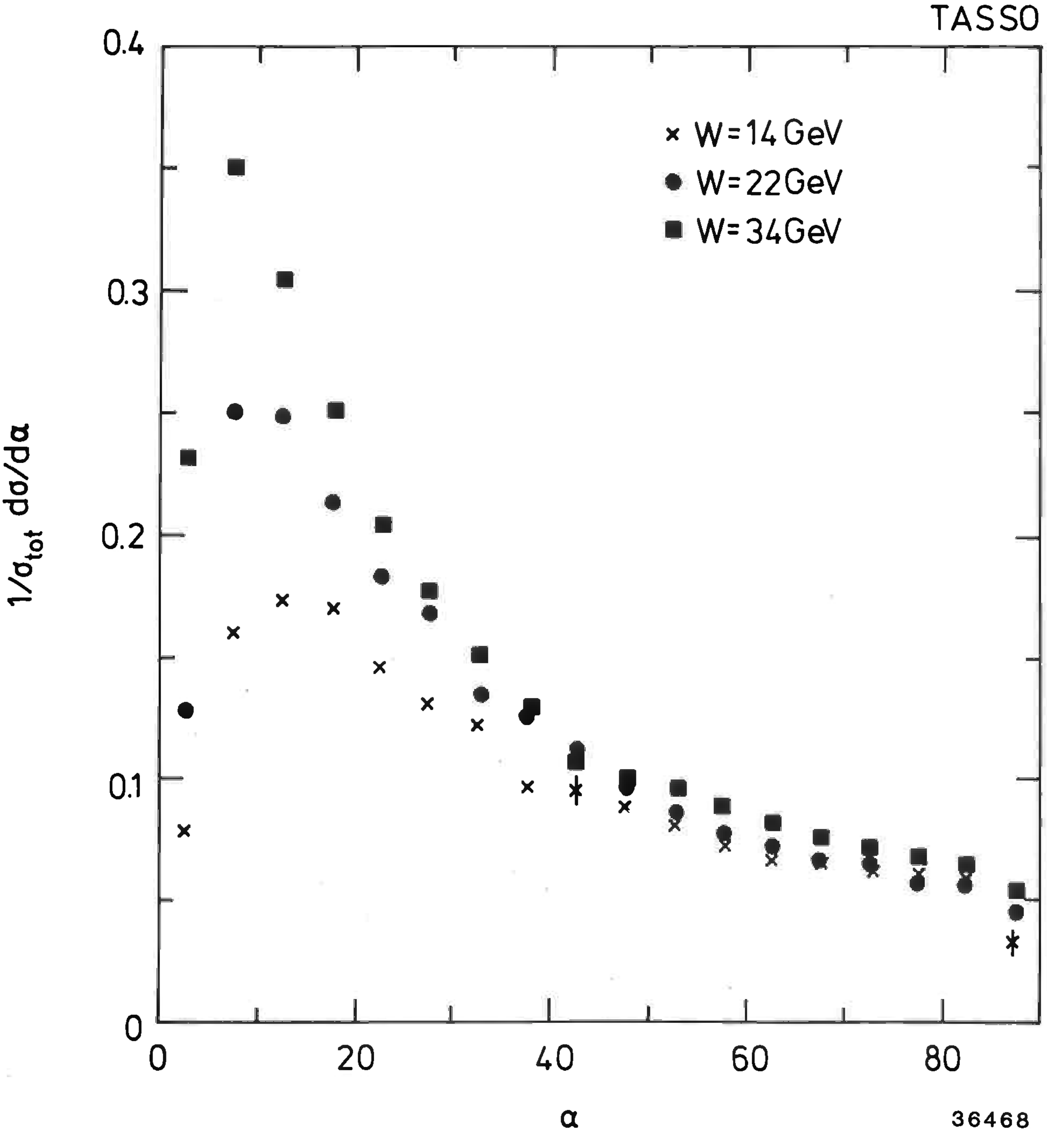
TASSO
× W=14 GeV
● W=22 GeV
■ W=34 GeV
$1/\sigma_{tot}\ d\sigma/d\alpha$
0.4
0.3
0.2
0.1
0
0
20
40
60
80
α
36468

Fig. 48

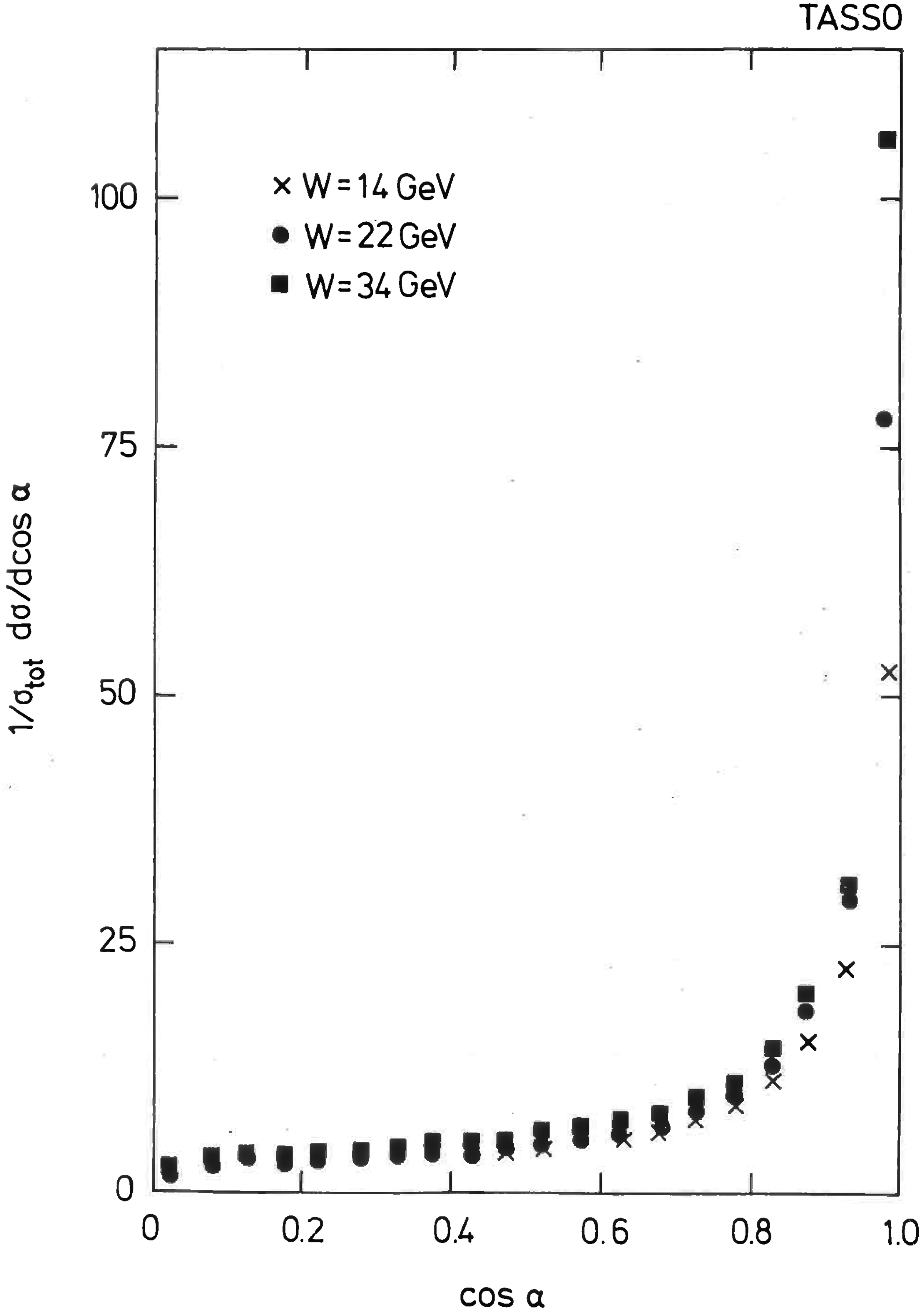
TASSO
× W = 14 GeV
● W = 22 GeV
■ W = 34 GeV
100
75
50
25
0
0
0.2
0.4
0.6
0.8
1.0
1/σ_tot dσ/dcos α
cos α

Fig. 49

36683

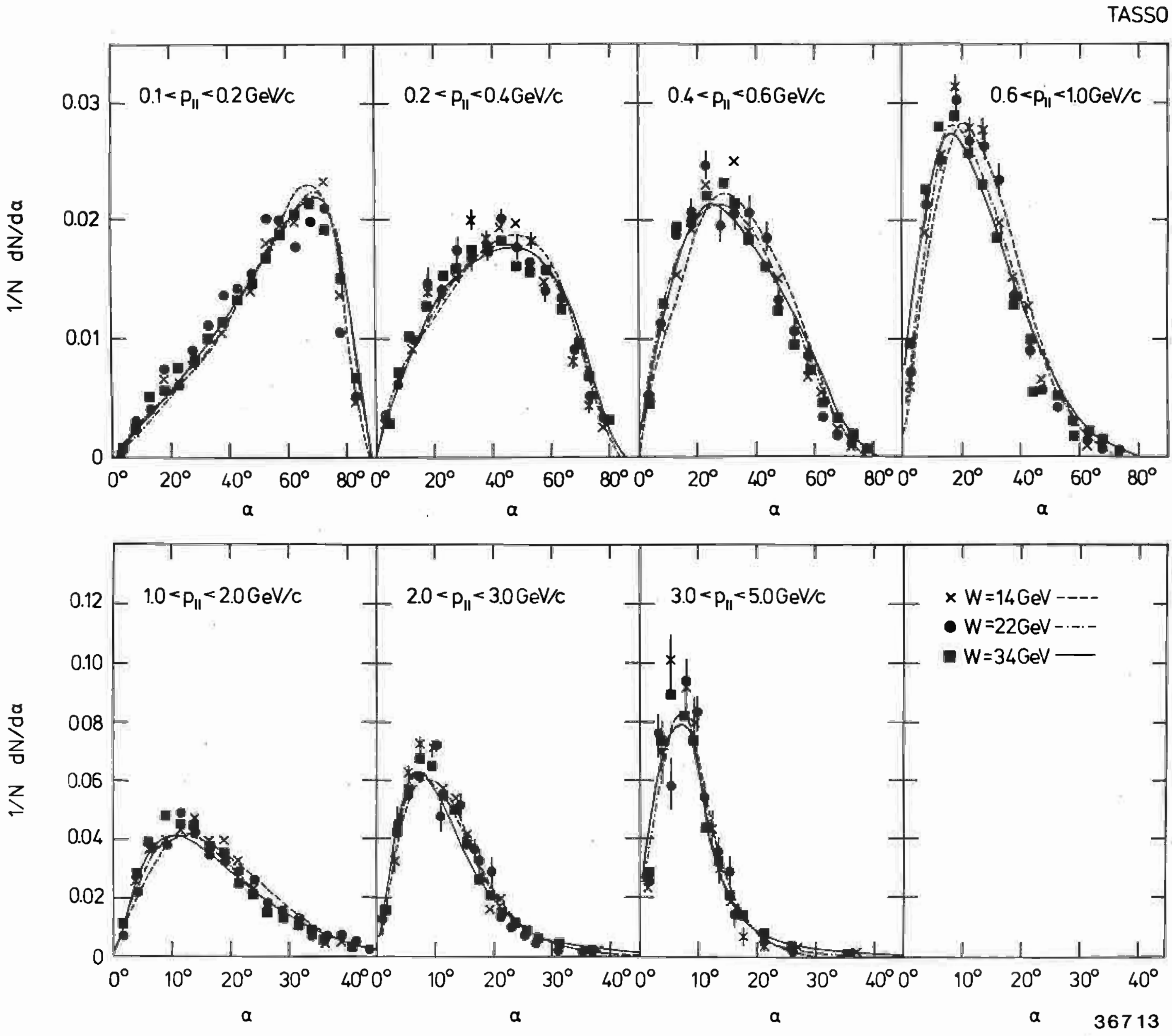
TASSO
0.1 < p_II < 0.2 GeV/c
0.2 < p_II < 0.4 GeV/c
0.4 < p_II < 0.6 GeV/c
0.6 < p_II < 1.0 GeV/c
1.0 < p_II < 2.0 GeV/c
2.0 < p_II < 3.0 GeV/c
3.0 < p_II < 5.0 GeV/c
× W=14 GeV ----
● W=22 GeV -·-·-
■ W=34 GeV ——
1/N dN/dα
0.03
0.02
0.01
0
0.12
0.10
0.08
0.06
0.04
0.02
0°
20°
40°
60°
80°
10°
30°
α
36713

Fig. 50

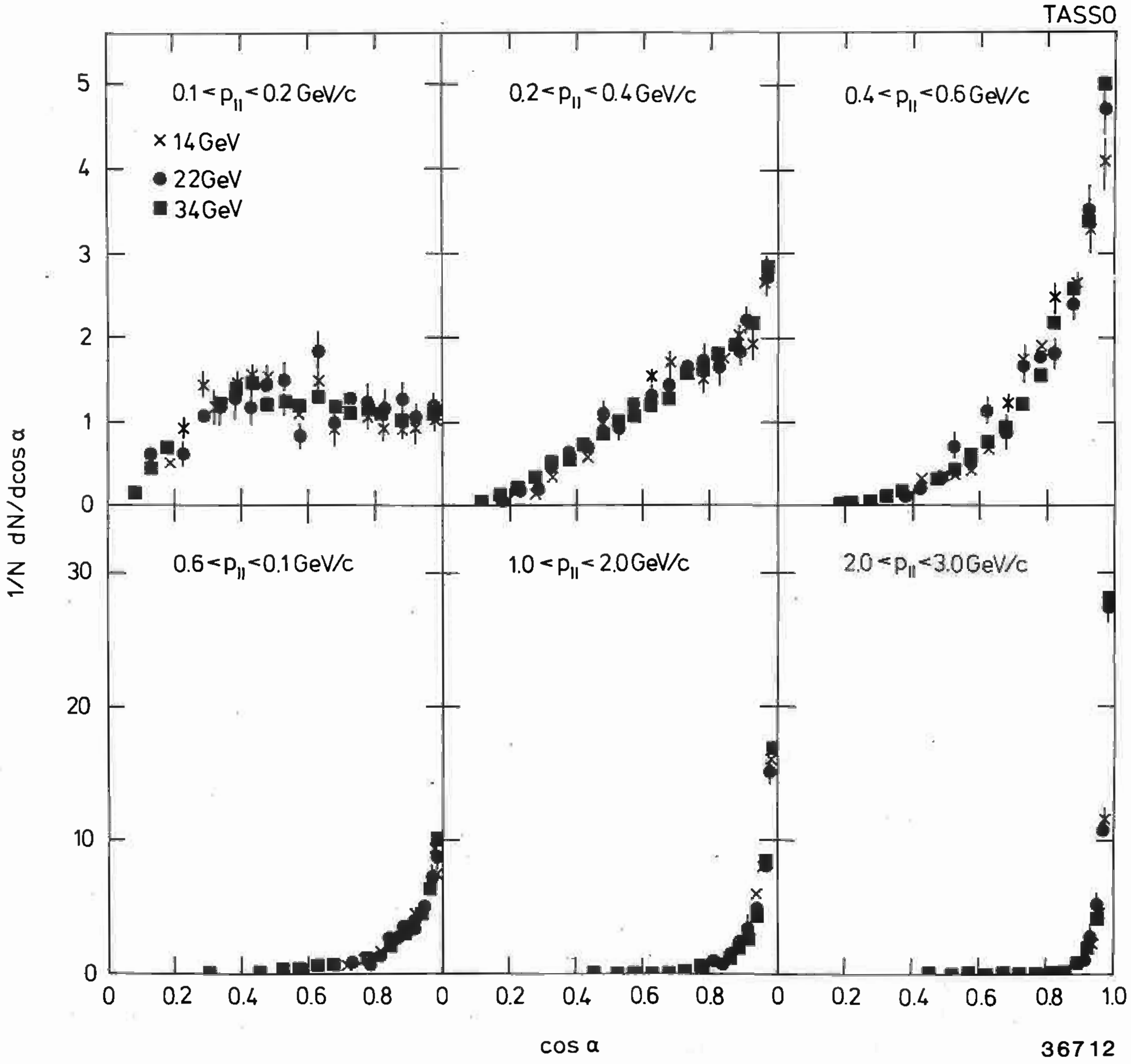
TASSO
0.1 < p∥ < 0.2 GeV/c
× 14 GeV
● 22 GeV
■ 34 GeV
0.2 < p∥ < 0.4 GeV/c
0.4 < p∥ < 0.6 GeV/c
0.6 < p∥ < 0.1 GeV/c
1.0 < p∥ < 2.0 GeV/c
2.0 < p∥ < 3.0 GeV/c
0
1
2
3
4
5
0
10
20
30
1/N dN/dcos α
0
0.2
0.4
0.6
0.8
0
0.2
0.4
0.6
0.8
0
0.2
0.4
0.6
0.8
1.0
cos α
36712

Fig. 51

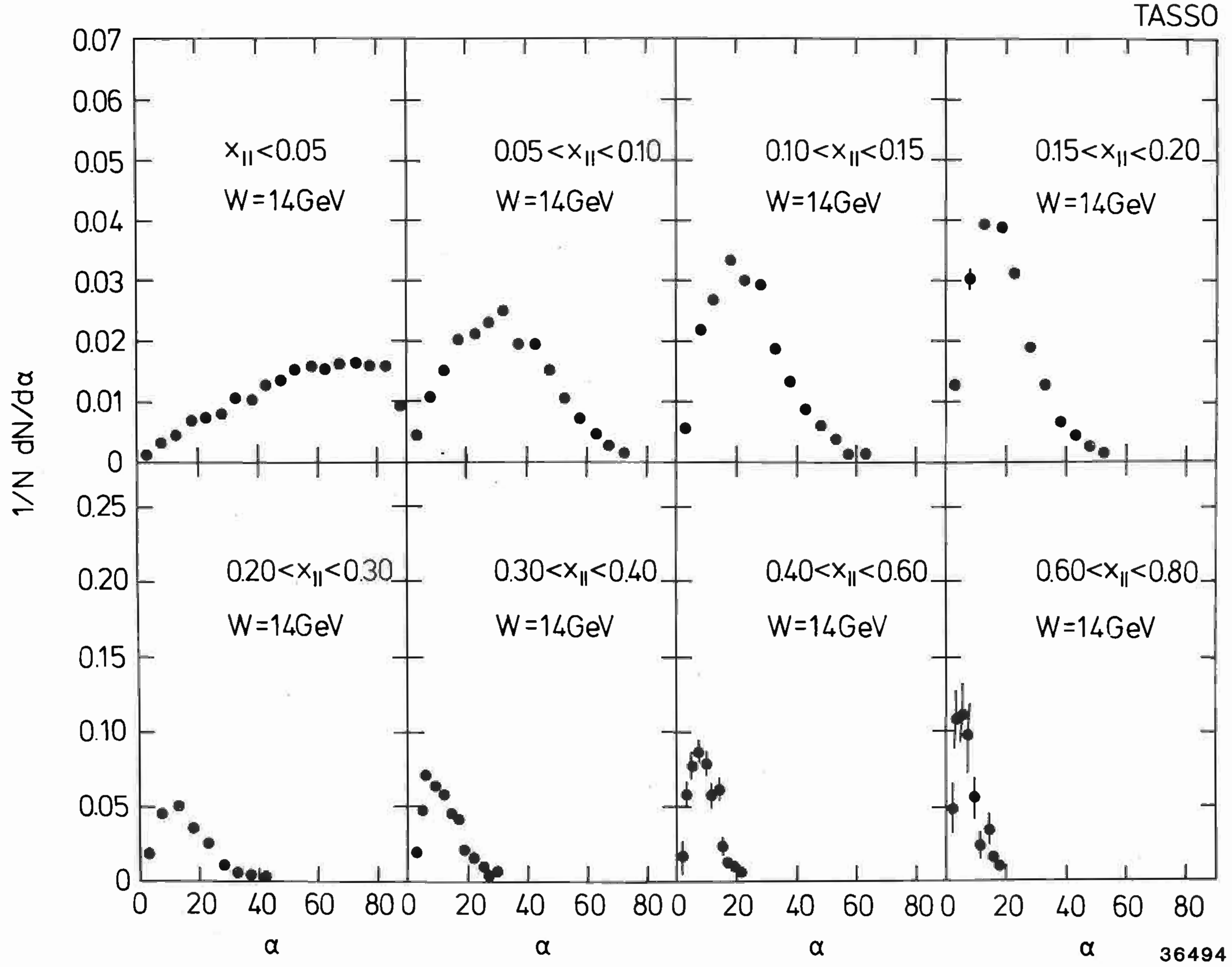
TASSO
1/N dN/dα
0.07
0.06
0.05
0.04
0.03
0.02
0.01
0
$x_{\parallel}<0.05$
W=14GeV
$0.05<x_{\parallel}<0.10$
W=14GeV
$0.10<x_{\parallel}<0.15$
W=14GeV
$0.15<x_{\parallel}<0.20$
W=14GeV
0.25
0.20
0.15
0.10
0.05
0
$0.20<x_{\parallel}<0.30$
W=14GeV
$0.30<x_{\parallel}<0.40$
W=14GeV
$0.40<x_{\parallel}<0.60$
W=14GeV
$0.60<x_{\parallel}<0.80$
W=14GeV
0
20
40
60
80
α
36494

Fig. 52a

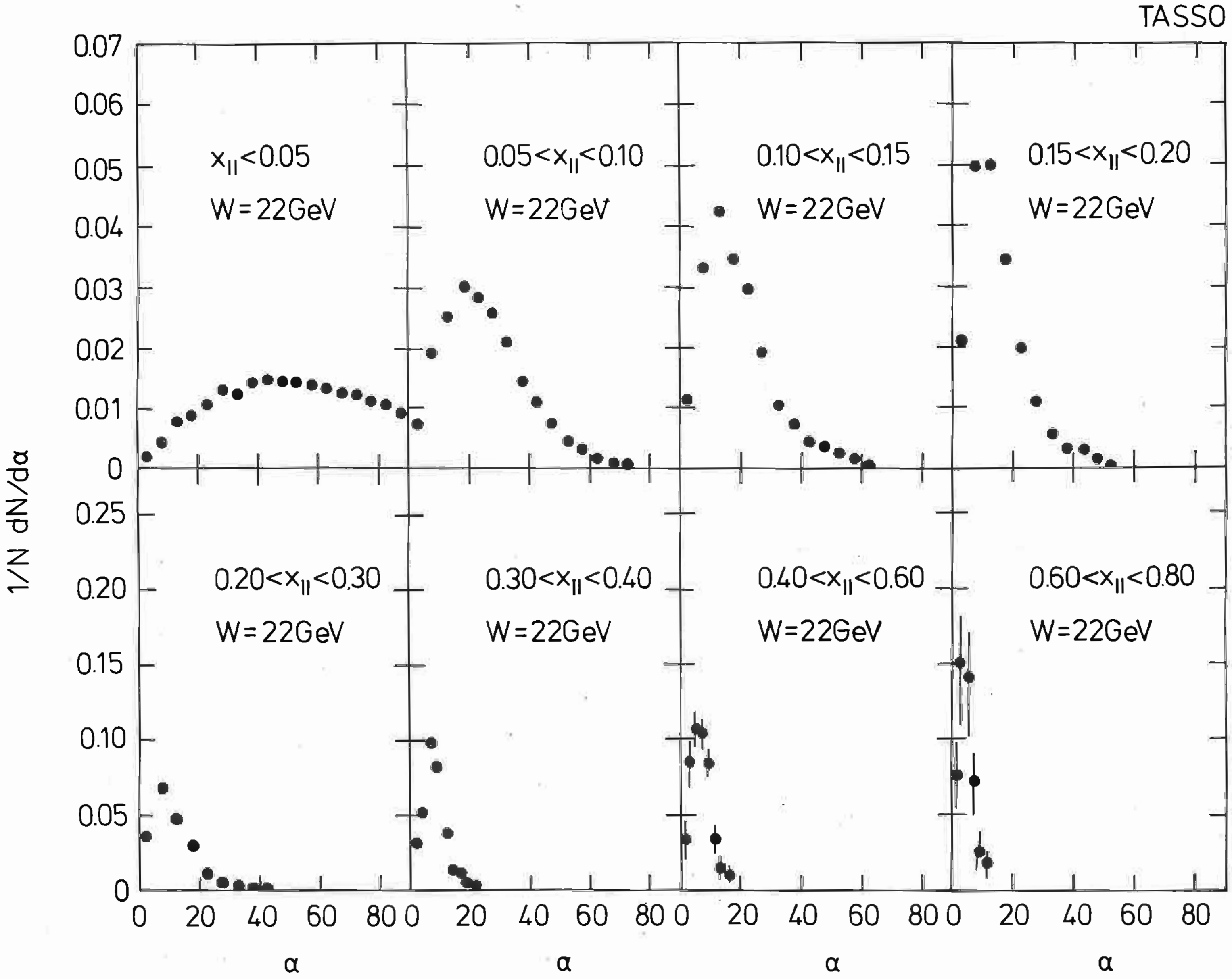

36714

Fig. 52b

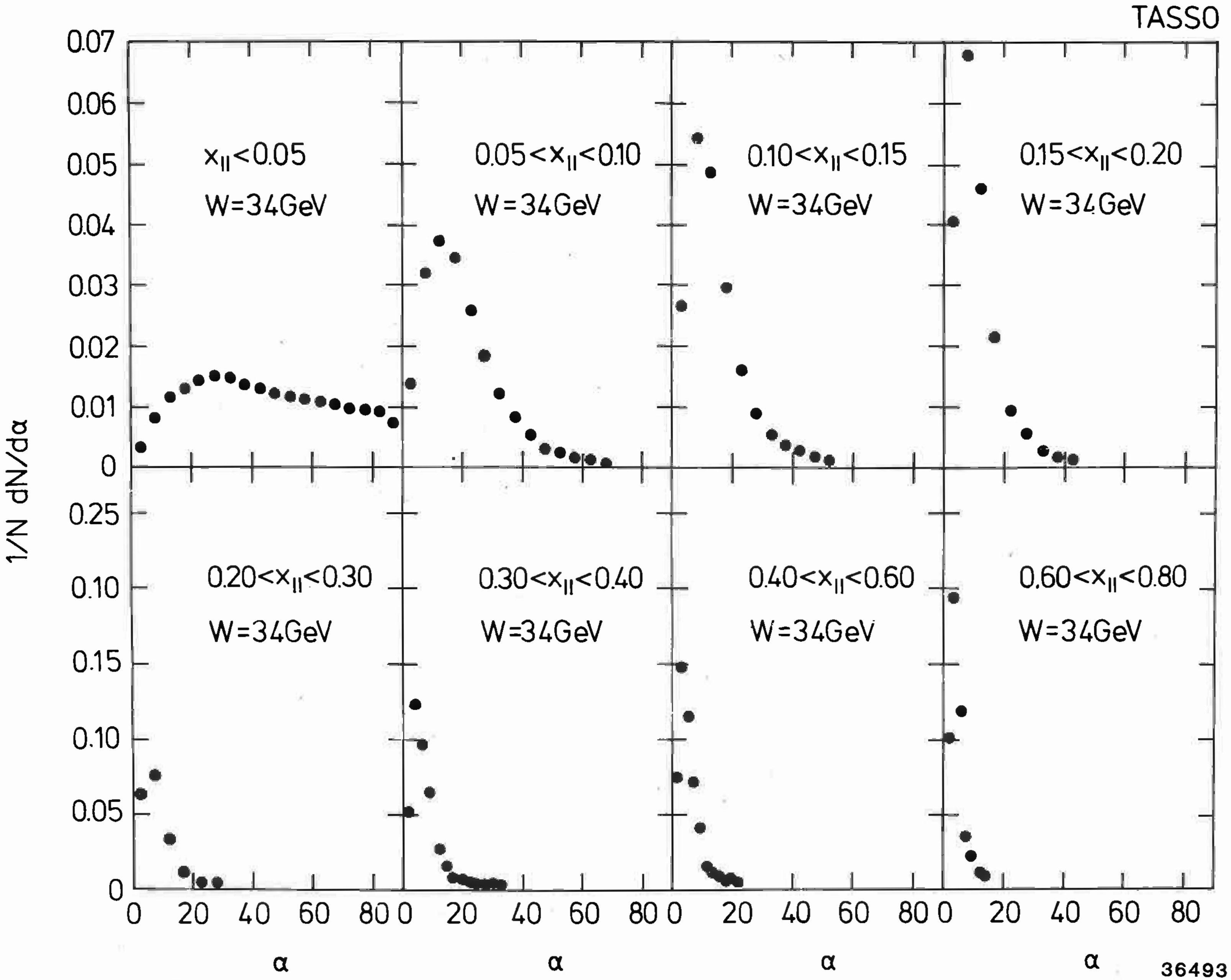
TASSO
1/N dN/dα
0.07
0.06
0.05
0.04
0.03
0.02
0.01
0
0.25
0.10
0.15
0.10
0.05
0
$x_{\|}<0.05$
W=34GeV
$0.05<x_{\|}<0.10$
W=34GeV
$0.10<x_{\|}<0.15$
W=34GeV
$0.15<x_{\|}<0.20$
W=34GeV
$0.20<x_{\|}<0.30$
W=34GeV
$0.30<x_{\|}<0.40$
W=34GeV
$0.40<x_{\|}<0.60$
W=34GeV
$0.60<x_{\|}<0.80$
W=34GeV
0
20
40
60
80
α
36493

Fig. 52c

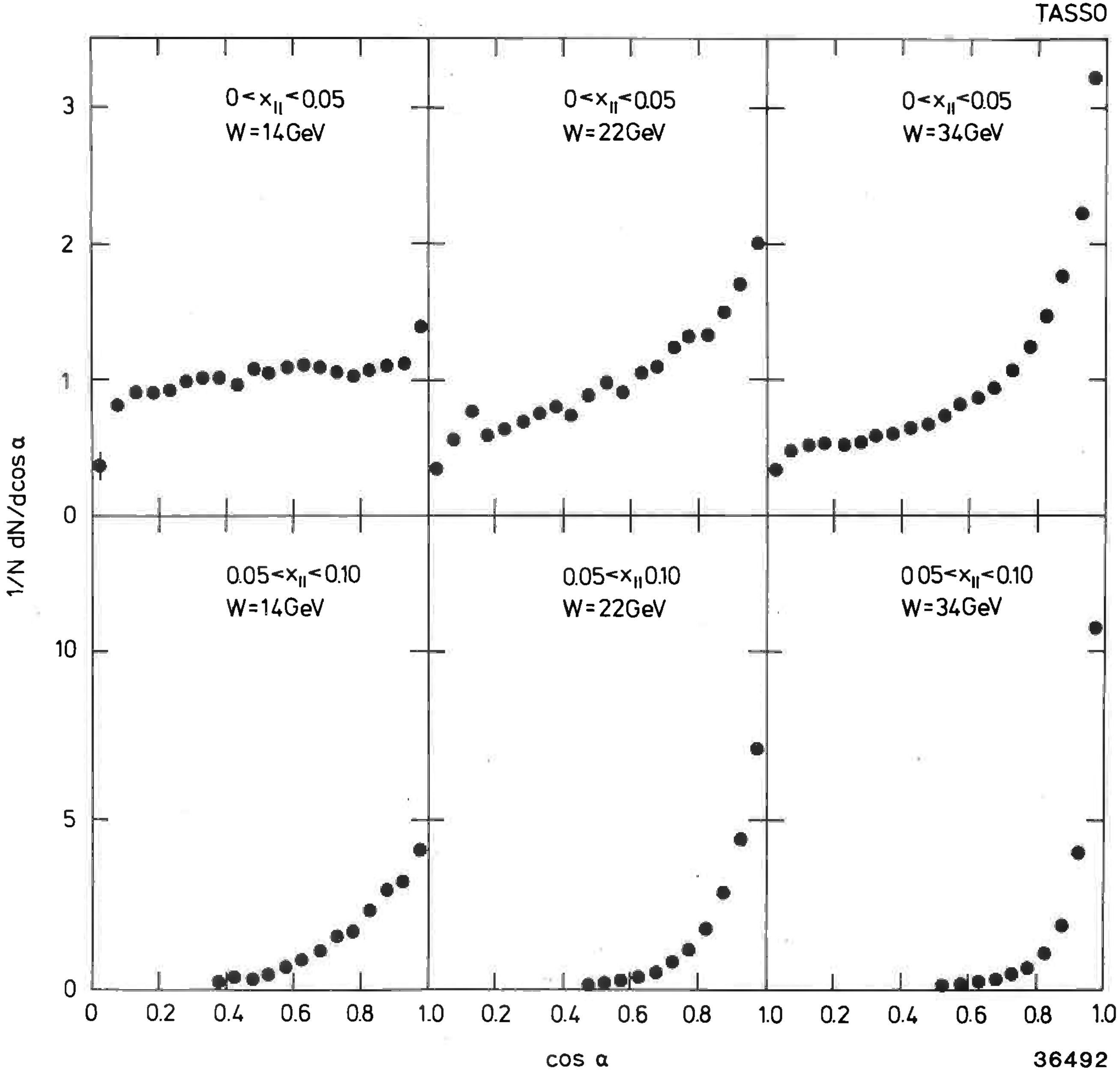
TASSO
0<x_{||}<0.05
W=14GeV
0<x_{||}<0.05
W=22GeV
0<x_{||}<0.05
W=34GeV
0.05<x_{||}<0.10
W=14GeV
0.05<x_{||}0.10
W=22GeV
0 05<x_{||}<0.10
W=34GeV
1/N dN/dcos α
0
1
2
3
0
5
10
0
0.2
0.4
0.6
0.8
1.0
cos α
36492

Fig. 53

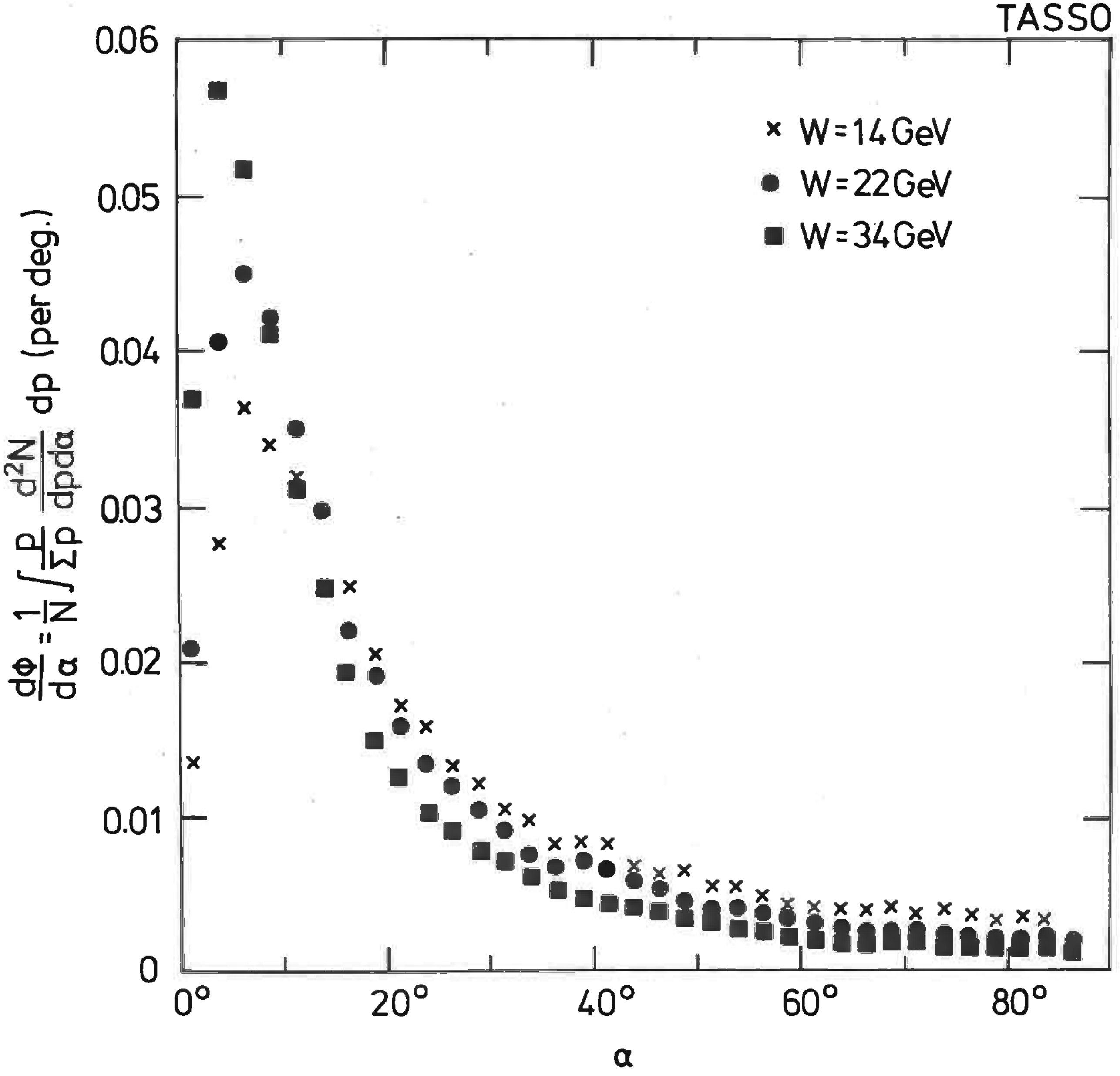
TASSO
× W = 14 GeV
● W = 22 GeV
■ W = 34 GeV
$\frac{d\Phi}{d\alpha} = \frac{1}{N}\int \frac{p}{\Sigma p}\frac{d^2N}{dp\,d\alpha}\,dp$ (per deg.)
0.06
0.05
0.04
0.03
0.02
0.01
0
0°
20°
40°
60°
80°
α

Fig. 54

36677

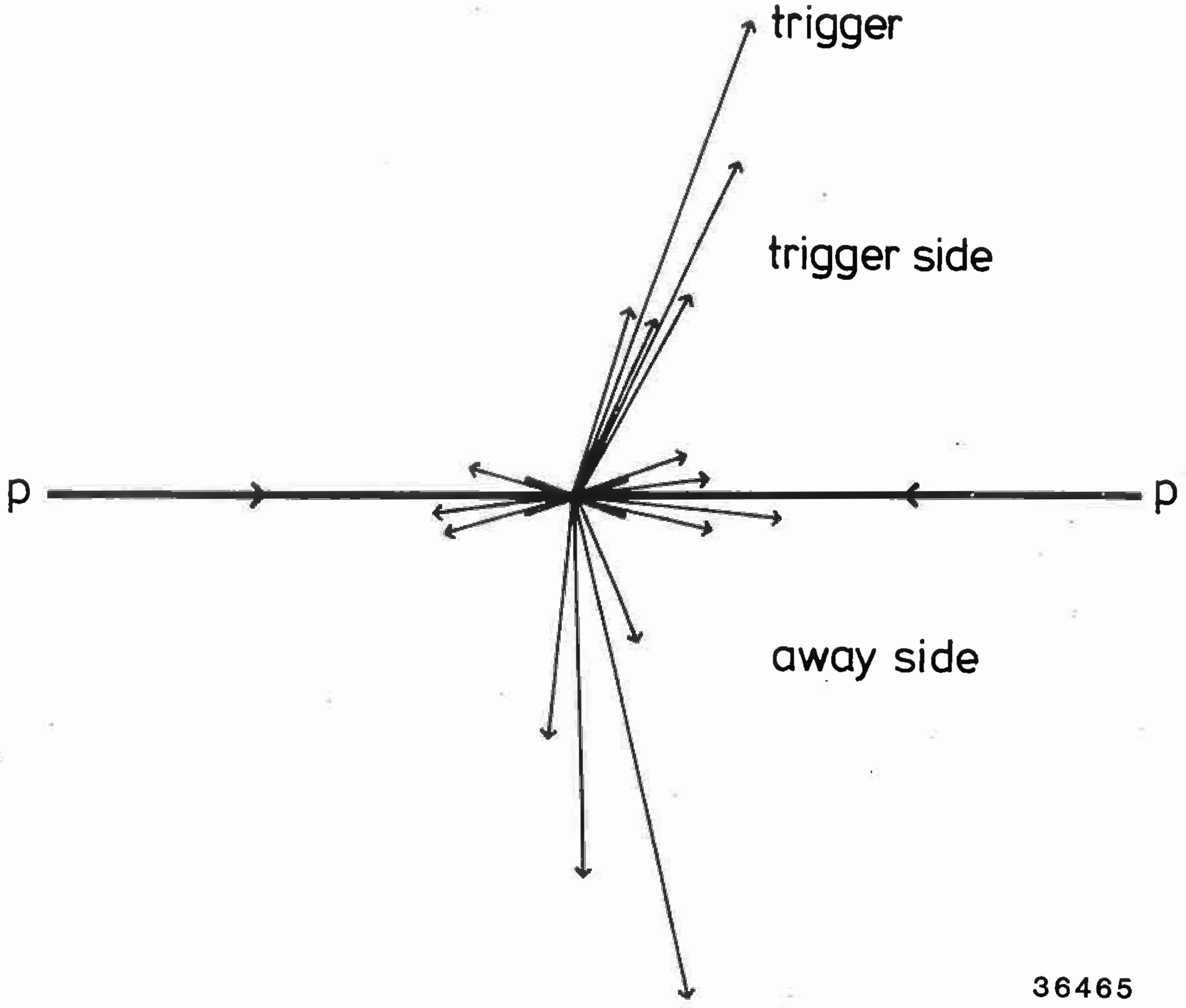

Fig. 55

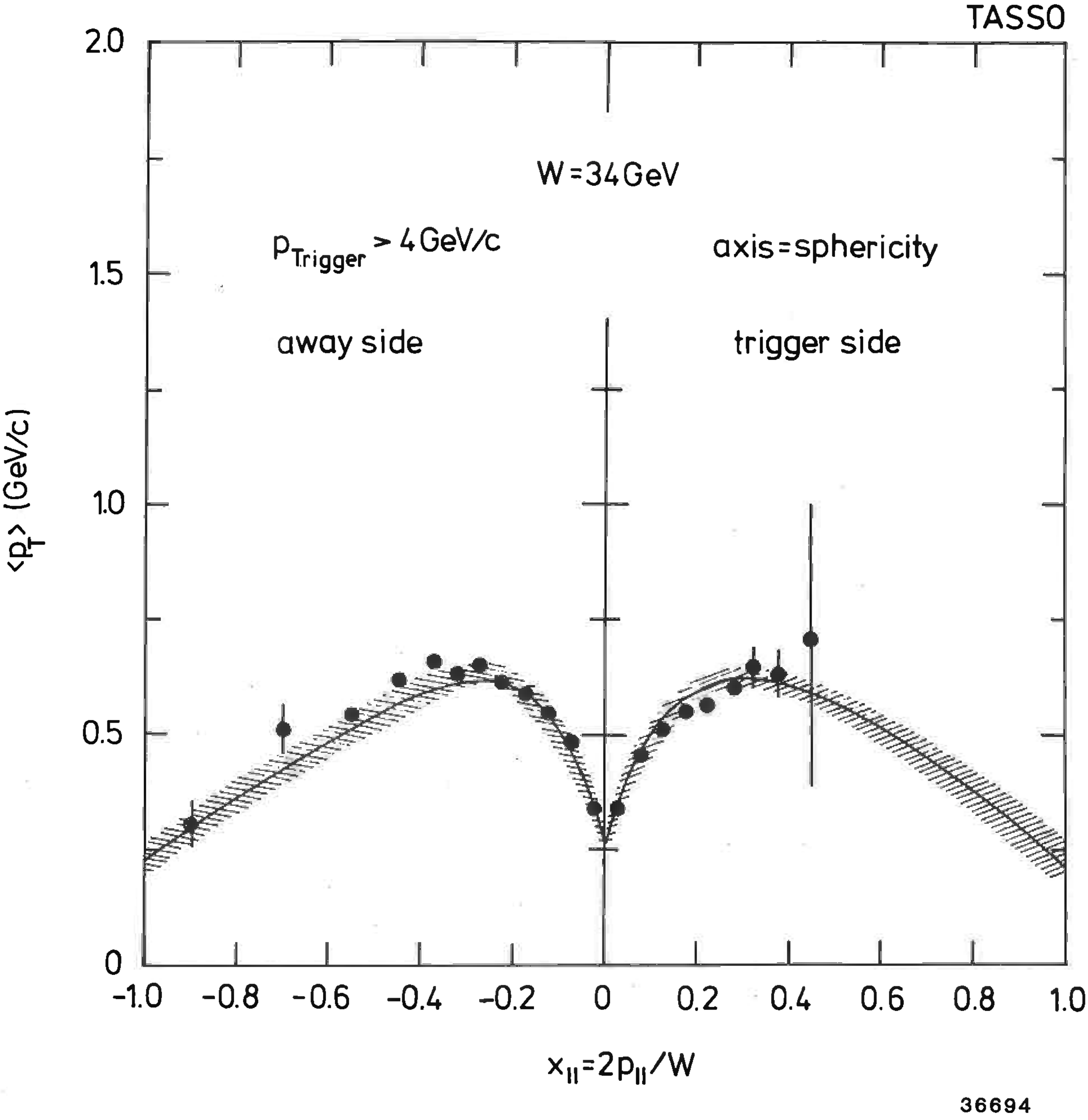
TASSO
W=34GeV
$p_{Trigger}$ > 4GeV/c
axis=sphericity
away side
trigger side
<p_T> (GeV/c)
2.0
1.5
1.0
0.5
0
-1.0
-0.8
-0.6
-0.4
-0.2
0
0.2
0.4
0.6
0.8
1.0
$x_{\parallel}=2p_{\parallel}/W$
36694

Fig. 56

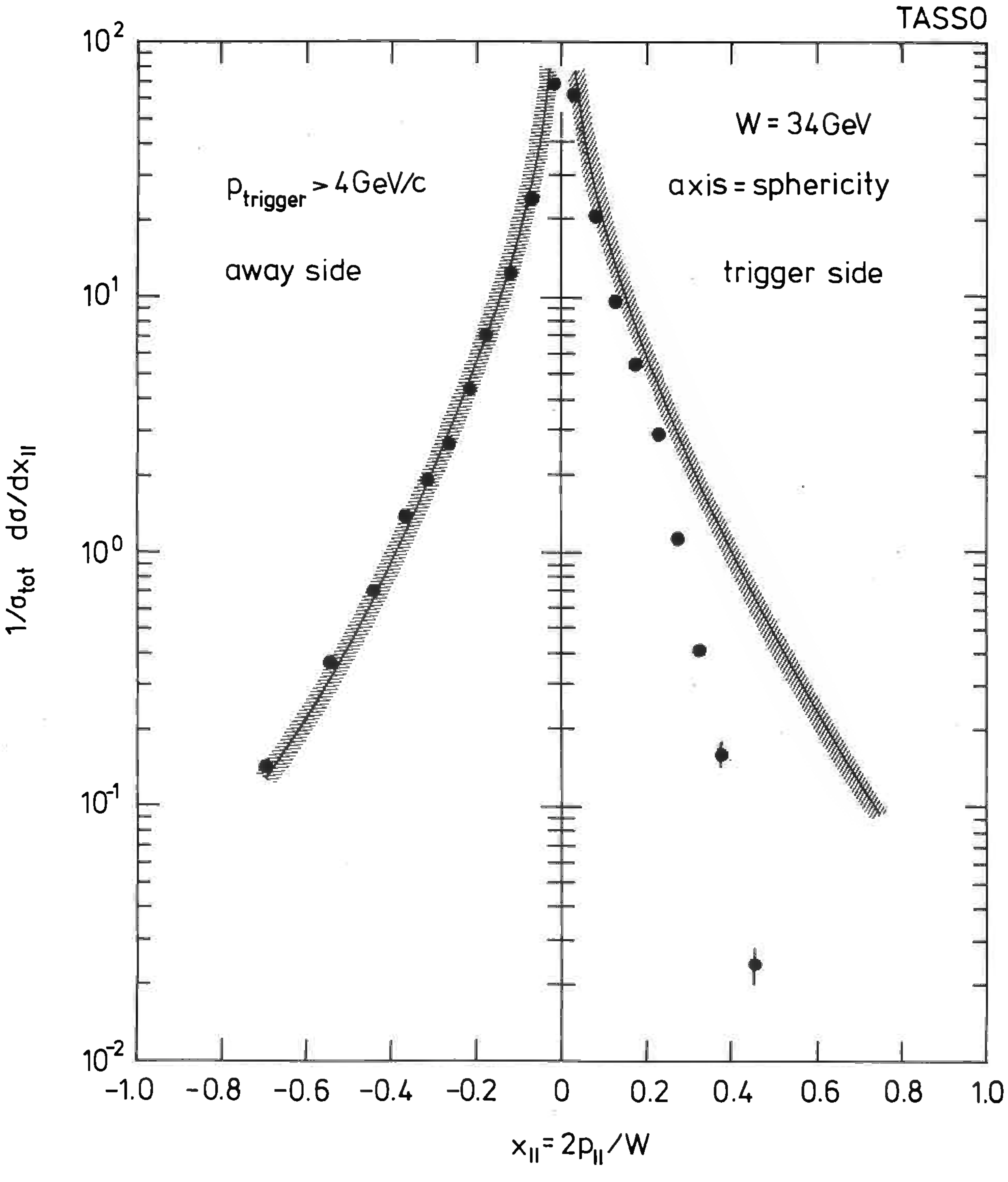
TASSO
10^2
10^1
10^0
10^{-1}
10^{-2}
$1/\sigma_{tot}\ d\sigma/dx_{\parallel}$
$p_{trigger} > 4$ GeV/c
away side
W = 34GeV
axis = sphericity
trigger side
-1.0
-0.8
-0.6
-0.4
-0.2
0
0.2
0.4
0.6
0.8
1.0
$x_{\parallel} = 2p_{\parallel}/W$
36697

Fig. 57

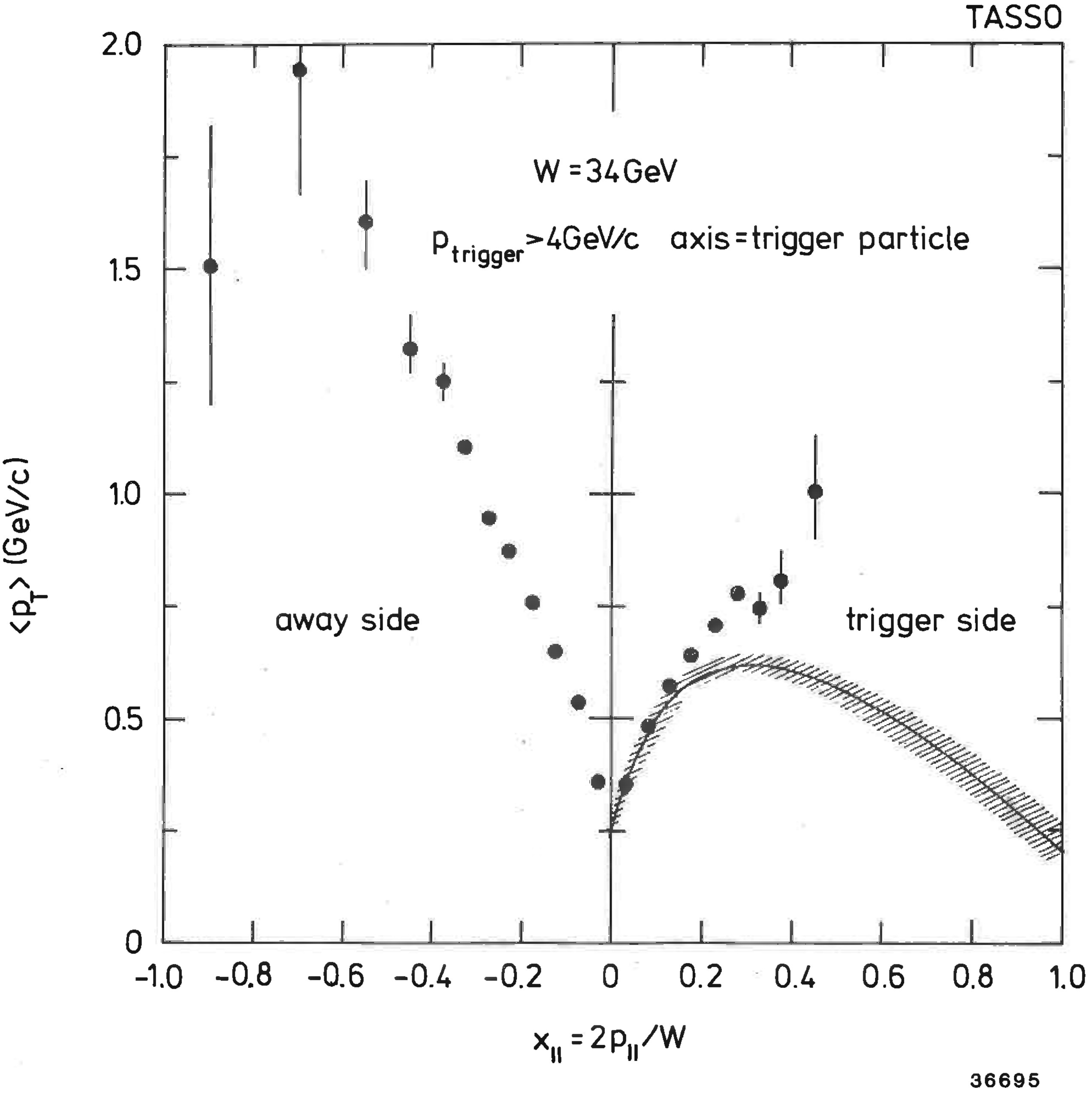
TASSO
W = 34 GeV
$p_{trigger}$ > 4 GeV/c
axis = trigger particle
away side
trigger side
$\langle p_T \rangle$ (GeV/c)
$x_{\parallel} = 2p_{\parallel}/W$
2.0
1.5
1.0
0.5
0
-1.0
-0.8
-0.6
-0.4
-0.2
0
0.2
0.4
0.6
0.8
1.0
36695

Fig. 58

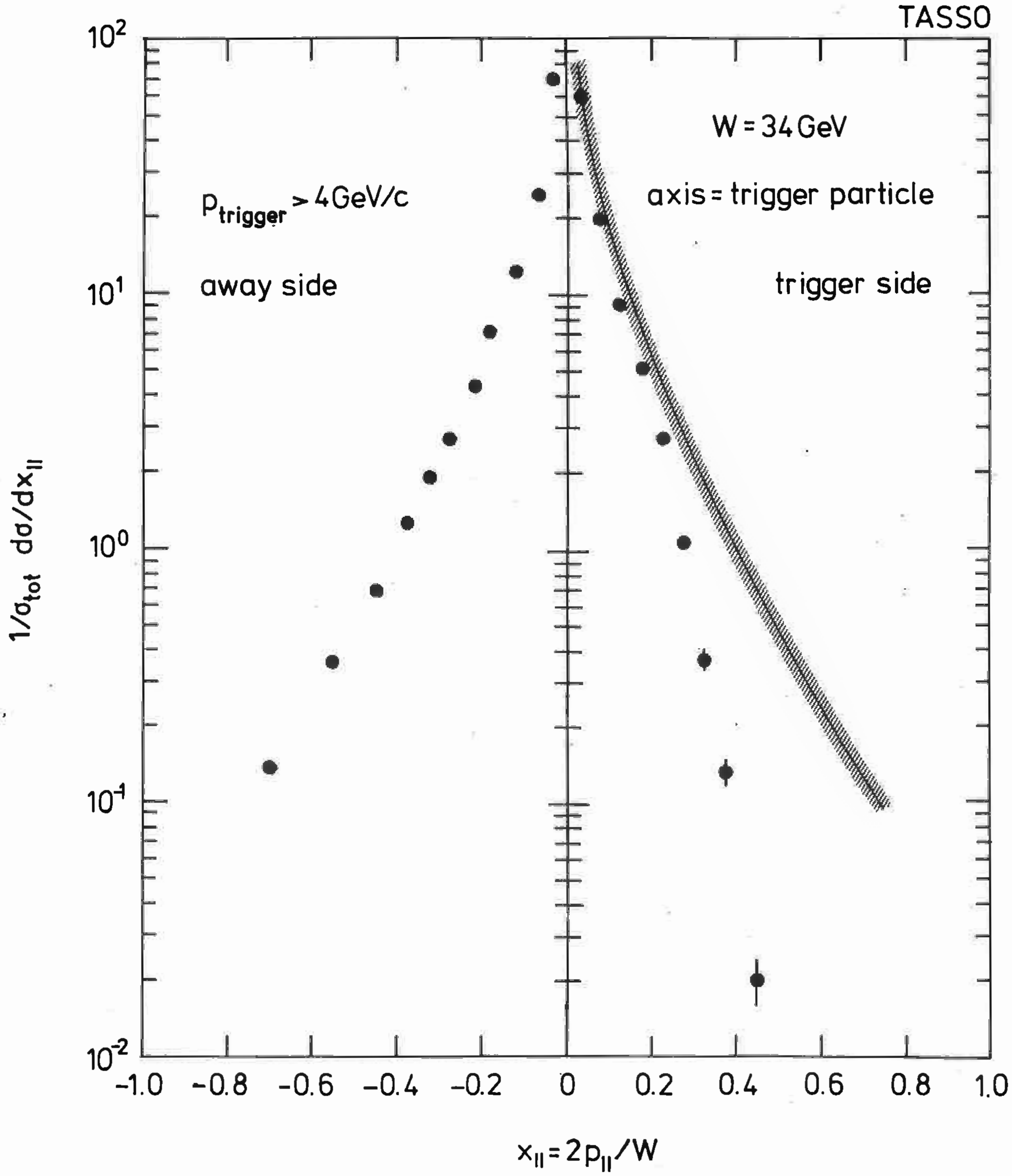
TASSO
10^2
10^1
10^0
10^{-1}
10^{-2}
$1/\sigma_{tot}\ d\sigma/dx_{\parallel}$
$p_{trigger} > 4$ GeV/c
away side
W = 34 GeV
axis = trigger particle
trigger side
-1.0
-0.8
-0.6
-0.4
-0.2
0
0.2
0.4
0.6
0.8
1.0
$x_{\parallel} = 2p_{\parallel}/W$
36698

Fig. 59

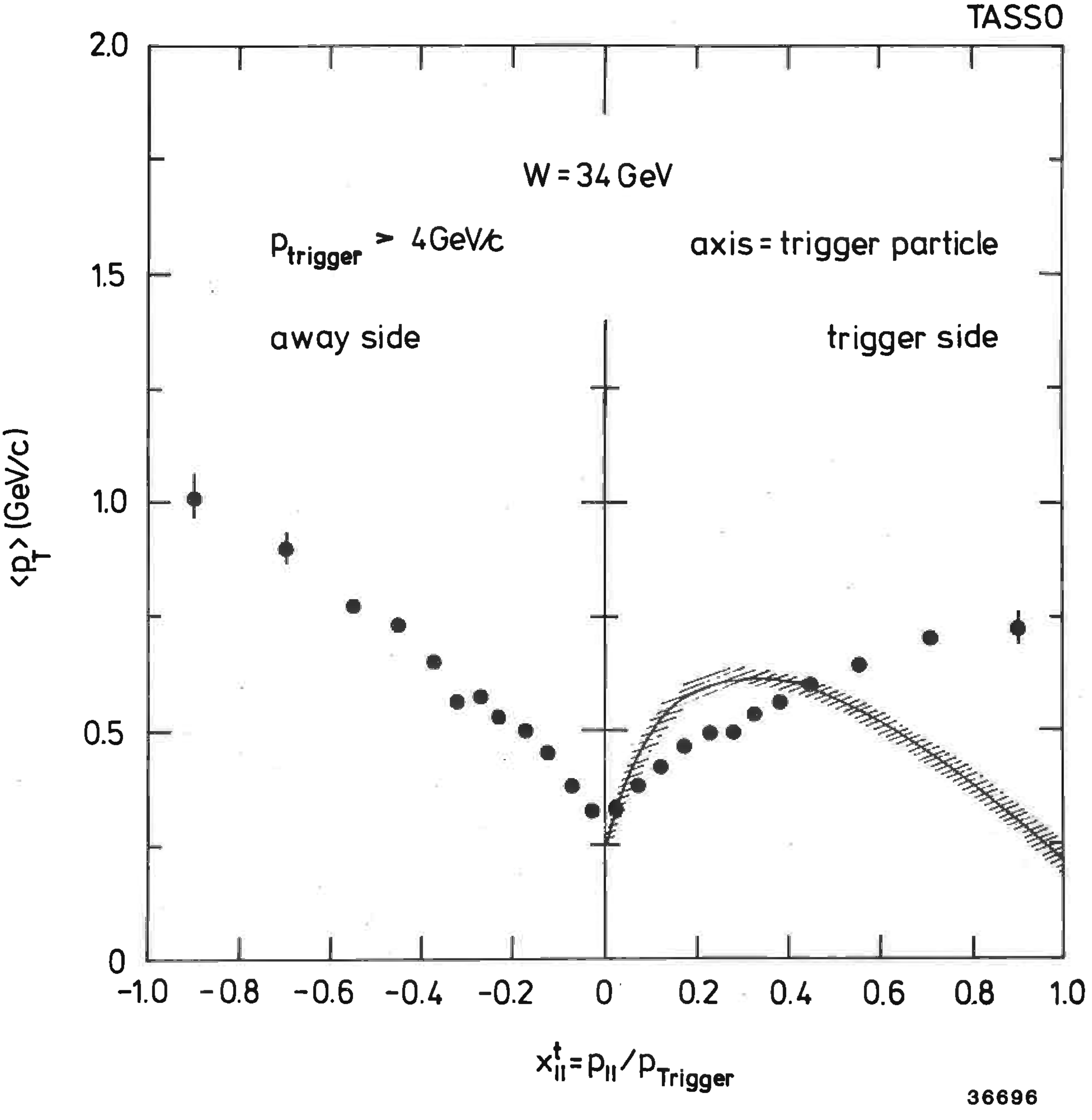
TASSO
W = 34 GeV
$p_{trigger} > 4$ GeV/c
axis = trigger particle
away side
trigger side
2.0
1.5
1.0
0.5
0
$\langle p_T \rangle$ (GeV/c)
-1.0
-0.8
-0.6
-0.4
-0.2
0
0.2
0.4
0.6
0.8
1.0
$x^t_{\parallel} = p_{\parallel}/p_{Trigger}$
36696

Fig. 60

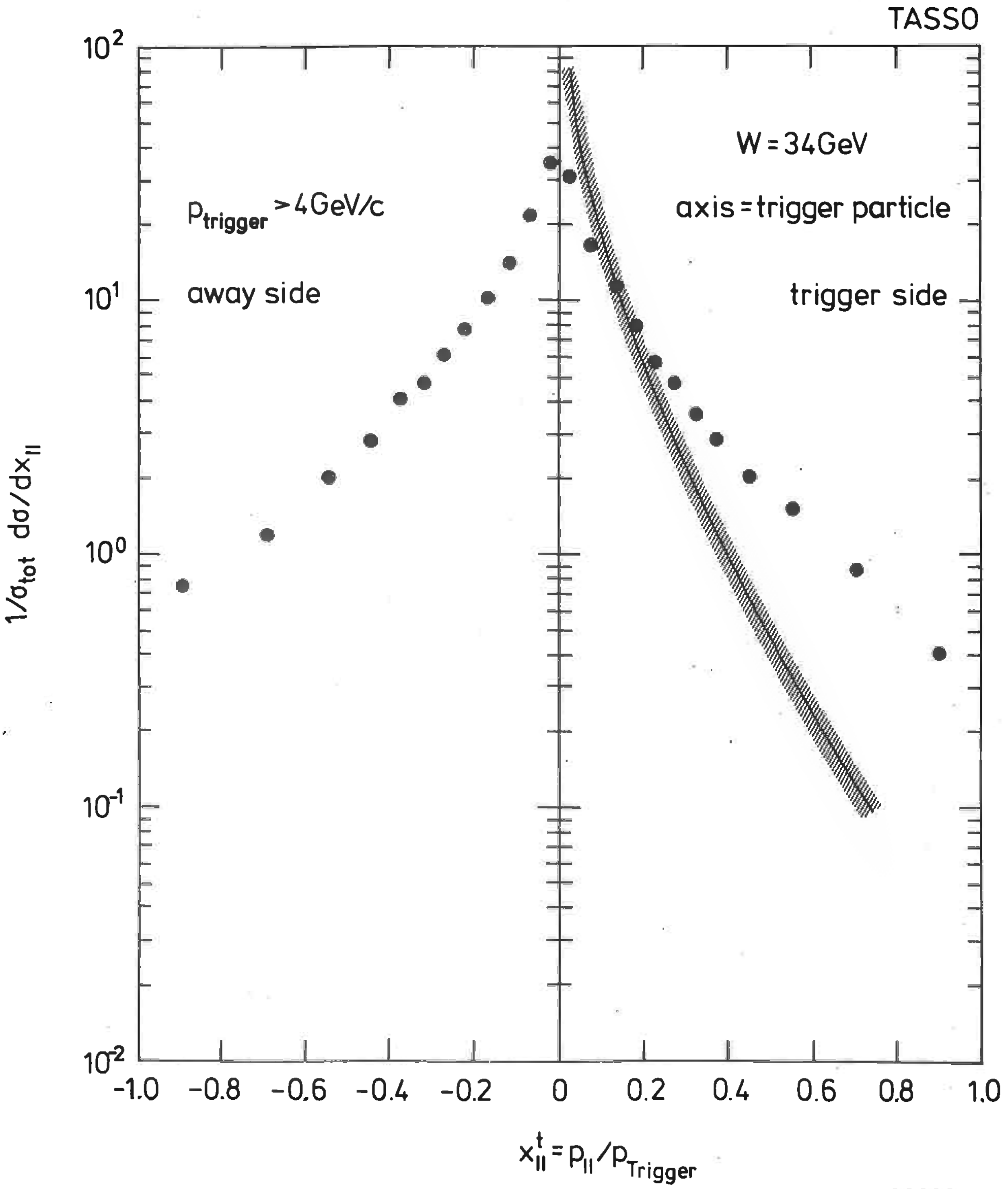
TASSO
10^2
10^1
10^0
10^{-1}
10^{-2}
$1/\sigma_{tot}\ d\sigma/dx_{\parallel}$
$p_{trigger} > 4$ GeV/c
away side
W = 34 GeV
axis = trigger particle
trigger side
-1.0
-0.8
-0.6
-0.4
-0.2
0
0.2
0.4
0.6
0.8
1.0
$x^t_{\parallel} = p_{\parallel}/p_{Trigger}$

36699

Fig. 61